UV-Raman Spectroscopy, X-ray Photoelectron Spectroscopy, and Temperature Programmed Desorption Studies of Model and Bulk Heterogeneous Catalysts

by

Craig Richmond Tewell

B.S. (North Carolina State University) 1994
B.S. (North Carolina State University) 1995

A dissertation submitted in partial satisfaction of the
requirements for the degree of

Doctor of Philosophy
in

Chemistry

in the

GRADUATE DIVISION

of the

UNIVERSITY of CALIFORNIA, BERKELEY

Committee in Charge:

Professor Gabor A. Somorjai, Chair
Professor Adam Arkin
Professor Roya Maboudian

Fall 2002

Abstract

UV-Raman Spectroscopy, X-ray Photoelectron Spectroscopy, and Temperature Programmed Desorption Studies of Model and Bulk Heterogeneous Catalysts

by

Craig Richmond Tewell

Doctor of Philosophy in Chemistry

University of California, Berkeley

Professor Gabor A. Somorjai, Chair

X-ray photoelectron spectroscopy (XPS) and Temperature Programmed Desorption (TPD) have been used to investigate the surface structure of model heterogeneous catalysts in ultra-high vacuum (UHV). UV-Raman spectroscopy has been used to probe the structure of bulk model catalysts in ambient and reaction conditions. The structural information obtained through UV-Raman spectroscopy has been correlated with both the UHV surface analysis and reaction results.

The present day propylene and ethylene polymerization catalysts (Ziegler-Natta catalysts) are prepared by deposition of $TiCl_4$ and a $Al(Et)_3$ co-catalyst on a microporous Mg-ethoxide support that is prepared from $MgCl_2$ and ethanol. A model thin film catalyst is prepared by depositing metallic Mg on a Au foil in a UHV chamber in a background of $TiCl_4$ in the gas phase. XPS results indicate that the Mg is completely oxidized to $MgCl_2$ by $TiCl_4$ resulting in a thin film of $MgCl_2/TiCl_x$, where x

= 2, 3, and 4. To prepare an active catalyst, the thin film of $MgCl_2/TiCl_x$ on Au foil is enclosed in a high pressure cell contained within the UHV chamber and exposed to ~1 Torr of $Al(Et)_3$.

TPD of physisorbed mesitylene molecules has been used as a nondestructive surface probe to distinguish the surface adsorption sites of this model Ziegler-Natta polymerization catalyst. The mesitylene TPD probe revealed two types of surface adsorption sites. The dominant site was attributed to the basal plane of these halide crystallites. Other sites present in lower concentration could be attributed to a defect structure at the basal plane boundaries with other crystal planes. Due to the chlorine termination of the catalyst surface, the metal ions under the chlorine layer could not be differentiated directly with the physisorbed mesitylene molecules. However, the mesitylene TPD profile was able to monitor compositional changes in the outermost chlorine layer accompanying a) the reaction of the catalyst film with the triethylaluminum cocatalysts, b) electron beam irradiation of the film surface, and c) diffusion of bulk chlorine to the surface to minimize the number of defect sites.

Microporous samples of Mg-ethoxide Ziegler-Natta catalyst supports were made from $MgCl_2$ and ethanol. Samples with an ethanol-to-$MgCl_2$ molar ratio (x) from 0.47 to 6 were studied by UV-Raman spectroscopy. These studies indicate the breaking of Mg-Cl bonds at molar ratios $\geq$ 2. At x = 6, the octahedral coordination of the Mg^{2+} ion has been completely replaced by octahedral coordination of the oxygen atoms from the ethanol molecules. It is suggested that the presence of the peak at 683 cm^{-1} may be attributed to the totally symmetric breathing mode of Mg-O octahedra, reinforcing the structure analysis of $MgCl_2(C_2H_5OH)_6$. The Raman shift of the O-H stretch shifts in the

3230-3480 cm^{-1} range as the C_2H_5OH to $MgCl_2$ molar ratio is altered and thus, it can be used to monitor the $MgCl_2(C_2H_5OH)_x$ composition. This correlation is used to follow the dealcoholation of an industrial sample of a Ziegler-Natta support.

The structure of Co-Mo catalysts supported on commercial silica, doped with various amount of sodium ions, was investigated by means of X-ray diffraction (XRD), UV-Raman spectroscopy and XPS. Samples prepared by two different methods were investigated. One set of samples was prepared by classic incipient wet impregnation (WI) and the other by co-impregnation in the presence of nitrilotriacetic acid (NTA). UV-Raman spectroscopic results indicated that sodium effected these two series of catalysts differently. In the case of the WI prepared catalysts, sodium promoted a transformation of polymolybdate species into monomolybdate Na_2MoO_4. In the case of the NTA prepared samples, sodium did not form the Na_2MoO_4 compound, but still induced transformation from heptamolybdates, $Mo_2O_7^{2-}$ and mixed CoMo oxides into MoO_4^{2-} units with distorted tetrahedral symmetry. As indicated by Mo 3d and Co 2p XPS binding energy shifts, in addition to purely structural modifications, sodium induced an electronic effect in the WI samples. The hydrodesulfurization (HDS) catalytic behavior of the samples was explained in terms of the observed structural and electronic changes.

With the success of applying UV-Raman spectroscopy to studying the structure of two different heterogeneous catalysts, an attempt was made to extend the use of this technique to study surface adsorbates on industrial catalyst *in situ*. Two reactions were studied: Cyclohexene hydrogenation / dehydrogenation on a 0.9 wt% Pt / γ-Al_2O_3 catalyst and ethylene hydrogenation on a 5 wt% Pt / γ-Al_2O_3 catalyst. No Raman

features where observed due to either the amorphous alumina support or hydrocarbon fragments on the surface during the cyclohexene reaction experiments. One very broad peak from 2750 to 3250 cm^{-1} was observed during one ethylene hydrogenation experiment. The broadness of the peak indicates a wide distribution of ethylene fragments on the surface and no correlation between this peak and the reaction kinetics could be drawn. UV-Raman spectroscopy results for mesoporous silica (MCM-41) supported nanoparticle catalysts indicate the need for a crystalline support to detect Raman features for the catalyst. A crystalline support may induce better ordering of surface reaction species and may facilitate interpretation of UV-Raman spectroscopic observations.

Dedicated to Elise

Table of Contents

List of Figures

List of Tables

Acknowledgements

The chance to acknowledge my colleagues and friends reminds me how rewarding it was to know and work with them. Long ago I decided to wait until I had written my entire dissertation before I would even start writing the acknowledgements. The writing of the acknowledgements has been a useful carrot dangling before me to keep my motivation high during the writing process.

First and foremost, I would like to thank Professor Gabor A. Somorjai for his support, guidance, and motivation during my atypical graduate school path. I am forever indebted to his patience and understanding as I struggled to decide on a career and educational path. He has always believed in me—thrusting me into new research areas and allowing significant latitude to not only learn, but to fail and thus to succeed. I daresay there is no other advisor with whom I could have had such an incredible experience.

My time with the Somorjai research group has spanned more than seven years now. I began my tenure in June 1995. My early UHV mentors and good friends included Howard Fairbrother, François Reniers, Alex Yoon, Nick Materer, and Pete Jacobs. I have to especially thank Howard and François who have remained important colleagues and friends through the years. I am deeply grateful for the chance to work with and count among my friends Rüdiger Döll, Katja Sperling, Martin Gierer, Christophe Bulliard, Craig Gerken, and John Jensen. All of these folks greatly extended my understanding not only of science, but of life, politics, and ironically, after a great deal of reluctance, foosball. The irony will become evident. I would be remiss if I did not mention the help from the other members of the research group at the time: Paul

Cremer, Fabio Ribeiro, Renee Minick, Gunther Rupprechter, Xingcai Su, David Gracias, and Michael Yang.

When I began working with Enrico Magni in 1996, I realized that the universe could be explained from the seemingly simple equation, V = IR. I am indebted to him for his mentoring, vision, and enthusiasm for science. Over the years Enrico has become much more than a mentor. Both he and his wife, Cristina, are great friends and trusted advisors. I cannot thank them enough.

My life outside the laboratory during my first two years at Berkeley would not have been the same had if it were not for Joel Roberts, Cheryl Hawkins, Robin Fulton, and Chris Caylor. I wish them continued success in their careers wherever they are.

I have to thank Exxon Research and Engineering Company for giving me a chance to extend my experiences during my two and a half year break from graduate school. I have to thank some current and former employees of Exxon for encouraging me to quit and return to Berkeley: Richard Madrid, Chris and Sarah Wall, Yunaima Hernandez, Scott Hagstrom, Mark Andreacci, Giselle Larish, Don Gardner, Hansie Mathelier, and Monica Arboleda.

During some rough times I often relied on my own personal cheerleaders who have and continue to provide unconditional support and friendship. It is said that it is rare to have more than one true friend. I am lucky to have six. Kristi Goettinger, Laura Linton, Angela Gasior, Catherine Harvey, Maria McDonald Freeman, and Joanna Perry thank you! I deeply appreciate the support from Patrick Heinrich, BradTad Nishida, Nathan Sutton, Jon Butzke, Veronica Godfrey, Dana and Kate Lynch, Stacie Moon, Jennifer King, Sameer Damre, and Erin Chervenak.

It was difficult to return to graduate school after a two and a half year break. Saskia Hoffer deserves special recognition in my acknowledgements. She has been an amazing friend to me and especially to Elise. Saskia was always there as a confidant, an extra pair of hands, a carpool partner, a dissertation writing partner, and most recently an ambassador to Los Alamos. We did it!

Jessica Parker Gaughn, too, was a trusted confidant and an always willing extra pair of hands. She helped me through the qualifying process and I hope I returned the favor. I wish her continued success in research and I regret that I will not be in Berkeley to see her graduate.

If it were not for the less visible efforts of Learr English, Sue Yoshioka, Davina Abram, Joel Ager, and especially Inger Coble, this disseration would not have been possible. I am also indebted to Seong Kim, Steve Baldelli, Bénédicte and Gilles Mailhot, and Keng Chou. David Tang deserves special mention for reviewing my dissertation for mistakes. Thank you all.

A l'ami j'ai connu le plus long, Hélène Huchette Desmarault, et ses parents...je vous remercie.

Although my family has not always understood the path my career has taken, they have always been supportive. Even though graduate school has increased the geographical distance between my parents, Terry and Ruth, and my sister, Julie, it has, in many ways, brought us closer. I am grateful for their love and understanding. I am lucky to have had the continued support and love of my two grandmothers, Anna Richmond and Betty Louise Tewell, through most of graduate school. My

grandmother, Louise, was one of my greatest cheerleaders. I wish she were here to see me complete my Ph.D.

During my two and a half years of indecision at Exxon Research and Engineering in Florham Park, NJ, my reluctantly acquired foosball skills gave me the greatest gift of my life. An improbable meeting at a foosball table introduced me to my future wife, Elise Custy. She is the greatest cheerleader, friend, advisor, and confidant. I am not sure if graduate school was more of a challenge for me or for Elise. I thank her for her patience. With the love and support of Elise came the added bonus of her family, Ed, Barbara, John, Joe, Mary, Chris, Evan, David, Mary Jane, Andrew, Peter, Jayna, Mike, and Thelma.

This work was supported by the Director, Office of Science, Office of Basic Energy Sciences, Division of Materials Sciences and Engineering, of the U.S. Department of Energy under Contract No. DE-AC03-76SF00098.

Chapter 1

Introduction

The present scientific frontier in the field of heterogeneous catalysis is understanding and controlling reaction selectivity. To achieve this goal, knowledge must be gained about the structure of the catalyst and the nature of the surface species *in situ*, that is, under reaction conditions. Surface science has provided a great deal of insight into catalysis through *ex situ* studies of model catalysts. Even today on the cutting edge of catalysis research, traditional surface science studies permit an essential starting point of scientific investigation. However, new techniques and approaches are necessary to complement traditional surface science studies with *in situ* information.

Photon in / photon out techniques have the capability of probing both model and industrial catalysts *in situ* and *ex situ.* Vibrational spectroscopies are perhaps the most important of these techniques due to the highly specific molecular-level information obtained. The choice of which particular vibrational technique to use is dictated by careful consideration of the catalytic system. The interaction of the probe and collected photons with both the catalyst and the reaction media must be well understood.

The vibrational spectroscopic technique to probe heterogeneous catalysts important to the petrochemical industrial must meet several important criteria. The reactions are generally conducted in a dense gas phase of organic molecules with a bed of catalyst at temperatures ranging from 25 to 500^{o}C. The catalyst is usually an active metal (e.g., Pt, Pd, Rh, Mo, Co, Ni, Cu, Ag) dispersed on a metal oxide support (e.g.,

Al_2O_3, CeO_2, TiO_2). These conditions almost immediately preclude using infrared (IR) photons as an *in situ* probe for several reasons: (1) attenuation of the incident photon by the gas phase organic molecules, (2) detection interference from blackbody radiation emitted by the high temperature catalyst bed, and (3) the attenuation of the incident photons below 1200 cm^{-1} from the strong absorption due to the highly ionic metal-oxygen bonds of the support. To overcome these difficulties the photon in and photon out must be in a different part of the electromagnetic spectrum. Since Raman spectroscopy is an energy loss rather than absorption technique, the photon in (and therefore photon out) can be chosen to be compatible with a particular catalytic system.

As with all techniques, Raman spectroscopy is not without its challenges. The Raman scattering process is notably weak. This weakness not only requires an intense source of incident photons, but the detection of the photon out often competes with other photophysical processes such as Rayleigh scattering, fluorescence, and phosphorescence. Early application of Raman spectroscopy to heterogeneous catalysis was hampered by the lack of highly intense, monochromatic incident photon sources. With the advent of continuous-wave noble gas ion lasers, this problem was overcome. However, these lasers provide photons in the visible region only. Surface hydroxyl groups commonly found on the metal oxide supports and trace organic contaminants fluoresce quite strongly in the visible.[1] The fluorescence spectrum overlaps with and overwhelms the much weaker Raman spectrum.

With newer generation of laser instruments[2], Asher and Johnson report a new approach to measuring the unenhanced Raman spectrum of samples known to fluoresce strongly in the visible.[3] Using a laser wavelength in the ultraviolet, the Raman

spectrum can be collected without interference from the fluorescence that is still occurring in the visible.

This approach to Raman spectroscopy is emulated and extended in the work presented in this dissertation. A detailed description of Raman spectroscopy and the other experimental techniques used is given in Chapter 2. A portion of recent extensive *ex situ* studies of model propylene and ethylene polymerization catalysts (Ziegler-Natta catalysts) is discussed in Chapter 3.[4,5] A UV-Raman spectroscopic investigation of the structure of a bulk Ziegler-Natta catalyst support material[6] and an *in situ* study is presented in Chapter 4. Results of a UV-Raman and X-ray photoelectron spectroscopic study of the structural differences between two preparation methods for hydrodesulfurization catalysts are given in Chapter 5.[7] Finally, in Chapter 6 results of an attempt to monitor surface hydrocarbon fragments on an industrial reforming catalysts (Pt supported on γ-Al_2O_3) during reaction are presented.

References

(1) Koningstein, J. A.; Gachter, B. F. *J. Opt. Soc. Am.* **1973**, *63*, 892.

(2) Asher, S. A.; Johnson, C. R.; Murtaugh, J. *Rev. Sci. Instrum.* **1983**, *54*, 1657.

(3) Asher, S. A.; Johnson, C. R. *Science* **1984**, *225*, 311.

(4) Kim, S. H.; Tewell, C. R.; Somorjai, G. A. *Langmuir* **2000**, *16*, 9414.

(5) Kim, S. H.; Tewell, C. R.; Somorjai, G. A. *Korean J Chem Eng* **2002**, *19 (1)*, 1.

(6) Tewell, C. R.; Malizia, F.; Ager, J. W.; Somorjai, G. A. *J. Phys. Chem. B* **2002**, *106*, 2946.

(7) Parola, V. L.; Deganello, G.; Tewell, C. R.; Venezia, A. M. *Applied Catalysis A:General* **2002**, *in press*.

Chapter 2

Experimental Techniques

Section 2.1 UV-Raman Spectroscopy and Experimental Setup

Section 2.1.1 Introduction to Normal Raman Spectroscopy Raman spectroscopy is a technique that provides molecular-level information by analyzing the light scattered from molecules subjected to illumination by a monochromatic source of photons. Upon collision with a molecule, a photon, $h\nu_o$, can be scattered elastically or inelastically. The elastically scattered photons are referred to as Rayleigh or classical scattering. The inelastically scattered photons ($h\nu_r$) have either lost (Stokes) or gained (anti-Stokes) energy. The magnitude of the energy lost or gained is reported, not in energy units, but as a frequency shift, $\Delta\nu$, where $\Delta\nu = (\nu_o - \nu_r)/c$ and the units are in wave numbers, cm^{-1}. This frequency shift is referred to as the Raman frequency or the Raman shift.

A Raman shift corresponds to a vibrational or rotational transition of the molecule. In the case of vibrational modes of organic molecules, the frequency of these transitions are in the infra-red (IR) region of the electromagnetic (E-M) spectrum. In IR spectroscopy, these transitions are measured by direct absorption of infra-red photons. The region of the E-M spectrum where these transitions are observed in Raman

spectroscopy is dictated by the wavelength of the illuminating photon. For example, the wavelength of a Raman photon for a given shift is calculated as follows:

$$RamanShift, cm^{-1} = \frac{n_o - n_r}{c} = 10^7 \frac{nm}{cm}\left(\frac{1}{l_o} - \frac{1}{l_r}\right) \qquad (2.1)$$

where ν_o and ν_r are the frequency of the incident and Raman scattered photon, respectively, and λ_o and λ_r are the wavelength of the incident and Raman scattered photon in nm, respectively. Solving for λ_r in (2.1):

$$l_r = \frac{10^7}{\frac{10^7}{l_o} - RamanShift, cm^{-1}} \qquad (2.2)$$

Table 2.1 shows the calculated wavelengths for 10 and 4000 cm^{-1} Raman shifted photons with three different wavelengths of incident photons. In absorption experiments, 10 to 4000 cm^{-1} always corresponds to 1,000,000 to 2,500 nm.

Raman spectroscopy is not merely a molecular vibration technique that can be conducted in different spectral regions, although this capability will be shown to be quite useful in a later section. Scattering and absorption vibrational spectroscopies differ in mechanism and do not provide identical information. The frequencies of a Raman spectrum are not necessarily identical to those in an infrared absorption spectrum. As will be demonstrated in Chapter 4, the molecular vibrational information provided by the two techniques are different, but complementary.

Section 2.1.2 Theoretical Origin of Light Scattering by Molecules There are generally three approaches to account for observed light scattering phenomena: (1) a classical explanation in terms of E-M radiation produced by electric and magnetic multipoles oscillating with a given frequency induced in the scattering molecule by the

electric and magnetic fields of the incident photon; (2) a time-independent quantum mechanical treatment to calculate transition moment amplitudes or the electric moment matrix; and (3) a general quantum mechanical treatment using time-dependent perturbation theory.

(1) The classical approach will not be discussed in this dissertation but can be found elsewhere.[1,2] The mathematics used in developing this treatment are more straightforward, but the results cannot account for many aspects of light scattering phenomena.

(2) The induced electric moment matrix, P_{nm}, for transitions between the initial state, n, and the final state, m, is defined by the following:

$$\boldsymbol{P}_{mn} = \int \psi_m^{*} \boldsymbol{P} \psi_n d\tau \qquad (2.3a)$$

or using Dirac notation, (2.3a) becomes;

$$\boldsymbol{P}_{mn} = \langle \psi_m | \boldsymbol{P} | \psi_n \rangle \qquad (2.3b)$$

where P is the induced dipole moment, ψ_n and ψ_m are the time-independent wave functions of the initial and final states, respectively. In the linear induced dipole approximation, P, in (2.3a) and (2.3b) be approximated (in first order) by:

$$\boldsymbol{P} = \alpha \times \boldsymbol{E}_o \qquad (2.4)$$

where α is the polarizability matrix and $\mathbf{E_o}$ is the electric field vector of the incident photon, $h\nu_o$. A Taylor series expansion of one element of the polarizability matrix in terms of the normal coordinates is given by:

$$\alpha_{ij} = \left(\alpha_{ij}\right)_o + \sum_k \left(\frac{\partial \alpha_{ij}}{\partial Q_k}\right)_o Q_k + \frac{1}{2}\sum_{k,l}\left(\frac{\partial^2 \alpha_{ij}}{\partial Q_k \partial Q_l}\right) Q_k Q_l + \ldots \qquad (2.5)$$

where α_{ij} is the ijth element of the polarizability tensor, α, and Q is the normal coordinate of the molecular vibration denoted by the subscripts k and l. To obtain an expression that qualitatively describes the selection rules for light scattering from molecules, the first two terms of (2.5) are substituted into (2.4). Then (2.4) is inserted in (2.3b) to yield:

$$P_{mn} = \overbrace{(a_{ij})_o \langle y_m | y_n \rangle E_o}^{a} + \overbrace{\sum_k \left(\frac{\partial a_{ij}}{\partial Q_k} \right)_o \langle y_m | Q_k | y_n \rangle E_o}^{b} \qquad (2.6)$$

Term **a** of (2.6) accounts for Rayleigh scattering since it is only non-zero when n = m. The selection rules of Raman scattering are determined term **b** of (2.6). By assuming that the electronic, vibrational, and rotational wavefunctions are separable and that the vibrational wavefunctions can be approximated by harmonic oscillator wave functions, the Raman selection rule is m = n ± 1. In addition, at least one normal mode vibration must have a non-zero polarizability derivative.

(3) By applying time-dependent perturbation theory, the following is obtained for the induced electric moment matrix:

$$P_{nm} = \frac{1}{h} \sum_r \left(\frac{M_{nr} M_{rm}}{n_{rn} - n_o} + \frac{M_{nr} M_{rm}}{n_{rm} + n_o} \right) E_o \qquad (2.7)$$

where h is Planck's constant, r is any level of a complete set of the unperturbed molecule, ν_{rm} and ν_{rn} are the frequencies corresponding to the difference between states denoted in the subscripts, ν_o is the frequency of the incident photon, M_{nr} and M_{rm} are the corresponding transition moments using time-independent wavefunctions as calculated by (2.6) with the appropriate change of subscripts, and E_o is the electric vector of the incident light. In this expression, the selection rules for Rayleigh and

Raman scattering, as discussed previously, are also valid. This expression accounts for the so-called Resonance Raman effect. When the frequency of the incident photon, ν_o, matches the transition frequency, ν_{rn}, the first term of (2.7) becomes, in principle, infinitely large. In practice, a large increase in scattering intensity can be observed, although only those vibrations that couple to the r ? n transition are enhanced.

Now that (2.7) has been introduced it is possible to briefly discuss the theoretical intensity of a Raman transition. A simplified expression for the intensity of a Raman transition, I, is given by:

$$I \propto I_o N(n_r)^4 |P_{nm}|^2 \qquad (2.8)$$

where I_o is the intensity of the incident laser, N is the number of scatters inside the focal volume of the laser, the ν_r is the frequency of the Raman scattered photon (not the Raman shift), and P_{nm} is the transition matrix given by (2.7). A more detailed description can be found elsewhere.[1]

Section 2.1.3 Motivation for UV-Raman The Raman spectra reported in this dissertation have been acquired with a UV laser excitation source. The motivation for using a UV photon source arises from the experimental difficulties from competing photoluminescent processes frequently encountered when using a visible photon source.[3,4] Visible photons are sufficiently energetic to induce electronic transitions in many of the inorganic and organic compounds of interest in heterogeneous catalysis. Once the sample has absorbed a photon, the energy will dissipate through photoluminescent or photophysical processes. In photophysical processes, the sample's vibrational modes are excited and the energy is dissipated through heat. In

photoluminescent processes, all or part of the absorbed energy is released as a photon through fluorescence or phosphorescence. To understand the motivation for choosing a UV excitation source for Raman scattering experiments, a brief explanation of photoluminescent processes is necessary. In principle, both fluorescence and phosphorescence can create the same experimental difficulty and it is not generally possible to know which of the two processes is occurring during acquisition of a Raman spectrum. As such, only fluorescence will be discussed. A more rigorous explanation of fluorescence and phosphorescence can be found elsewhere.[4,5]

Figure 2.1 depicts ground and first excited singlet states of a hypothetical molecule. The horizontal lines in each singlet state represent the vibrational quantum levels for a single normal mode of the hypothetical molecule. The arrow pointing to the top of the page represents the energy, $h\nu_{incident}$, of a photon incident on the sample. In the diagram the energy of that photon exactly matches the difference in energy between the ground vibrational level of the ground singlet state, S_0, and an excited vibrational mode of the first-excited singlet state, S_1. With this energy matching, an electron of the molecule increases in energy by $h\nu_{incident}$ and its potential follows that of S_1. The molecule immediately begins to dissipate some of that energy through the collisions incurred as a result of being in an excited electronic and vibrational mode. Eventually during this rapid loss of energy, the molecule arrives in the ground vibrational state of S_1. If S_1 and S_0 do not intersect at this energy, there is a non-zero probability that the remaining energy from $h\nu_{incident}$ will be lost through the emission of a photon, $h\nu_{emitted}$. In Figure 2.1, this photoemission is depicted as occurring from the ground vibrational mode of S_1 to an excited vibrational mode of S_0. This figure depicts the nuclear

distance in lowest vibrational state of the first-excited electronic state being larger than the equivalent in the ground electronic state. As a result of this difference in nuclear distance, $h\nu_{emitted}$ will be less than $h\nu_{incident}$. This loss in energy corresponds to a lengthening of the wavelength of the emitted photon relative to the absorbed photon. This change in energy and wavelength is called a Stokes-shift.

Recalling from the introduction to normal Raman spectroscopy, the scattered photons are also Stokes-shifted. In fact the use of the term Stokes photons in Raman spectroscopy originates from the study of fluorescence and phosphorescence. The experimental difficulty arises when the Stokes-shifted fluorescence photons overlap the Stokes-shifted Raman photons. Typically the fluorescence emission is much more intense than Raman scattering. Figure 2.1 does not fully explain the observed fluorescence emission. Only the most probable photoemission is shown. Other transitions from S_1 to different vibrational levels of S_0 have non-zero probability. Thus, a fluorescence spectrum is not discrete but rather broad, owing to the high density of vibrational levels at the higher energy portion of S_o.

An example of fluorescence interference is shown in Figure 2.2. The Raman spectrum of $Al_2O_3 \cdot 3H_2O$ was acquired using both a visible source, 488 nm, and a UV source, 244 nm. In the visible Raman spectrum, there is a broad and intense background that maximizes at approximately 570 nm. Referring to Table 2.1, it is clear that 570 nm superimposes a 10-4000 cm^{-1} Raman spectrum when using 488 nm radiation. The result of this superimposition is quite clear in Figure 2.2. The background of the UV spectrum is flat and free of fluorescence interference. The advantage of the lack of fluorescence interference can be quantified by calculating the

signal-to-noise (S/N) ratio for a given mode in each spectrum. The S/N ratio of the 3618 cm^{-1} peak is 43 times greater in the UV spectrum than the visible spectrum. At lower frequency, the 569 cm^{-1} peak is 10 times greater in the UV spectrum than the visible spectrum.

It is important to note that the $Al_2O_3 \cdot H_2O$ is fluorescing during the acquisition of both spectra in Figure 2.2. The transition between electronic states that is the source of fluorescence emission is always the same for a given molecule (S_1? S_0 in this hypothetical case). So, unlike Raman scattering, the fluorescence spectrum does not shift with a change in incident photon energy. The fluorescence maximum is 570 nm for $Al_2O_3 \cdot H_2O$.

Section 2.1.4 95-SHG Lexel Laser The LEXEL 95-SHG laser is an intracavity frequency doubled Argon ion laser that produces a continuous-wave UV output at 244 nm. The frequency doubling is accomplished through Second Harmonic Generation using a nonlinear crystal of β-Barium Borate, BaB_2O_4 (BBO). The SHG power is proportional to:

$$P^{2w} \approx \frac{\left(P^{w}\right)^2}{A}\left[\frac{\sin\left(L\Delta k/2\right)}{L\Delta k/2}\right]^2 \qquad (2.8)$$

where A is the cross section of the visible beam, L is the length of the doubling crystal, Δk is the difference between the wave vectors of the UV and visible beams, and P^{ω} and $P^{2\omega}$ are the powers of the visible and UV beams, respectively. Thus to increase the power of the UV beam, the power of the visible beam can be increased. The output of most common CW ion lasers is a fraction of the power inside the laser cavity. This is the advantage of placing the BBO crystal inside the laser cavity as shown in Figure 2.3.

However, care must be taken to prevent the power density from exceeding the damage threshold of the BBO crystal.

The power of the UV beam will be maximized for a given visible power when the argument of the sine function in (2.8) is zero. That is, when

$$\Delta k = k^{2w} - k^{w} = \frac{4p\left(n^{2w} - n^{w}\right)}{l^{w}} = 0 \qquad (2.9)$$

where $k^{2\omega}$ and k^{ω} are the wave vectors for the UV and visible beams, respectively. When the phases of the UV and visible beams are matched, $n^{2\omega}$ will equal n^{ω} and (2.9) will be zero. This phase matching is accomplished by adjusting the angle of the BBO crystal shown in Figure 2.3. In principle the prism near M1 of Figure 2.3 can be adjusted to "select" another Argon ion transition to lase and this new line could be frequency doubled by the BBO. In practice with the existing BBO crystal, phase matching cannot be maximized for any but the 488.0 nm wavelength of the Argon ion laser.

Section 2.1.5 Acquiring a Raman Spectrum The Raman scattered light is collected by a 50 mm diameter f/2 fused silica lens; this corresponds to a solid angle of collection of 0.20 sr. The collected scattered light is focused on the entrance slit of a f/3.7 SPEX 1877 Triplemate triple spectrometer by a 160 mm focal length lens.

A schematic of the SPEX 1877 Triplemate is given in Figure 2.4. The Triplemate is specially designed to provide low-stray light that is both flat and undistorted at the focal plane. The Triplemate has two main sections. The first is a 0.22 m double monochromator filter stage with gratings locked in a subtractive-dispersion mode. It acts as a variable-wavelength, selectable bandpass filter that feeds a non-

dispersed segment of radiation from a sample into the entrance slit of the second, or spectrograph, stage. The 0.6 m, single-monochromator spectrograph stage disperses the radiation over the detector. To vary this dispersion and the spectral coverage at the focal plane, the spectrograph has provisions for mounting three gratings on a manual turret.

In Figure 2.4 a segment of white light is artificially broken into color segments as shown on the left of the lens, **L1**. **L1** focuses the light on **S1**. The f/number of this lens is matched to the distance between **S1** and **M1** such that the image on **L1** will exactly fill mirror **M1**. Part of the image on **L1** can be rejected by changing the aperture of **S1**. If the image is of a uniform sample, this will simply reduce the intensity of light entering the spectrometer. **M1** collimates the light on the first diffraction grating, **G1**. **G1** disperses the light across **M2**. **M2** reflects the light through a second slit, **S2**. Since the image has been dispersed spatially, **S2** serves as the bandpass filter. This effect is illustrated on **M3** where only the yellow, green, and blue light reflected from **M2** reaches **M3**. **M4** collimates the light onto the second diffraction grating that cancels the dispersions of **G1**. **M5** focuses the light on a third slit, **S3**. Since the light is undispersed at **S3**, the aperture sets the spectral resolution. The smaller this aperture, the less overlap between neighboring colors when the collimated light from **M6** is dispersed by one of the **G4-6** gratings. There is a practical limit to how small this aperture can be since the intensity of the light passing **S3** is proportional to the square of the aperture size. **M7** projects a flat image onto the focal plane of the detector.

To acquire a spectrum of a certain Raman shift region, it is necessary to set the central wavelength of both the dispersion and filter stage. Figure 2.5 is a schematic of

the SPEX 1877 Triplemate control panel. In this schematic, the central wavelength of **G6** is shown to be 251.0 nm. This value can be changed by pressing the "UP" or "DWN" buttons. The central wavelength of the filter stage is shown in the "Filter nm" window. The scale is by default for 600 gr/mm diffraction gratings in **G1** and **G2**. These gratings have been replaced with 2400 gr/mm gratings to allow for more efficient rejection of the intense Rayleigh scattered light at low Raman shifts. As a result, the "Filter nm" window will indicate a value four times the actual central wavelength of the filter stage. The central wavelength of the filter stage is controlled by the "Filter Control" knob. Another consequence of having such high groove density gratings in the filter stage is that it is no longer possible to fill the entire focal plane of the detector with light. Even with **S2** fully open, the maximum bandpass when λ_o is 244 nm is approximately 1000 cm^{-1}. For a typical **S3** setting of 200 μm the spectral resolution is ~24 cm^{-1}.

The spectrum is collected on a Princeton Instruments back thinned, UV-enhanced liquid-nitrogen-cooled 1340 x 100 pixel CCD detector (Model No. LN/CCD-1340/100-EB/1). The quantum efficiency of the CCD array at 244 nm is approximately 33%. Computer acquisition is accomplished with a Roper Scientific computer card and WinSpec32 software package.

Spectra obtained between 0 and 1500 cm^{-1} were calibrated using the well-known Raman shifts of cyclohexane.[2] Peaks were fitted to a Lorentzian line shape. Table 2.2 shows the results of a typical calibration performed in this spectral region. For a given dispersion and filter stage position, a cyclohexane spectrum is acquired between 3 and 6 times. Each spectrum is fitted and the average peak position is used to make a linear

correlation between CCD pixel position and Raman photon wavelength, λ_r. This correlation is inserted into equation (2.1) to create a correlation between Raman shift and CCD pixel. As seen from Table 2.2, this calibration will provide a Raman shift with a 95% confidence level between 0.3 and 0.7 cm^{-1}.

Spectra obtained between 3200 and 3620 cm^{-1} were calibrated using the O-H peak frequencies of gibbsite[6] in a procedure identical to that described above. This calibration is extrapolated for use in a region spanning from 2800 to 3700 cm^{-1}.

Section 2.1.6 Catalytic Reactors for UV-Raman Spectroscopy Raman spectroscopy offers the capability of probing samples in the presence of a dense gas or ambient liquid phase. Unlike some non-linear spectroscopic techniques, Raman spectroscopy is not uniquely surface sensitive. This is advantageous in the sense that, with Raman spectroscopy, optically flat and reflective surfaces are not strictly required. The intensity of a Raman transition is governed by (2.8). In the case of hydrocarbon fragments on a high surface area catalyst, the number of scatters, N, will be very small in a very tightly focused laser beam. To obtain a useful signal-to-noise ratio with no enhancement due to resonance or the surface enhanced Raman (SERS) effect, one can only increase the incident laser intensity, I_o. With an increase in laser intensity comes an increase in the local temperature of the sampled spot. It has been reported that the local temperature can be as much as 100^{o}C greater than the surrounding material.[7] Such a large temperature difference creates a significant problem to relate Raman spectra with kinetic data. Several studies have been conducted to determine the effect of the temperature increase.[7-10]

Several approaches have been used to minimize the local heating effect during the acquisition of a Raman spectrum. A common approach is to focus the laser beam not as a spot, but as a line. In this way, the flux of photons is spread across the sample in effect increasing the number of scatters, N, probed by the incident laser, I_o.

In another approach, the catalyst sample is rotated during irradiation by the incident laser.[11,12] Most heterogeneous catalysts are in the form of extrudates of silica, alumina, or other metal oxides and are often crushed to powder for scientific studies. To prevent the powder from dispersing during rotation it is usually compressed into a mechanically rigid pellet. Reactant gases are flowed around the pellet during the experiment. Quantitative kinetic data is difficult to obtain because it is usually unknown how far reactant gases diffuse into the pellet.

A rather creative approach has been developed to study samples under cryogenic temperature control although it can be extended to any temperature range. To avoid the obvious difficulties of rotating very cold components of the apparatus, the geometry of the incident laser and the laser focusing lens is carefully designed to provide for scanning the laser beam over the sample in a linear[13] or circular path[14]. This approach does allow for significant flexibility in the types of samples to be probed but the experimental setup is very sensitive to alignment.

In 2000 Chua and Stair published a paper that described an *in situ* fluidized bed reactor for measuring UV-Raman spectra of catalysts during reaction.[15] In their approach a powdered catalyst rests on a porous frit contained near the top of a stainless steel tube. Gas is forced through the frit and the bottom of the powdered catalyst bed providing vertical lift to the particles. An electromagnetic shaker is used to induce side-

to-side motion of the particles. The result is a bed of fluidized particles. In other words the packing density of the powdered bed has been significantly reduce but the particles are not propelled out of the stainless steel tube. Now when a laser is incident on the top of this fluidized bed, the same catalyst particles are not always in the focal volume.

Two reactors have been built for the work contained in this dissertation. The first is a glass packed bed reactor shown in Figure 2.6. The porous disk on which the catalyst rest is also made of glass. The second reactor is shown in Figure 2.7 and is based on the design by Chua and Stair.[15] A photo of the fluidized bed reactor with the electromagnetic shaker[16] is shown in Figure 2.8. The porous metal disk has a uniform porosity throughout its volume of 40 μm.[17] The advantage of the fluidized bed can be seen in Figure 2.9. In this figure two spectra of pyridine adsorbed on a bed of ZSM-5 are shown. The acquisition time and conditions were identical for both spectra. When the bed is not fluidized, there is a significant amount of laser induced carbon at 1635 cm^{-1} relative to the fluidized spectrum. The resonance-enhanced ring breathing mode of pyridine at 1020 cm^{-1} has a much better signal-to-noise ratio in the fluidized bed spectrum.

Section 2.2 Surface Science Techniques and Experimental Setup

Section 2.2.1 Ultra High Vacuum (UHV) Many surface science techniques involve the interaction of electrons with the surface of interest. For surface science techniques to be useful in the field of catalysis, the composition of chemical species at the surface should not only be measurable, but also controllable. This necessitates maintaining a "clean" surface (i.e., free of contaminants) for at least the duration of the

experiment. Many clean surfaces (e.g. metallic surfaces) are highly reactive with oxygen and carbon containing compounds. Performing experiments under ultra-high vacuum conditions ensures that the mean free path of an electron is large enough to leave the source, interact with the surface, and return to the analyzer as well as leaving the surface free of oxygen and carbon for a reasonable length of time. The quality of the vacuum can be approximated by considering the impact rate of molecules with the surface. Using a simplified form of the kinetic theory of gases, the impact rate is estimated by the following:

$$r = 3.51 \times 10^{22} \frac{P}{(TM)^{0.5}}$$

where P is the pressure in torr, T is the temperature in Kelvin, and M is the atomic mass unit of the molecule impacting the surface. For a molecule of atomic mass 28 (e.g., N_2 or CO) at a pressure of 1 x 10^{-9} torr and room temperature, the arrival rate is 3.3 x 10^{11} molecules cm^{-2} s^{-1}. For a 1 cm^2 sample area, one monolayer will be formed in approximately one hour assuming each impact results in a physisorption or chemisorption (i.e., a sticking probability of 1).

The studies reported in this dissertation were performed in a stainless steel UHV chamber (Figure 2.10) pumped with a liquid nitrogen cooled diffusion pump. An ion pump is attached to the chamber, but is used primarily for maintaining vacuum when the diffusion pump is off line. A base pressure of 2 x 10^{-9} torr can be achieved after heating the chamber to desorb gases adsorbed to the walls until a pressure of <5 x 10^{-8} Torr is achieved while the chamber is still hot. After the heating is turned off, all of the equipment with filaments are energized slowly to operating conditions. Current is

continually passed through the filaments until the chamber is at room temperature. If the filaments are not energized while the chamber is cooling, subsequent use of the equipment will cause the base pressure to increase.

The UHV chamber is equipped with a sputter ion gun for surface cleaning, an X-ray source, a double-pass cylindrical mirror analyzer (CMA) with a coaxial electron gun for X-ray photoelectron spectroscopy (XPS), and a quadrupole mass spectrometer (QMS) for residual gas analysis and TPD. A commercially available sample manipulator provided three-dimensional translation and 360^{o} rotation of the sample. The chamber also has three leak valves for gas exposure, a Mg evaporation source for the Mg dose, an electron flood gun for electron beam irradiation of the sample, and an internal high-pressure (HP) reaction cell for polymerization. Further details are given elsewhere.[18] Gas admittance into the UHV chamber was controlled with leak valves facing the sample. Nominal pressures reported in this dissertation were readouts of the nude ion gauge, located about 20 cm away from the sample, without correction for ionization sensitivity and dosing geometry.

Section 2.2.2 X-ray Photoelectron Spectroscopy (XPS) X-ray photoelectron spectroscopy (XPS) is a technique in which a sample is irradiated with nearly monochromatic soft X-rays and the kinetic energy of the emitted core electrons is measured. A simplified depiction of the XPS process is shown in Figure 2.11A. More elaborate explanations can be found elsewhere.[20-22] In Figure 2.11A an X-ray of energy $h\nu$ ejects a carbon 1s electron. The emitted electron has a kinetic energy, KE_1, that can be measured by an electron energy analyzer (typically referred to as a spectrometer). XPS spectra are given as a plot of intensity versus binding energy (BE). The binding

energy of the photoelectron is characteristic of the atomic orbital from which the electron originated. Therefore, the BE will provide the identity of the atoms present in the analysis volume. Furthermore, since the BE is sensitive to the local electron density, shifts in BE for a given atom provides an indication of the oxidation state of the atom.

In Koopman's approximation, the binding energy (BE) of the photoelectron is related to the measured kinetic energy as follows:

$$BE = hn - KE_{meas} - \Phi_s \qquad (2.10)$$

where $h\nu$ is the energy of the soft x-ray, KE_{meas} is the kinetic energy of the emitted photoelectron as measured by the spectrometer, and Φ_s is the work function of the spectrometer. As indicated in Figure 2.11B, the kinetic energy that is measured by the spectrometer is not necessarily equivalent to the kinetic energy of the electron emitted from the sample volume. Oftentimes, the sample and spectrometer work functions are different and unknown. The spectrometer work function can be estimated by using an internal BE standard within the sample volume. In this dissertation, a BE of 84.0 eV for the $Au4_{f_{7/2}}$ peak is used as the internal standard unless otherwise noted.

Quantitative determination of the surface atomic concentration is accomplished by correcting the calculated peak area by a sensitivity factor specific to each element as follows[22]:

$$C_i = \frac{\frac{A_i}{S_i}}{\sum_{j=1}^{i} \frac{A_j}{S_j}} \qquad (2.x)$$

where C_i is the concentration of species i, S_i is the sensitivity factor of species i, and the summation is over all species present in the XPS spectrum. The sensitivity factors used are provided in Table 2.3 and were taken from reported values.[23]

XPS experiments are performed with a Perkin-Elmer 04-548 Dual Anode X-ray Source and a PHI 13-255G Double Pass Cylindrical Mirror Analyzer for electron energy analysis. Both the Mg (1253.6 eV) and Al (1486.6 eV) anode X-ray sources are used to acquire XPS spectra. The Al X-ray photons are sufficiently energetic to induce the Mg KLL Auger transition. The Mg source is more intense and allows a better signal-to-noise ratio in a shorter accumulation time.

Section 2.2.3 Temperature Programmed Desorption (TPD) Temperature programmed desorption (TPD) is probably the most widely used technique for the determination of the heat of adsorption and coverage of molecules on surfaces and for studying desorption kinetics. Detailed descriptions of the experimental setup and the interpretation of results have been published elsewhere.[21,24-30] Briefly, the surface under analysis is held at constant temperature while being exposed to a probe molecule. The system is then evacuated and the temperature of the adsorbate-covered surface is ramped linearly. The desorbing species are monitored with a mass spectrometer and plotted as a function of sample temperature. A schematic of the experimental setup used in this dissertation is given in Figure 2.12.

The sample coverage is proportional to the integral of the thermal desorption spectrum. The gas-phase concentration profile can easily be related to the kinetics and energetics of the desorption process. A variety of approaches have been suggested to extract this information. When the pumping rate is very large compared to the

desorption rate, the latter is directly proportional to the gas-phase pressure. In the simplest interpretation of the thermal desorption spectrum, the activation energy for the desorption process E_d is obtained from the temperature of the desorption peak maximum T_{max} using the following equation[21,29]:

$$\frac{E_d}{RT_{\max}^2} = \left(\frac{n_1}{b}\right) e^{\frac{-E_d}{RT_{\max}}} \qquad (2.11)$$

for first-order desorption where ν_1 is the pre-exponential factor, R is the universal constant of gases, and β is the temperature ramp (dT/dt). According to (2.11), T_{max} is independent of the initial coverage. By assuming a value of 10^{13} for the pre-exponential factor, the activation energy for desorption can be obtained. E_d is a good approximation of the heat of adsorption as long as the adsorption is a non-activated process. This assumption is implicitly applied whenever heats of adsorption are evaluated from TPD data.

Section 2.3 References

(1) Long, D. A. *Raman Spectroscopy*; McGraw-Hill International Book Company: New York, 1977.

(2) McCreery, R. L. *Raman Spectroscopy for Chemical Analysis*; Wiley-Interscience: New York, 2000; Vol. 157.

(3) Asher, S. A.; Johnson, C. R. *Science* **1984**, *225*, 311.

(4) Turro, N. J. *Modern Molecular Photochemistry*; University Science Books: Sausalito, 1991.

(5) Pankove, J. I. *Optical Processes in Semiconductors*; Dover Publications, Inc.: New York, 1971.

(6) Dollish, F. R.; Fateley, W. G.; Bentley, F. *Characteristic Raman Frequencies of Organic Compounds*; John Wiley & Sons, Inc.: New York, 1974.

(7) Bock, A. *Phys. Rev. B* **1995**, *51*, 15506.

(8) Fell, N. F.; Vanderhoff, J. A.; Pesce-Rodriguez, R. A.; McNesby, K. L. *J. Raman Spectrosc.* **1998**, *29*, 165.

(9) Pope, S. J. A.; West, Y. D. *Spectrochim. Acta, Part A* **1995**, *51*, 2011.

(10) Xie, S. B.; Rosynek, M. P.; Lunsford, J. H. *Appl Spectroscopy* **1999**, *53*, 1183.

(11) Cheng, C. P.; Ludowise, J. D.; Schrader, G. L. *Applied Spectroscopy* **1980**, *34*, 146.

(12) Brown, F. R.; Makovsky, L. E.; Rhee, K. H. *Applied Spectroscopy* **1977**, *31*, 563.

(13) Koningstein, J. A.; Gachter, B. F. *J. Opt. Soc. Am.* **1973**, *63*, 892.

(14) Zimmerer, N.; Kiefer, W. *Applied Spectroscopy* **1974**, *23*, 279.

(15) Chua, Y. T.; Stair, P. C. *J. of Catal.* **2000**, *196*, 66.

(16) *Cleveland Vibrator Company,* Cleveland, OH.

(17) *Mott Corporation,* Farmington, CT.

(18) Kim, S. H.; Somorjai, G. A. *J. Phys. Chem. B* **2000**, *104*, 5519.

(19) Mousty-Desbuquoit, C.; Riga, J.; Verbist, J. J. *Inorg. Chem.* **1987**, *26*, 1212.

(20) Ertl, G.; Kuppers, J. *Low Energy Electrons and Surface Chemistry*; Verlag Chemie: Weinheim, 1985.

(21) Woodruff, D. P.; Delchar, T. A. *Modern Techniques of Surface Science*; Cambridge University Press: Cambridge, 1994.

(22) Moulder, J. F.; Stickle, W. F.; Sobol, P. E.; Bomben, K. D. *Handbook of X-ray Photoelectron Spectroscopy*; Physical Electronics, Inc.: Eden Prairie, MN, 1995.

(23) *ESCA Operator's Reference Manual. ESCA Version 4.0 and Multi-Technique 2.0*; Physical Electronics, Inc.: Eden Prairie, MN, 1988.

(24) Redhead, P. A. *Vacuum* **1962**, *12*, 203.

(25) Cvetanovic, R. J.; Amenomiya, Y. *Catal. Rev.* **1972**, *6*, 21.

(26) Cvetanovic, R. J.; Amenomiya, Y. In *Advances in Catalysis*; Eley, D. D., Selwood, P. W., Weisz, P. B., Eds.; Academic Press, 1967; pp 103.

(27) Falconer, J. L.; Schwarz, J. A. *Catal. Rev. -Sci. Eng.* **1983**, *25*, 141.

(28) Bhatia, S.; Beltramini, J.; Do, D. D. *Catalysis Today* **1990**, *3*, 308.

(29) Somorjai, G. A. *Chemistry in Two Dimensions*; Cornell University Press: Ithaca, NY, 1981.

(30) Adamson, A. W. Physical Chemistry of Surfaces; Wiley: New York, 1990; pp 690.

l_o	l_r, **10 cm^{-1}**	l_r, **4000 cm^{-1}**
1064	1065.1	1852.4
488	488.2	606.4
244	244.1	270.4

Table 2.1 Wavelength of 10 and 4000 cm^{-1} Raman Shifted photons with three different wavelengths of incident photons. All wavelengths are given in nm.

Wavelength of Cyclohexane Peak, nm	**248.866**	**250.280**	**251.092**	**251.780**	**252.914**
Raman Shift of Cyclohexane Peak, cm^{-1}	**801.3**	**1028.3**	**1157.6**	**1266.4**	**1444.4**
022500_Cyclohexane_01.spe, pixel	367.505	469.672	527.414	577.723	659.491
022500_Cyclohexane_02.spe, pixel	367.372	469.529	527.816	577.552	659.400
022500_Cyclohexane_03.spe, pixel	367.319	469.573	527.564	577.703	659.402
022500_Cyclohexane_04.spe, pixel	367.307	469.298	527.565	577.620	659.382
022500_Cyclohexane_05.spe, pixel	367.278	469.394	527.392	577.491	659.137
022500_Cyclohexane_06.spe, pixel	367.355	469.466	527.792	577.622	659.429
Average Pixel Position	**367.356**	**469.489**	**527.591**	**577.619**	**659.374**
Standard Deviation	0.080	0.133	0.181	0.088	0.122
Upper 95% CL	367.420	469.595	527.735	577.689	659.471
Lower 95% CL	367.292	469.382	527.446	577.548	659.276
+/- of a pixel	0.064	0.106	0.145	0.070	0.098
+/- cm^{-1}	0.288	0.470	0.636	0.308	0.423

Table 2.2 Statistical analysis of wavelength calibration for CCD detector using cyclohexane.

Atom	Orbital (Auger Transition)	Sensitivity Factor
Au	$4f_{7/2}$	3.50
Ti	2p	2.00
Mg	(KLL)	2.40
Cl	2p	0.89
Cl	1s	0.30
O	1s	0.71
Al	2s	0.29

Table 2.3 XPS and AES atomic sensitivity factors.

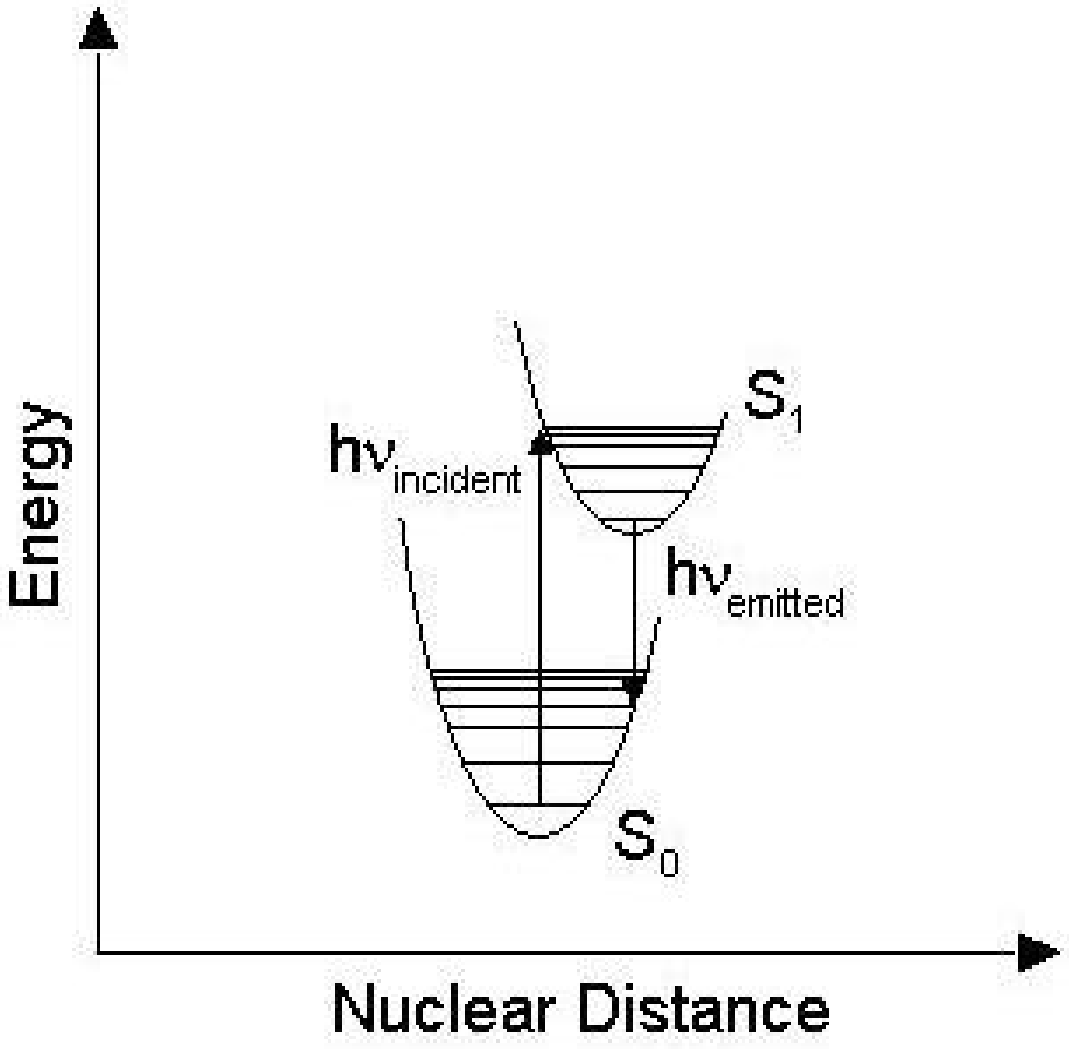

Figure 2.1 Simplified molecular orbital depiction of fluorescence process. S_o is the ground state singlet electronic state. S_1 is the first excited singlet state.

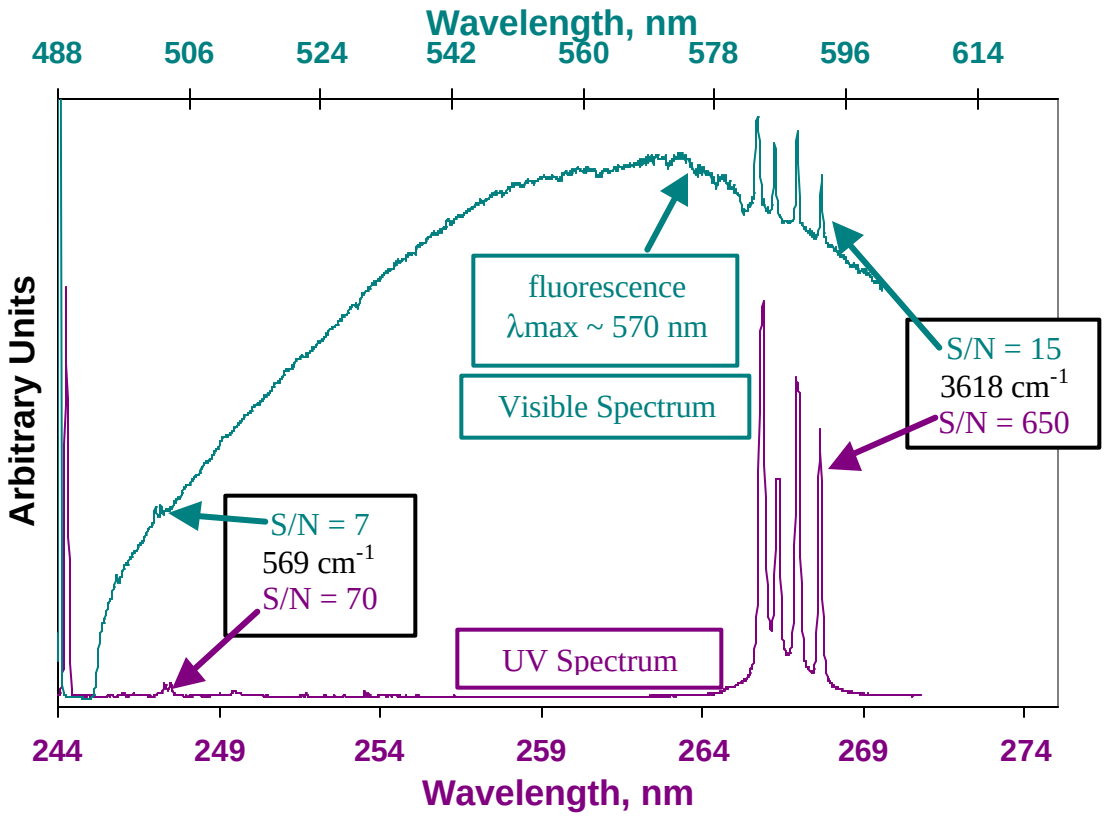

Figure 2.2 Comparison of Visible and UV Raman spectra of $Al_2O_3 \cdot 3H_2O$.

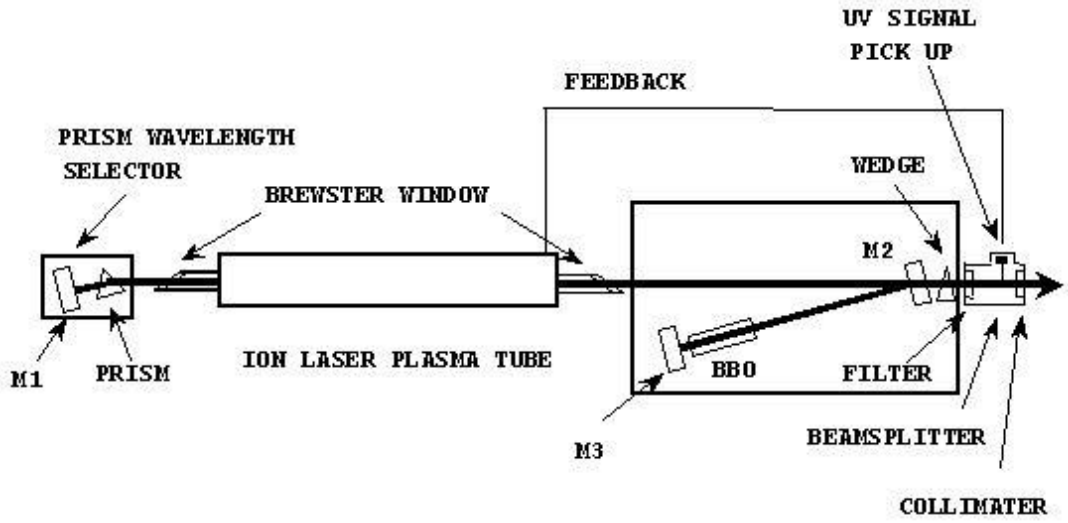

Figure 2.3 95-SHG laser cavity

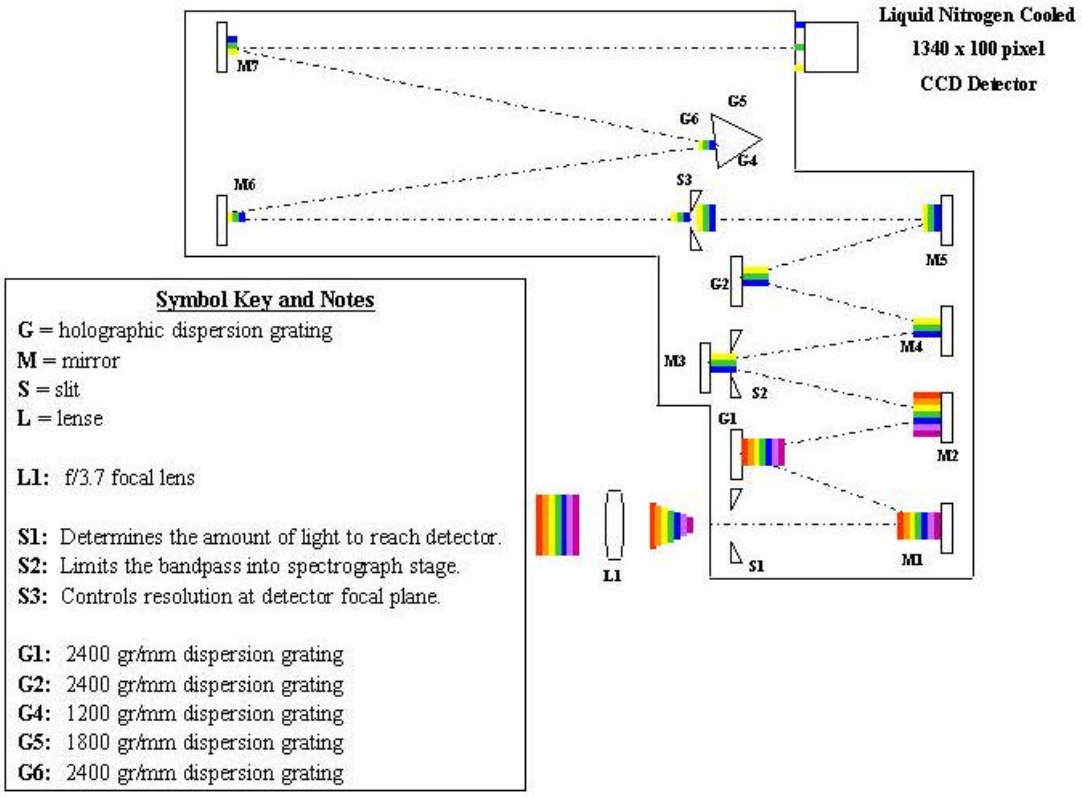

Figure 2.4 SPEX 1877 Triplemate spectrometer

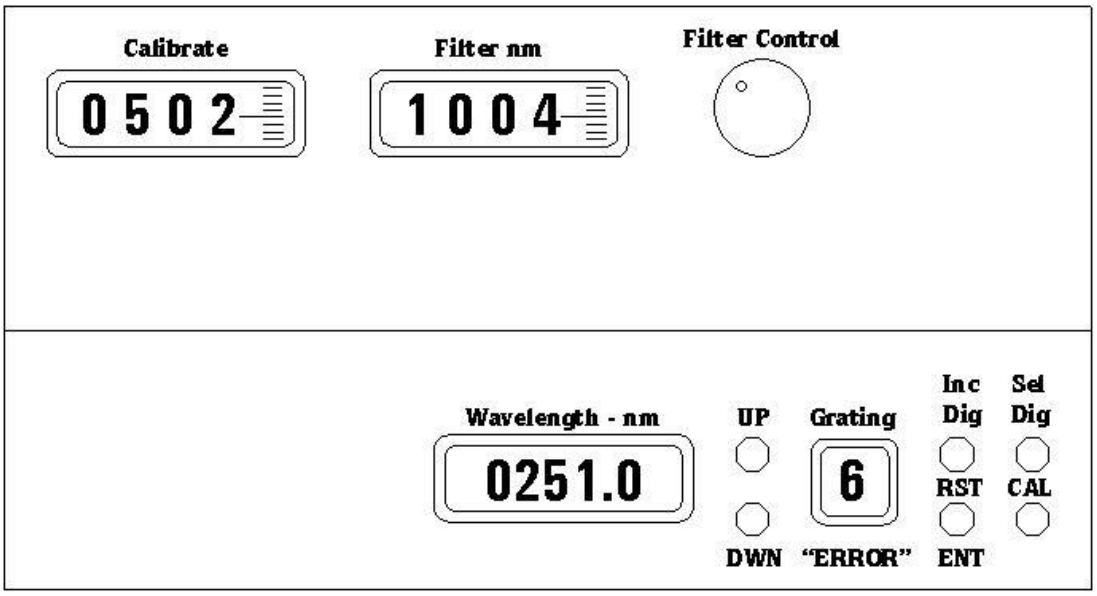

Figure 2.5 SPEX 1877 Triplemate control panel

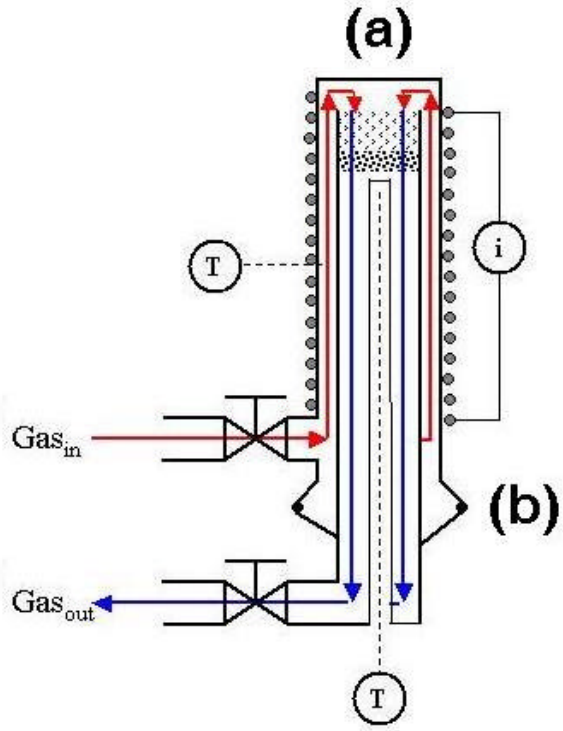

Figure 2.6 Glass packed bed UV-Raman reactor. The path of the gas flow is indicated by the arrows. (a) UV grade fused silica window, (b) viton O-ring to seal upper and lower parts, (T) K-type thermocouple, and (i) heating tape.

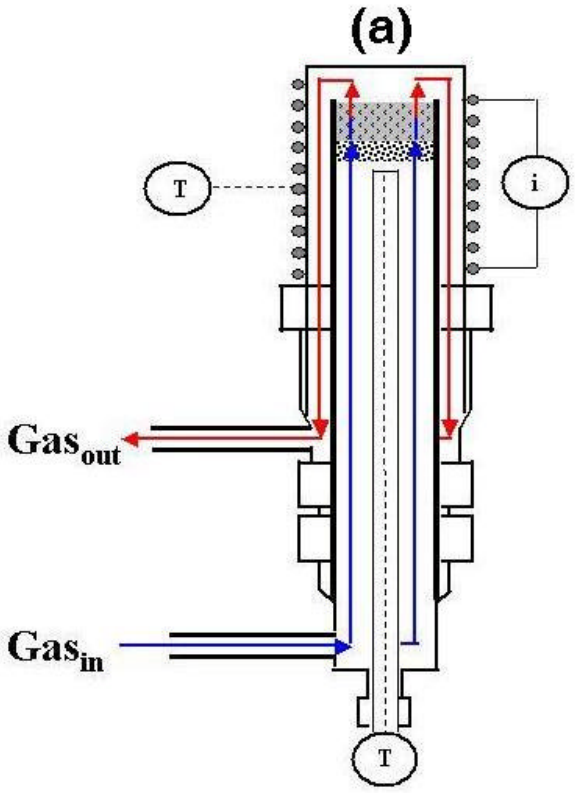

Figure 2.7 Stainless steel fluidized bed UV-Raman reactor. The path of the gas flow is indicated by the arrows. (a) UV grade fused silica window, (T) K-type thermocouple, and (i) heating tape.

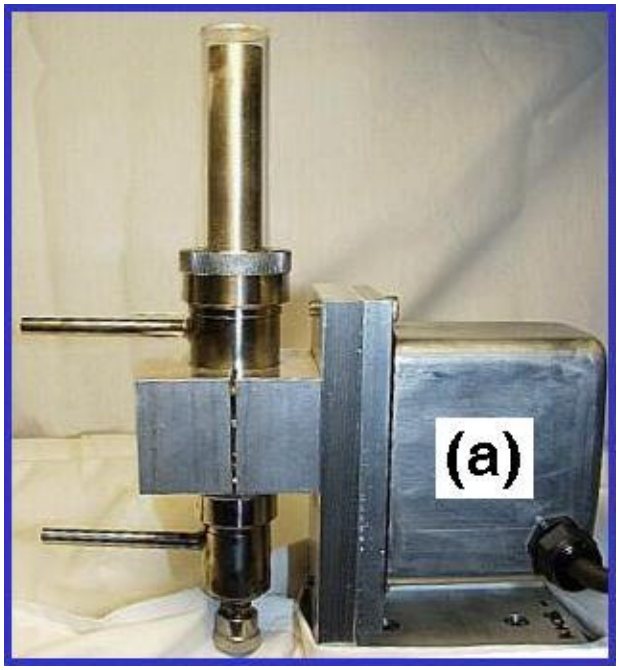

Figure 2.8 Photo of fluidized bed UV-Raman reactor with (a) electromagnetic shaker.

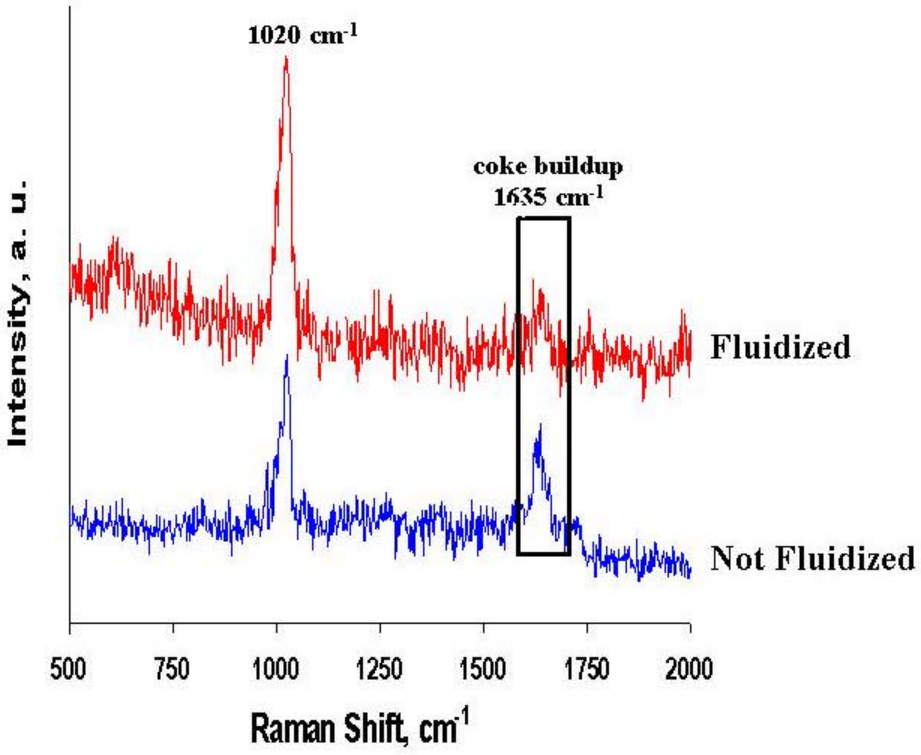

Figure 2.9 Pyridine adsorption on ZSM-5 zeolite in both the fluidized bed and packed bed reactors. The mode at 1020 cm^{-1} is attributed to the resonance enhanced ring breathing mode of pyridine. The peak at 1635 cm^{-1} is due to laser induced coke formation on the ZSM-5. The acquisition time and conditions of the two spectra are identical.

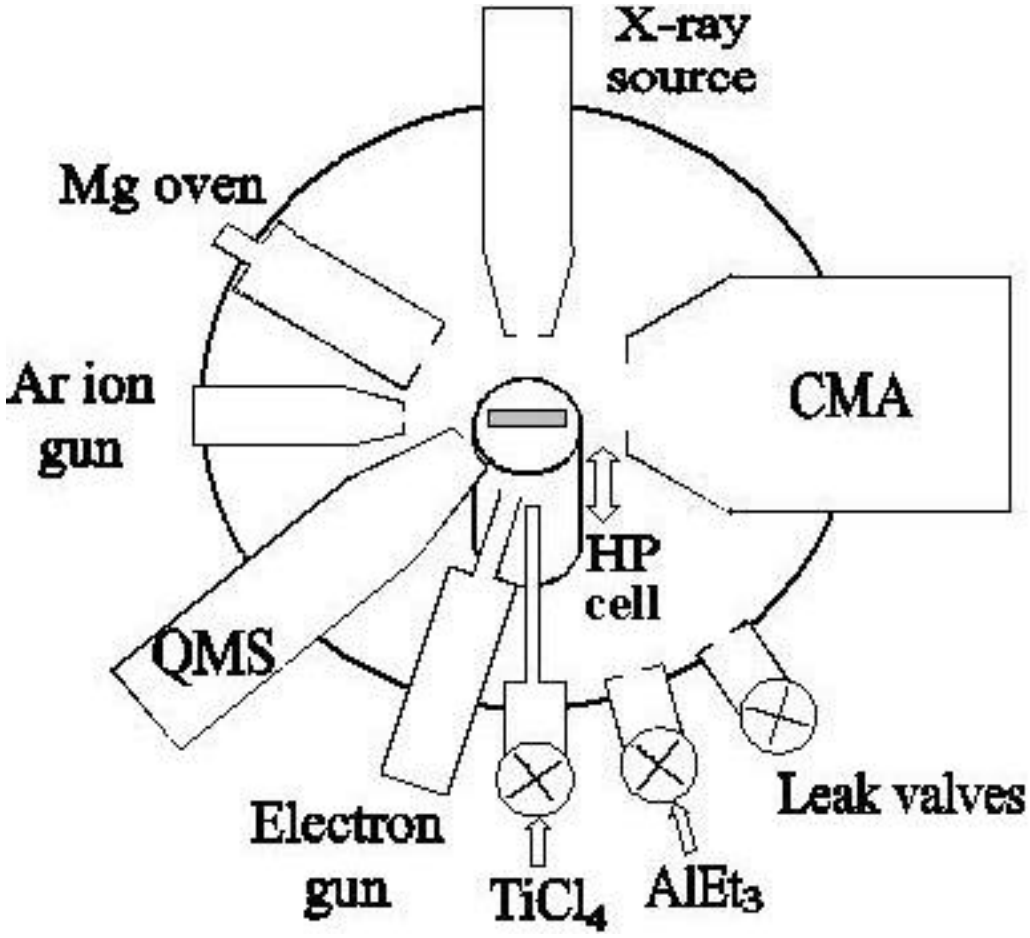

Figure 2.10 UHV Chamber employed for the study of model UHV Ziegler-Natta catalyst.

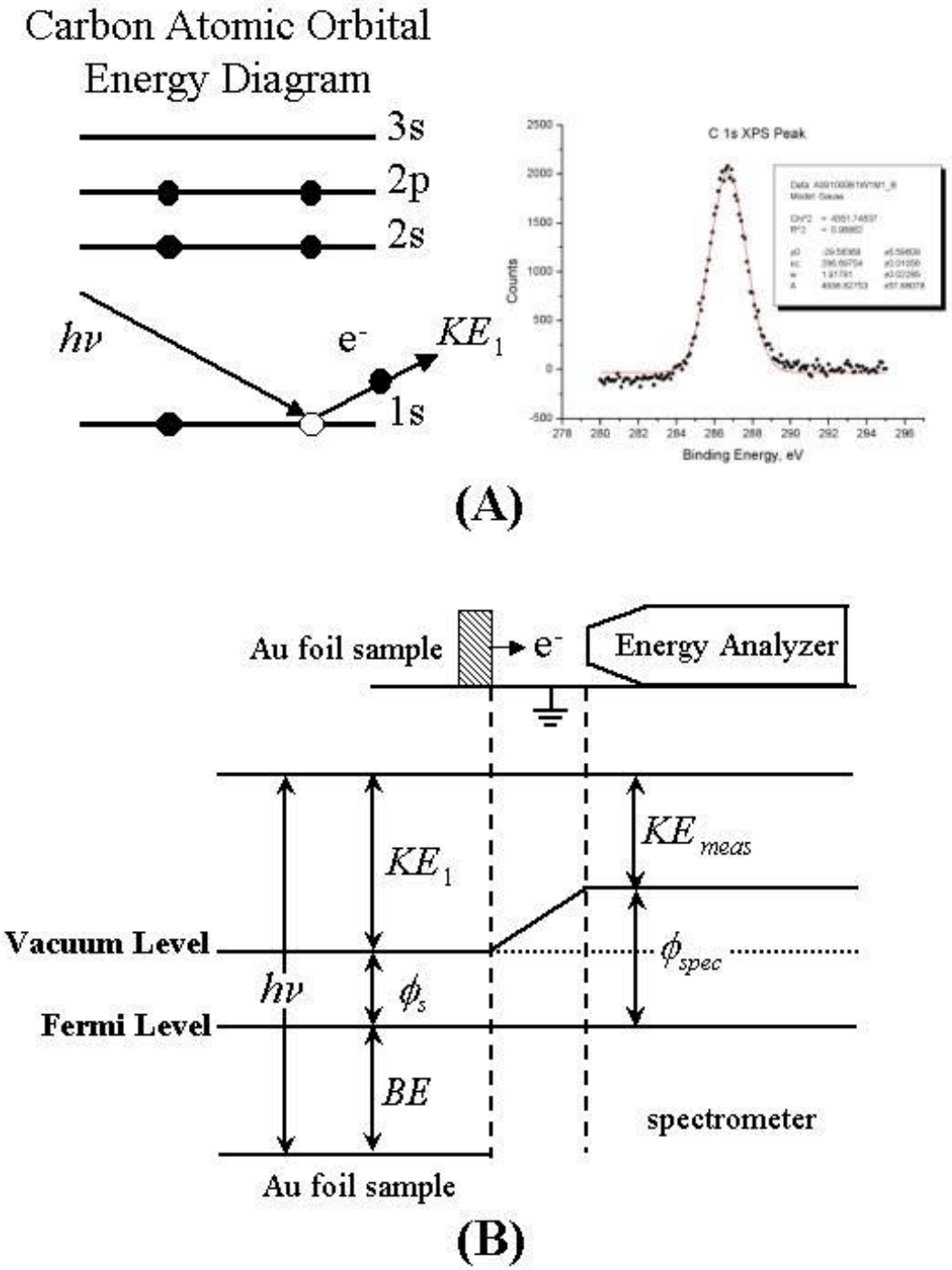

Figure 2.11 Depiction of the (A) XPS process for carbon 1s core electron and the resultant spectrum and (B) the energy level diagram relating the measured kinetic energy, KE_{meas}, to the binding energy, BE, of the sample.

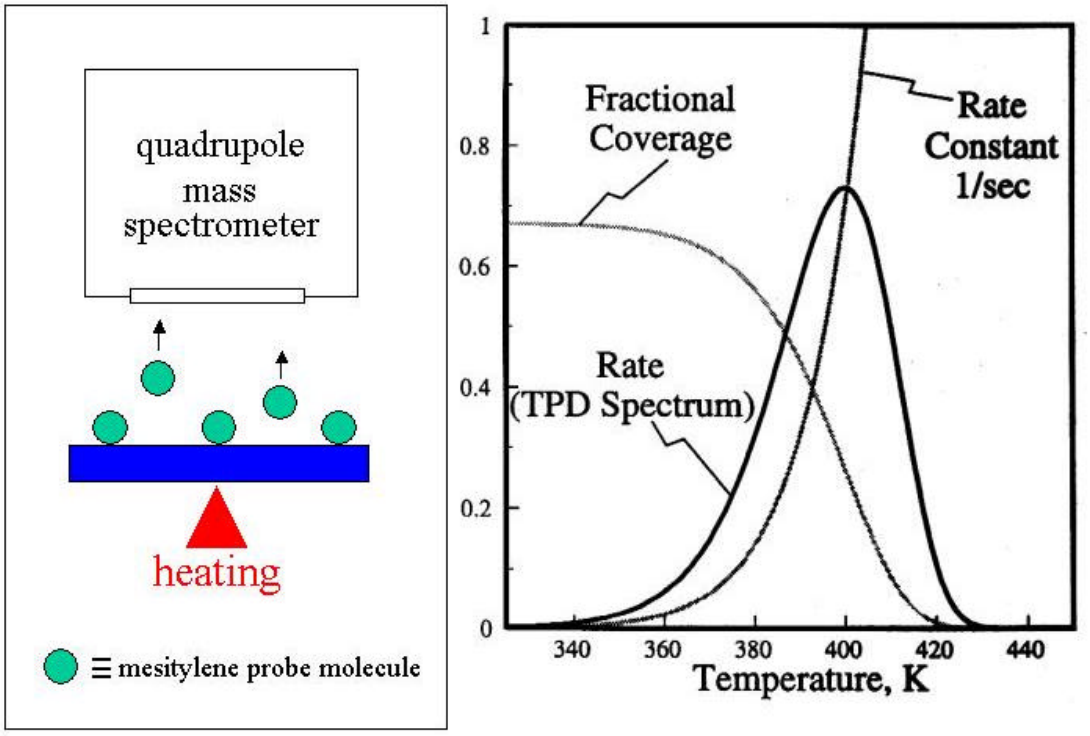

Figure 2.12 Depiction of a temperature programmed desorption (TPD) experiment.

Chapter 3

Surface Characterization of the $TiCl_x/MgCl_2$ Model Ziegler-Natta Polymerization Catalysts: Adsorption Site Studies Using Mesitylene Thermal Desorption

Section 3.1 Introduction

Identification of the active catalytic sites is one of the most difficult challenges in a $MgCl_2$-supported $TiCl_4$-based Ziegler-Natta polymerization catalysis system used for polyolefin production.[1,2] The ability to distinguish and monitor surface adsorption sites on the Ziegler-Natta catalysts can provide an unprecedented opportunity to correlate catalytic behaviors, such as polymerization activity and stereospecificity, with surface structure and composition. In addition, molecular-level knowledge of the surface adsorption sites is a prerequisite to controlling the active sites of the heterogeneous catalysts. If one can find a way to produce a single-site Ziegler-Natta catalyst, it would be possible to control the molecular weight distribution and stereospecificity of polymers to tailor their mechanical properties.[3-8]

For structure determination of flat surfaces, the most frequently used surface-science technique is low-energy electron diffraction (LEED).[9] This technique has been successfully used to study the surface structure of a model $MgCl_2$ film prepared by thermal evaporation in ultra high vacuum (UHV).[10,11] The surface of a multilayer $MgCl_2$ film has the structure of the $MgCl_2$ (001) basal plane. However, LEED would not be an appropriate technique for a titanium chloride film supported on $MgCl_2$ ($TiCl_x/MgCl_2$). First, the titanium species are not expected to have long-range order on

the supported catalyst that is necessary for diffraction.[12] Second, the primary electron beam of LEED will alter the film composition via electron-stimulated desorption (ESD) of chlorine.[10] The Ti-Cl bond of a $TiCl_x$ species would be more susceptible to electron-induced dissociation than the Mg-Cl bond of the $MgCl_2$ substrate. The ease of this process for $TiCl_x$ is expected because the Ti ion can exist in multiple oxidation states. Other techniques such as low-energy ion scattering (LEIS) cannot be employed for the polycrystalline films because a large single domain is required for data analysis.[13]

With these techniques using electrons or ions as a probe ruled out, temperature-programmed desorption (TPD) of organic molecules can be an alternative way to differentiate various surface adsorption sites of the catalysts if different sites exhibit different heats of desorption.[14] The key requirements to be an appropriate probe molecule are (1) strong and selective interaction with the various surface sites and (2) molecular adsorption and intact desorption without changing surface composition and structure. The second requirement is especially critical; otherwise, the effects of various surface treatments should be determined from TPD data of different samples. In this case, the catalyst samples must be prepared with extremely high reproducibility, that is, the same adsorption site distribution, which is unlikely in the preparation of the model Ziegler-Natta catalysts.

In a previous study, mesitylene was found to be a proper molecule for TPD characterization of the model Ziegler-Natta catalysts.[14] Due to the high stability of the conjugated π-electron ring, mesitylene exhibited no chemical reaction with the model catalyst upon adsorption and thermal desorption. The high polarizability of the aromatic ring produced strong interactions with the surface. Compared to the case of

benzene, the presence of three electron-donating methyl groups increased electron density in the aromatic ring, enhancing adsorbate-surface interactions.[15]

This work demonstrates that the mesitylene TPD technique is an effective way to identify and quantify the surface adsorption sites of the $TiCl_x/MgCl_2$ model Ziegler-Natta polymerization catalysts. For the as-prepared $TiCl_x/MgCl_2$ catalysts, two desorption peaks were observed in mesitylene TPD. On the basis of the topographic and structural knowledge of the film obtained with X-ray diffraction (XRD),[16-18] density functional theory,[19] scanning electron microscopy (SEM),[20,21] LEED,[10,11] and ion scattering spectroscopy (ISS),[22,23] two peaks were assigned to a site on the basal plane where the metal ions are hexagonally coordinated with six chlorine ions and a defective site where the metal ions are undercoordinated with chlorine ions. The latter sites could be found at the basal plane boundaries or crystallographic dislocations on the basal planes.[16-21]

The surface changes of the model catalyst, due to activation with triethylaluminum and propylene polymerization, could be followed by the peak temperature change of the mesitylene desorption. The mesitylene TPD technique has also suggested that bulk chlorine atoms can diffuse to the surface to fill the defect sites generated on the basal planes both by electron irradiation and by atomic Mg adsorption from the gas phase.[22,23] This diffusion process lowered the surface energy of the film to an equilibrium value. The mobility of bulk chlorine ions might suggest that the bulk chlorine atoms act as an inhibitor in surface reactions of the catalyst with electron donors (Lewis bases) to form stereospecific polymerization sites at the catalyst surface.

Section 3.2 Experimental Section

The experiments were performed in a UHV chamber equipped with a sputter ion gun for surface cleaning, an X-ray source, a double-pass cylindrical mirror analyzer (CMA) with a coaxial electron gun for X-ray photoelectron spectroscopy (XPS) and Auger electron spectroscopy (AES), and a quadrupole mass spectrometer (QMS) for residual gas analysis and TPD. The UHV chamber was pumped by a 2000 L/s diffusion pump and maintained a base pressure of about 1×10^{-9} Torr. A commercially available sample manipulator provided three-dimensional translation and 360^{o} rotation of the sample. The chamber also had three leak valves for gas exposure, a Mg evaporation source for the Mg dose, an electron flood gun for electron beam irradiation onto the sample, and an internal high-pressure reaction cell (HP) for in-situ polymerization. Further details were given elsewhere.[24] Gas admittance into the UHV chamber was controlled with leak valves facing the sample. Nominal pressures reported in this paper were readouts of the nude ion gauge, located about 20 cm away from the sample, without correction for ionization sensitivity and dosing geometry.

A polycrystalline Au foil (1.2 cm^2) was used as an inert substrate that could be heated resistively to 1000 K and cooled to 100 K. The surface temperature was measured using a K-type thermocouple attached to the back of the foil. The Au foil was cleaned with Ar ion sputtering followed by annealing at 900 K. Surface cleanliness was checked with XPS and AES. $TiCl_4$ and mesitylene (1, 3, 5-trimethylbenzene) were purified by several freeze-pump-thaw cycles.

Thin films of titanium chloride and magnesium chloride, $TiCl_x/MgCl_2$, were fabricated by codeposition of $TiCl_4$ and Mg metal on the Au foil at 300 K. During

deposition, the substrate faced both the Mg evaporation source and the $TiCl_4$ doser at 60^o with respect to the surface normal. Mg was evaporated from the Mg source during the $TiCl_4$ exposure. Adjusting the Mg source temperature (T_{Mg}) and exposure time controlled the Mg dose. With T_{Mg} = 600 K, the Mg flux on the Au substrate was estimated to be about 6 x 10^{12} atoms/cm^2·s.[24]

XPS was used to measure the surface composition and oxidation states. The X-ray source was positioned 55^o with respect to the surface normal and emitted the Al Kα line (1486.6 eV). The angle between the X-ray source and the CMA axis was 90^o. The Au $4f_{7/2}$ peak at 84 eV was taken as a reference for the energy scale. The titanium oxidation state distribution was obtained from the deconvolution of the Ti 2p XPS spectra with a series of synthetic peaks that represented the photoelectron emission from different oxidation states.[24,25]

In mesitylene TPD experiment, the deposited film was exposed to a given exposure (1 L = 1x10^{-6} Torr · s) of mesitylene and then resistively heated at a ramp rate of 4 K/s. The QMS ionizer was covered with a shroud that had an aperture of about 5 mm, positioned about 1 cm from the surface, to discriminate background desorption. QMS signals, up to 5 masses, were recorded with a computer.

As a reference surface for mesitylene TPD, $MgCl_2$ multilayers were deposited on Au at 300 K by thermal evaporation of $MgCl_2$ from a separate Knudsen cell, until no Au signal was observable in AES. XPS confirmed the stoichiometry of $MgCl_2$.

After high-pressure catalyst activation and propylene polymerization in the HP cell, the changes in surface composition and adsorption sites of the model catalyst film were studied using XPS and mesitylene TPD in UHV. The model catalyst was

activated by exposing it to ~1 Torr of triethylaluminum ($AlEt_3$) for 3 min at 300K. After the $AlEt_3$ was pumped out, 800 Torr of propylene was introduced and the catalyst temperature was increased to 343K.

Section 3.3 Results and Discussion

The film structure, composition, and titanium oxidation state distribution of the model catalyst film ($TiCl_x/MgCl_2$) are summarized briefly here. Mg was completely oxidized to Mg^{2+}, forming $MgCl_2$ multilayers. Most of the deposited $TiCl_x$ species were present at the film surface. The $TiCl_x/MgCl_2$ film was stable up to 400 K, above which $TiCl_4$ desorbed. More details have been described elsewhere.[24]

Mesitylene adsorbed molecularly on the $TiCl_x/MgCl_2$ film at 100 K and desorbed intact in the temperature range 170-350 K. The desorption profile of mesitylene was highly reproducible in the TPD experiments for a single sample, indicative of reversible mesitylene desorption without altering the catalyst surface composition. No hydrocarbon desorption was detected at temperatures higher than 350K. The peak desorption temperature decreased with increasing mesitylene exposure in the monolayer regime, indicative of repulsive interadsorbate interactions. For this reason, the mesitylene exposure in TPD was limited to lower than 1.5 L (about 30% of the monolayer saturation coverage) in order to avoid the effect of interadsorbate interactions in the desorption profile. A multilayer desorption peak appeared at about 175 K for exposures larger than ~4.5 L (data not shown).

Section 3.3.1 Identification of Surface Adsorption Sites. The mesitylene TPD of the $TiCl_x/MgCl_2$ film exhibited two distinct peaks at 205-220 and 260-273 K, as

shown in Figure 1a. The narrowness of the full width at half-maximum (fwhm ~ 20 K) implied that each peak corresponds to a single adsorption site. Hereafter, each site will be called A and B, respectively, for convenience. From their relative intensities, the site distribution on the catalyst surface was calculated to be 84% of the A site and 16% of the B site. Assuming first-order desorption kinetics and a pre-exponential value of 10^{13} s^{-1}, the mesitylene desorption energies from the A and B sites were calculated to be 12.3-13.3 kcal/mol and 15.9-16.6 kcal/mol, respectively.[26]

The mesitylene TPD profile for a $MgCl_2$ film is presented in Figure 1b. The multilayer $MgCl_2$ film was chosen as a reference because its surface structure has been determined with LEED[10,11] and its bulk crystalline structure is similar to those of titanium chlorides.[16-18] Two desorption peaks (A and B) were observed in the same temperature range as in Figure 1a. The widths (fwhm) of these two desorption peaks appeared to be the same. The relative ratio of A/B on the $MgCl_2$ film was about 70:30, indicating that the B site concentration was twice that of Figure 1a. Due to the repulsive nature of the lateral interactions between the adsorbates, the higher concentration of the B site on $MgCl_2$ lowered the peak temperature of mesitylene desorption from this site, in comparison to the data of Figure 1a (ΔT ~ 10 K for 1.4L). The lower mesitylene desorption temperature from the B site at higher concentration of the B site was also observed from the $TiCl_x/MgCl_2$ films (see Figures 2, 4, and 5).

The mesitylene TPD alone could not determine unambiguously the surface structure of the $TiCl_x/MgCl_2$ model Ziegler-Natta catalyst. However, one could deduce the surface structure corresponding to the A and B sites, observed in Figure 1, on the basis of (1) the similarity of the mesitylene TPD profiles for the $TiCl_x/MgCl_2$ and

$MgCl_2$ films, (2) the close analogy of the crystal structure for $MgCl_2$, $TiCl_2$, and $TiCl_3$,[1,16-18] (3) the shape of the microcrystals of $TiCl_3$,[20,21] (4) the surface structure of $MgCl_2$,[10,11] and (5) the surface composition of the $MgCl_2$ and $TiCl_x/MgCl_2$ films.[22,23] These halide crystals have a layered structure, each layer consisting of two monoatomic layers of chlorine atoms octahedrally coordinated to intercalating metal atoms. The surface energies of the (001) basal planes of these crystals are the lowest, owing to the very weak interaction (dispersive interaction) between the neighboring layers.[19] Therefore, the majority of the film surfaces of $TiCl_x/MgCl_2$ and $MgCl_2$ will adopt the basal plane structure to lower the film surface energy. The SEM images of the $TiCl_3$ films[20,21] and LEED studies of the $MgCl_2$ multilayer film[10,11] confirmed that the surfaces of these films consist of small platelets with the (001) basal plane structure. Since the desorption peak (205-220 K) from the A site was dominant in the mesitylene TPD (Figure 1), the A site could be attributed to the (001) basal plane. This site would be called *a coordinatively saturated site* because the metal ions under the chlorine layer are coordinated with six chlorine atoms.

Since the heat of mesitylene desorption was higher for the B site than the A site, the surface structure of the B site must be different from that of the A site. The He^+ ISS studies of the model Ziegler-Natta catalysts films[22,23] found that the surfaces of these films are terminated with chlorine ions and no metal ions are exposed to vacuum. So it was unlikely that the high-temperature desorption peak originated from mesitylene molecules directly adsorbed to metal ions. To distinguish from the A site, the B site would be called *a coordinatively unsaturated site* where the metal ions under the chlorine layer are undercoordinated. Since the majority of the film surface had the

(001) basal plane structure, these minor sites (15-30% depending on the deposition conditions) could be the crystallographic dislocations on the basal plane formed during the crystal growth,[20] or other crystallographic planes at the boundaries of the (001) basal plane.[21]

Even though the data could not select the most plausible structure, the presence of only one peak attributable to the undercoordinated site suggested that only one structure appeared dominant among various possible structures. Busico et al. suggested the presence of the (100) and (110) planes on the small $MgCl_2$ particulates.[27] The $MgCl_2$ (100) surface has the Mg atoms coordinated to five chlorine atoms. The $MgCl_2$ (110) surface has the Mg atoms coordinated to four chlorine atoms. If these surfaces retain their bulk-terminated structure without any reconstruction, the mesitylene TPD would distinguish these two surface structures. However, the fact that there was only one defect peak indicated these energetically unstable surfaces undergo significant reconstruction to lower the surface energy,[19] leading to a structure with the chlorine densities similar to each other.

One of the goals of probe-molecule TPD characterization of the model Ziegler-Natta catalysts was to quantify the Ti concentration at the catalyst surface. Unfortunately, mesitylene TPD could not distinguish the titanium-containing site from the magnesium-containing site. This could be attributed to the chlorine termination of the catalyst surface.[11,22,23] Metal chlorides always tend to have a chlorine-terminated surface to lower the system surface energy.[19] On these surfaces, the main interactions of the physisorbed mesitylene molecule with the surface would be van der Waals

interactions between the adsorbate and the chlorine layer whose atomic densities were determined by the metal coordination under the layer.

For metal-specific TPD characterization, chemisorption of a small molecule might be required. In this case, however, the chemisorbed probe molecule would not desorb below the polymerization temperature and would alter the surface composition of the catalyst. When dimethyl ether, one of the weakest Lewis bases, was used as a probe molecule, a small fraction of the adsorbed molecules desorbed along with the titanium species at T > 450K.[14] Stronger Lewis bases, for example, ethyl benzoate used as an internal electron donor, could replace the titanium chloride species chemisorbed on the $MgCl_2$ surface.[1,2] Petts and Waugh studied the adsorption isotherm of allene (a weak poison for ethylene and propylene polymerization) on the $TiCl_3$-based high-surface-area catalysts and found that a certain fraction of the allene was irreversibly adsorbed; that is, the desorbed amount was always less than the adsorbed amount.[28] It should be noted that, even with the weak poison probe, they found only two adsorption sites on the powdered sample, with a low-temperature site being dominant, consistent with this data.

Section 3.3.2 Catalyst Activation and Propylene Polymerization. After reacting with $AlEt_3$ (cocatalyst) the model $TiCl_x/MgCl_2$ catalyst film was active for the gas-phase polymerization of propylene. Figure 2 presents the XPS and mesitylene TPD data obtained with a single catalyst film at various stages of the polymerization process. The fresh $TiCl_x/MgCl_2$/Au film showed the Mg, Ti and Cl signals of the catalyst as well as the Au substrate signal in XPS and two types of the surface adsorption sites (A/B = 78:22) in mesitylene TPD (Figure 2a). Compared to Figure 1, the desorption

temperature of the B site in Figure 2 was lower due to a higher concentration of the B site (22% in Figures 2 and 16% in Figure 1). At a higher defect concentration, the mesitylene molecules adsorbed at the defect sites will feel more repulsive interadsorbate interactions, leading to desorption at a lower temperature.

After catalyst activation by the reaction with about 1 Torr of $AlEt_3$ for 3 min at 300 K, XPS (Figure 2b) showed the reduction of Ti^{4+} and Ti^{3+} species into Ti^{2+} species (Table 1) and a slight decrease in the Cl signal and a slight increase in the C signal (most likely C_2H_5), indicative of surface alkylation. This was consistent with a previous study.[29] These surface changes lowered the mesitylene desorption temperature to a different extent for the A and B sites (Figure 2b), indicative of weaker interactions of mesitylene with the activated surface species. It appeared that the alteration of the mesitylene desorption profile was caused more likely by the alkylation, not by the metal reduction, because the mesitylene TPD was not sensitive to the metal identity (Figure 1) or oxidation state (see Figure 3) under the outermost chlorine layer. However, it should be noted that the alkylation and reduction of the catalyst are not separate processes; that is, both result from the $AlEt_3$ alkylation.

Accepting the structural assignments for the surface sites from section 3.3.1 and the reaction stoichiometry data reported by Rodriguez et al.,[30] one could describe the surface alkylation by $AlEt_3$ as replacement of one Cl ligand with one C_2H_5 group for the coordinately saturated site (A) and addition of one C_2H_5 group to the undercoordinated site (B). Then, the slight decrease (about 6K) of the mesitylene desorption temperature for the A site could be attributed to a slightly lower polarizability of the C_2H_5 group that replaced the Cl anion.[30] The large decrease (about 16 K) of the mesitylene desorption

temperature for the B site could imply that the addition of an extra ligand group weakens the mesitylene-surface interaction more than expected for the replacement of the exiting ligand group.[30,31] The observed difference in the effects of the alkylation for two sites was consistent with report of Petts and Waugh that, among two sites, the heat of allene adsorption on the high-energy adsorption site was affected more significantly by the aluminum alkyl activation.[28]

Figures 2c and d show the XPS and mesitylene TPD data for the activated catalyst after being used for polymerization with ~800 Torr of propylene at 343 K. The polymerization process was interrupted 20 min after monomer introduction to the reaction cell in order to monitor the surface changes of the catalyst film at an early stage of polymerization (Figure 2c). XPS showed the C 1s signal (285 eV) of a thin polymer film on the catalyst and no observable signals of the catalyst film (Mg, Ti, and Cl). The attenuated Au substrate signal was still observable, indicating that the polymer film produced on the catalyst was not very thick. In mesitylene TPD, the peak desorption temperature was shifted to about 170 K, characteristic of the mesitylene desorption from a polypropylene film (as shown in Figure 2d with a dashed curve). It should be noted that the mesitylene TPD profile in Figure 2c had a high-temperature shoulder peak reaching up to about 230 K. Since the polypropylene surface cannot have a mesitylene desorption peak above 170 K, the high-temperature shoulder peak indicated that mesitylene can still reach the active sites at this stage of polymerization. This might indicate the polymer contained large pores to allow mesitylene adsorption to the active sites under the polymer layers. Upon reintroduction of monomer (propylene) and polymerization for 14 h, a thick film of polypropylene was grown on the catalyst

surface, showing only the C 1s signal in XPS and the 170 K peak in mesitylene TPD (Figure 2d).[32] In conclusion, these data proved that mesitylene TPD can be an effective technique to monitor the active sites present on the Ziegler-Natta catalyst at early stages of the polymerization process.

Section 3.3.3 Surface Modification: Diffusion of Bulk Chlorine to the Surface. The surface modification was attempted in three ways: (1) annealing, (2) electron irradiation, and (3) Mg metal dose. The annealing method was tested first because it is a commonly used process to reduce surface and bulk defect concentrations. The second and third methods were tested to produce undercoordinated sites at the surface by removing Cl^- from the surface and deposting extra Mg atoms onto the surface, respectively. The remainder of this section will describe each case in detail.

(1) *Postdeposition Annealing.* Annealing of the catalyst film (used in Figure 1a) at 640 K removed some fraction of the chemisorbed titanium chloride species via $TiCl_4$ desorption, leading to reduction of both the concentration and the oxidation state distribution of the titanium chloride species.[24] In XPS measurements after the 640 K annealing, the Mg_{KLL} signal intensity increased by ~30% while the Ti_{2p} signal intensity decreased by ~50%, compared to those before the annealing. Table 2 shows that the 640 K annealing decreased the Ti^{4+} state and increased the Ti^{2+} state in the Ti oxidation state distribution. However, Figure 3 shows that the peak temperature and relative intensity of the mesitylene desorption profile were not changed significantly by the 640 K annealing, indicating that the heat of mesitylene desorption was not sensitive to the annealing effect. The only discernible change was a slight depression of the desorption profile in the temperature range 220-240 K.

This result could be attributed to the chlorine termination of the catalyst film.[10,11,22,23] The mesitylene molecules adsorbed on the chlorine layer. The changes in the oxidation state and concentration of the Ti species under the chlorine layer were not reflected in the mesitylene desorption profile. No discernible change in the relative intensities of the A and B sites might suggest that there is no significant change in the average size of the crystallites or the structural arrangement of the chlorine ions at the surfaces of these crystallites. However, more detail could not be discerned with the mesitylene TPD alone.

(2) *Electron irradiation at 150 K.* Electron irradiation of the halide solid is known to cause desorption of surface chlorine.[33] Figure 4 illustrates the effect of low-energy electron irradiation of the $TiCl_x/MgCl_2$ film on the mesitylene TPD profile. First, it should be noted in Figure 4a that the as-deposited film showed two mesitylene desorption peaks corresponding to the A and B sites-a characteristic feature of the nonirradiated film-and no change in the mesitylene desorption profile with repeated TPD experiments up to 380 K. When the film was irradiated with 50 eV electrons (6×10^{16} electrons/cm^2) at 150 K, the mesitylene desorption profile lost its two-peak feature and shifted its peak maximum to 222 K (Figure 4b). This result indicated that the electron-induced loss of chlorine created a new adsorption site structure whose heat of mesitylene desorption was between those of A and B sites on the as-deposited film. If electron-induced chlorine desorption occurred statistically, not from a preferential site, many electron-induced defect sites would be generated on the basal planes because the majority of the film surface assumed the basal plane structure.

In repeating the TPD experiment for the same film, the two-peak desorption feature characteristic of the nonirradiated films appeared again. Heating to 380 K appeared to be enough to anneal the electron-irradiated film surface and recover the original surface structure before electron irradiation. This result could indicate that, during the TPD run, bulk chlorine atoms diffuse and fill the electron-induced defect sites, lowering the surface energy of the plane.

Figure 4c shows the effect of 200 eV electron irradiation at 150 K. With the same electron dose (6×10^{16} electrons/ cm^2), more noticeable changes were observed in the mesitylene desorption profile and more heating cycles were required to recover the original desorption profile. The enhanced electron-irradiation effect could be explained with a secondary electron effect. At higher energy of the incident electrons, more secondary electrons are generated[34-36] and participated in the electron-stimulated desorption of chlorine, leading to more damage on the film surface.

Electron irradiation at 150 K altered the film surface at a much lower dose than that for electron irradiation at 300 K. In previous studies, ion scatting spectroscopy (ISS) showed that electron irradiation of titanium chloride and $MgCl_2$ films at 300 K exposed metals at the film/vacuum interface only after extended irradiation of the film with a focused beam of 1keV electrons.[22,23] However, with the current irradiation conditions (small electron dose at 150 K), no Mg^0 was detected in XPS while the mesitylene TPD monitored the formation of chlorine-deficient sites at the surface. This higher efficiency at low temperature could be attributed to suppression of the chlorine diffusion from the bulk at low temperature.

(3) *Metallic Mg Dose at 150 K.* An attempt was made to produce Mg adatoms on the $TiCl_x/MgCl_2$ catalyst surface by depositing Mg atoms at 150 K. The deposition rate of Mg was about half a monolayer per minute. Figure 5 compares the mesitylene desorption profiles for the as-depostied film and the Mg-dosed films. The data showed no change in the mesitylene TPD profile with the Mg doses on the $TiCl_x/MgCl_2$ film, indicating that the Mg adatoms were immediately covered with chlorine atoms. This result could be explained with the reaction of the adsorbed Mg atoms with the $TiCl_x(Ti^{4+})$ species in the surface layer even at 150 K.[37]

It is interesting to note that the Mg atom doses at 150 K did not produce any change in the surface adsorption site structure (Figure 5) while the electron-induced desorption of chlorine at 150 K produced a new adsorption site structure that was removed by chlorine diffusion only at higher temperatures (Figure 4). In the case of the Mg dose onto the film, the adsorbed Mg atoms energetically favored reaction with $TiCl_x(Ti^{4+})$ species in the surface layer rather than with the $MgCl_2$ species.[24] This process reduced the Ti oxidation state and converted the Mg adatoms to $MgCl_2$, recovering the chlorine-terminated surface structure. In contrast, the hyperthermal electron irradiation removed chlorine atoms from both Mg^{2+} and Ti^{4+} species in the surface layer. In addition, it altered the underlayer composition. For electrons of a kinetic energy of 5-200 eV, the inelastic mean free path of electrons is typically on the order of 5-10Å,[38] which is about 2-3 times the c-axis of the $MgCl_2$ unit cell.[11] Therefore, the electron-induced process altered the surface composition and structure more significantly than the Mg dose producing more prominent changes in the mesitylene desorption profile.

Section 3.3.4 Implications to the Catalyst Preparation and Polymerization.

Lowering of the surface energy by diffusion of bulk chlorine atoms to the surface defects, observed in these experiments, will provide insights into the dynamic roles of the $MgCl_2$ substrate in reactions with $TiCl_4$ and ethyl benzoate (internal Lewis base). For preparation of high-surface-area catalysts, comilling of $MgCl_2$ with $TiCl_4$ always gives more $MgCl_2$ size reduction and more $TiCl_4$ incorporation, compared to milling of $MgCl_2$ alone followed by reaction with $TiCl_4$.[39-41] Ethyl benzoate or ethanol are often comilled with $MgCl_2$ to stabilize newly exposed faces that are created by the milling action and are responsible for stereospecific polymerization of propylene.[42-44] The efficacy of the comilling processes can now be understood in light of the fast diffusion of bulk chlorine to the surface from the bulk. When $MgCl_2$ is milled alone, the undercoordinated sites produced during the milling process will be immediately chlorinated by the chlorine atoms from the bulk, lowering the concentration of the binding sites for $TiCl_4$ and ethyl benzoate.

The importance of the undercoordinated sites in stereospecific polymerization of propylene has been studied by correlating the mesitylene TPD profile for the model catalyst produced by different methods and the isotacticity of the polypropylene produced with these model catalysts.[45] When a $MgCl_2$-free model catalyst was prepared by electron-induced deposition of $TiCl_4$, the A site in the mesitylene TPD (basal plane structure) was absent and the gas-phase polymerization without any Lewis base produced exclusively isotactic polypropylene. When a model catalyst was produced by the codeposition of Mg and $TiCl_4$, the mesitylene TPD showed the same profile as reported in this work and both atactic and isotactic polypropylene were

produced. In the former case, the simultaneous and continuous irradiation of electrons during the catalyst deposition seemed to be responsible for removal of chlorine from the film, lowering the formation of the basal plane structure on the film surface. These studies showed that the capability to titrate the surface adsorption site distribution would be expected to aid understanding of stereospecific polymerization.

Section 3.4 Conclusions

TPD of mesitylene has been shown to be an efficient method for surface adsorption site characterization of the model Ziegler-Natta polymerization catalyst films. The mesitylene TPD for the $TiCl_x/MgCl_2$ film indicated the presence of two distinct adsorption site structures that have different chlorine arrangements. The dominant site was a coordinately saturated site of the basal plane structure. The minor site was tentatively attributed to a coordinatively unsaturated site at the basal plane boundaries or defects. Due to the chlorine termination of the catalyst surface, the mesitylene TPD could not distinguish the identity and oxidation state of the metals under the chlorine layer. The catalyst activation by $AlEt_3$ was accompanied by a lowering of the mesitylene desorption temperature from the alkylated sites. The catalyst film revealed a remarkably high diffusion rate of the bulk chlorine atoms to the surface to fill chlorine-deficient defect sites that were generated by Cl removal from the basal plane or Mg addition to the basal plane.

Section 3.5 References

(1) Barbe, P. C.; Cecchin, G.; Noristi, L. *Adv. Polym. Sci.* **1987**, *81*, 1.

(2) Dusseault, J. J. A.; Hsu, C. C. *J. M. S.- Rev. Macromol. Chem. Phys.* **1993**, *C33*, 103.

(3) Floyd, S.; Heiskanen, T.; Tayor, T. W.; Mann, G. E. *J. Appl. Polym. Sci.* **1987**, *33*, 1021.

(4) Shiono, T.; Hagihara, H.; Ikeda, T.; Soga, K. *Polymer* **1997**, *38*, 6409.

(5) Misra, S.; Lu, F. M.; Spruiell, J. E.; Richeson, G. C. *J. Appl. Polym. Sci.* **1995**, *56*, 1761.

(6) Andreassen, E.; Myhre, O. J.; Hinrichsen, E. L.; Grostad, K. J. *J. Appl. Polym. Sci.* **1994**, *52*, 1505.

(7) Ogawa, T. *J. Appl. Polym. Sci.* **1992**, *44*, 1869.

(8) Flood, J. E.; Nulf, S. A. *Polym. Eng. Sci.* **1990**, *30*, 1504.

(9) Somorjai, G. A. Chapter 2. In *Introduction to Surface Chemistry and Catalysis*; John Wiley and Sons: New York, 1994.

(10) Fairbrother, D. H.; Roberts, J. G.; Rizi, S.; Somorjai, G. A. *Langmuir* **1997**, *13*, 2090.

(11) Fairbrother, D. H.; Roberts, J. G.; Somorjai, G. A. *Surf. Sci.* **1998**, *399*, 109.

(12) Hasebe, K.; Mori, H.; Tomitori, M.; Keii, T.; Terano, M. *J. Mol. Catal. A* **1997**, *115*, 259.

(13) Woodruff, D. P.; Delchar, T. A. In *Modern Techniques of Surface Science*; 2nd ed.; Cambridge University Press: London, 1994; pp 292.

(14) Kim, S. H.; Somorjai, G. A. *Appl. Surf. Sci.* **2000**, *161*, 333.

(15) Bruggerman, K.; Czernuszewicz, R. S.; Kochi, K. J. *J. Phys. Chem.* **1992**, *96*, 4405.

(16) Giunchi, G.; Allegra, G. *J. Appl. Chrystallogr.* **1984**, *17*, 172.

(17) Allegra, G. *Macromol. Symp.* **1995**, *89*, 163.

(18) Kashiwa, N. *Polym. J.* **1980**, *12*, 603.

(19) Lin, J. S.; Catlow, C. R. A. *J. Mater. Chem.* **1993**, *3*, 1217.

(20) Rodriguez, L. A. M.; Van Looy, H. M. *J. Polym. Sci. Pat A* **1966**, *4*, 1971.

(21) Guttman, J. Y.; Guillet, J. E. *Macromolecules* **1968**, *1*, 461.

(22) Magni, E.; Somorjai, G. A. *Surf. Sci.* **1995**, *341*, L1078.

(23) Magni, E.; Somorjai, G. A. *Surf. Sci.* **1996**, *345*, 1.

(24) Kim, S. H.; Somorjai, G. A. *J. Phys. Chem. B* **2000**, *104*, 5519.

(25) Mousty-Desbuquoit, C.; Riga, J.; Verbist, J. J. *Inorg. Chem.* **1987**, *26*, 1212.

(26) Redhead, P. A. *Vacuum* **1962**, *12*, 203.

(27) Busico, V.; Corradini, P.; De Martino, L.; Proto, A.; Albizzati, E. *Makromol. Chem* **1986**, *187*, 1115.

(28) Petts, R. W.; Waugh, K. K. *Polymer* **1982**, *23*, 897.

(29) Magni, E.; Somorjai, G. A. *Surf. Sci.* **1997**, *377*, 824.

(30) Rodriguez, L. A. M.; Van Looy, H. M.; Gabant, J. A. *J. Polym. Sci. Pat A* **1966**, *4*, 1905.

(31) Arlman, E. J.; Cossee, P. J. *Journal of Catalysis* **1964**, *3*, 99.

(32) Kim, S. H.; Magni, E.; Somorjai, G. A. *Stud. Surf. Sci. Catal.* **2000**, *130*, 3861.

(33) Tokutaka, H.; Prutton, M.; Higginbotham, I. G.; Gallon, T. E. *Surf. Sci.* **1970**, *1*, 233.

(34) Shih, A.; Hor, C. *IEEE Trans. Electron Devices* **1993**, *40*, 824.

(35) Farhang, H.; Napchan, E.; Blott, B. H. *J. Phys. D: Appl. Phys.* **1993**, *26*, 2266.

(36) Kim, S. H.; Somorjai, G. A., Manuscript in preparation for publication.

(37) *In a separate experiment, we dosed Mg atoms on a condensed layer of $TiCl_4$ at 100 K. No metallic Mg atoms were detected in XPS measured at 100 K.*

(38) *Reference 9*, 383.

(39) Giannini, U. *Makromol. Chem. Suppl.* **1981**, *5*, 216.

(40) Galli, P.; Barbe, P. C.; Guidetti, G.; Zannetti, R.; Marigo, A.; Bergozza, M.; Fichera, A. *European Polymer Journal* **1983**, *19*, 19.

(41) Kashiwa, N.; Toyota, A. *Polym. Bull.* **1984**, *11*, 471.

(42) Chien, J. C. W.; Wu, J.; Kuo, C. *J. Polym. Sci. Polym Chem. Ed.* **1983**, *21*, 737.

(43) Keszler, B.; Bodor, G.; Simon, A. *Polymer* **1980**, *21*, 1037.

(44) Sergeev, S. A.; Bukatov, G. D.; Zakharov, V. A. *Makromol. Chem* **1983**, *184*, 2421.

(45) Kim, S. H.; Somorjai, G. A. *J. Phys. Chem. B* **2001**, *105*, 3922.

$AlEt_3$ activation[c]	Ti oxidation state				
	4+	3+	2+	1+	0
before	46	26	20	8	0
after	39	18	39	4	0

Table 3.1 Effect of the $AlEt_3$ activation on the Ti oxidation state distribution (%) in the $TiCl_x$ / $MgCl_2$ film deposited by reaction of Mg with $TiCl_4$.[a,b]

a. XPS Measurement: 300K
b. $P(TiCl_4) = 2 \times 10^{-7}$ Torr, T_{Mg} = 610 K, deposition time = 10 min
c. $P(AlEt_3)$ = 1 Torr, T_{sample} = 300 K, reaction time = 3 min

	Ti oxidation state				
annealing at 640 K	4+	3+	2+	1+	0
before[c]	29	24	46	0	1
after[d]	8	12	65	6	9

Table 3.2 Effect of the annealing on the Ti oxidation state distribution (%) in the $TiCl_x$ / $MgCl_2$ film deposited by reaction of $TiCl_4$.[a,b]

a. XPS Measurement: 300K
b. $P(TiCl_4) = 1 \times 10^{-7}$ Torr, T_{Mg} = 600 K, deposition time = 10 min
c. Figure 3.1
d. Figure 3.3

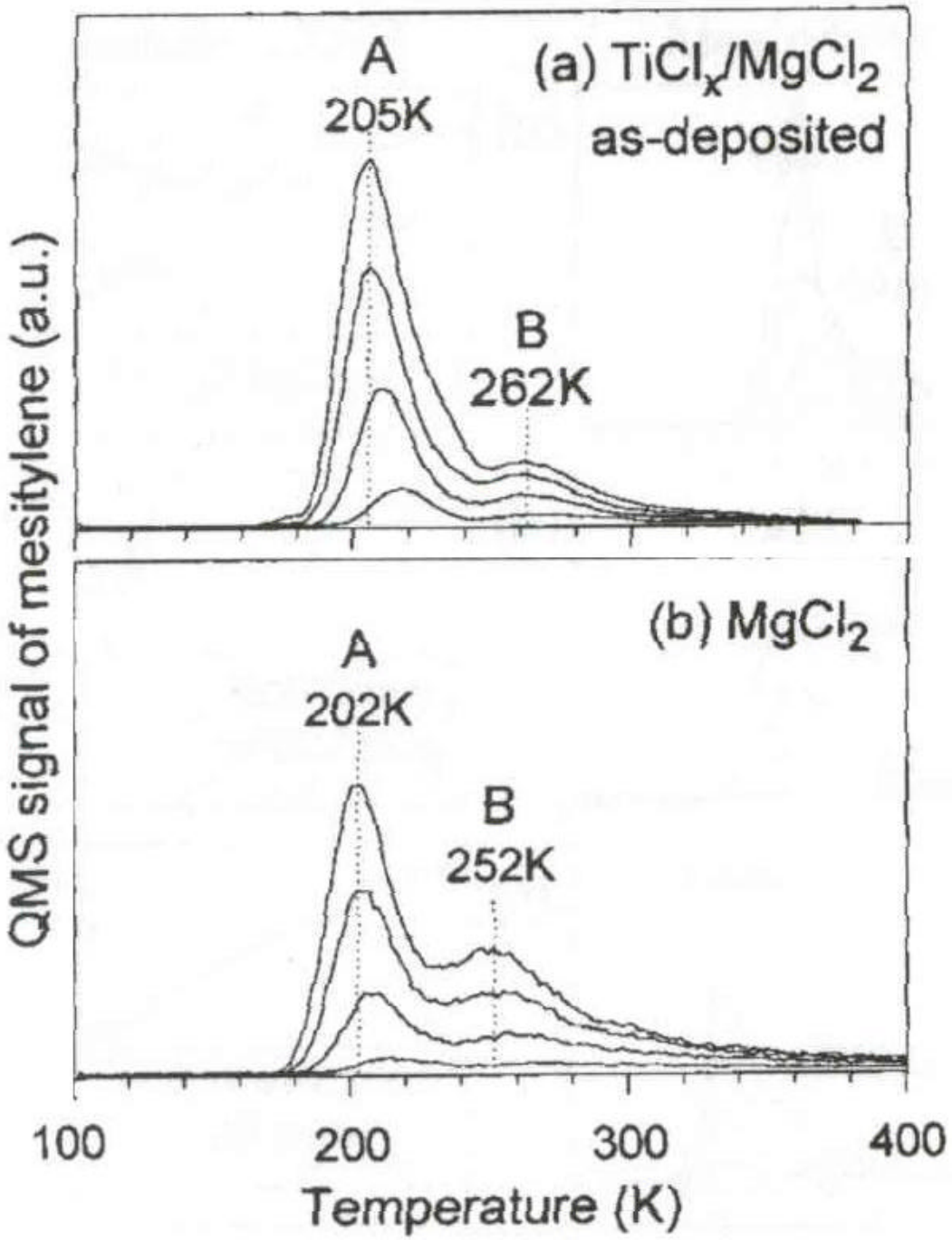

Figure 3.1 Mesitylene TPD for (a) the $TiCl_x$ / $MgCl_2$ film and (b) the $MgCl_2$ reference film. Mesitylene exposure: 0.2, 0.6, 1.0, and 1.4 L (from the bottom). The saturation of mesitylene 1 ML occurs at an exposure of ~4.5 L. Film deposition conditions: T_{Mg} = 600 K; $P(TiCl_4) = 1 \times 10^{-7}$ Torr; time = 10 min.

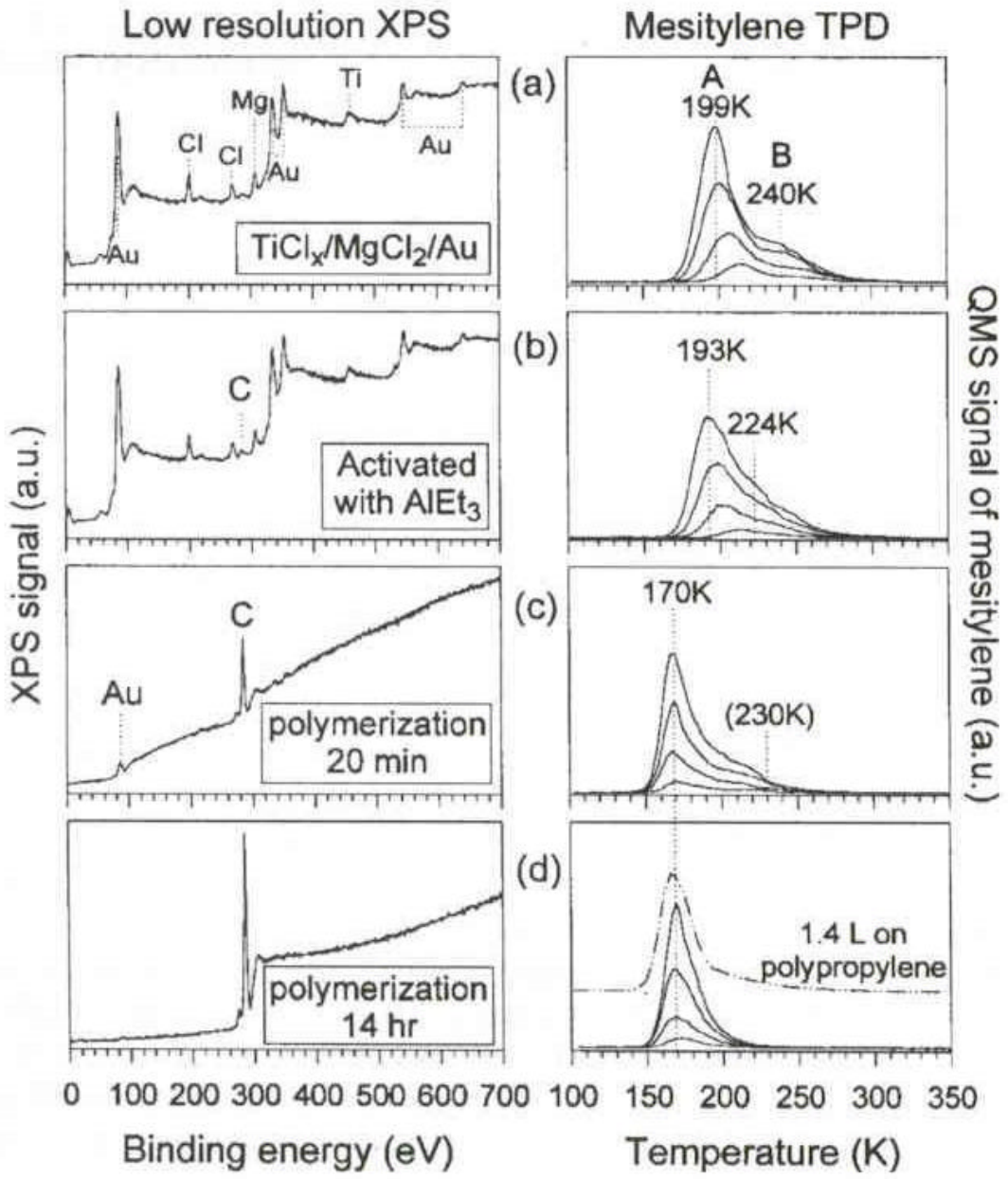

Figure 3.2 XPS and mesitylene TPD for the model Ziegler-Natta catalyst: (a) as-deposited $TiCl_x$ / $MgCl_2$ film; (b) after catalyst activation (exposure to 1 Torr of $AlEt_3$ for 3 min at T_{sample} = 300 K); (c) after 20 min of polymerization (800 Torr of propylene at T_{sample} = 343 K); and (d) after 14 h of polymerization (800 Torr of propylene at T_{sample} = 343 K). Film deposition conditions: T_{Mg} = 610 K; $P(TiCl_4) = 2 \times 10^{-7}$ Torr; time = 10 min. Mesitylene exposure: 0.2, 0.6, 1.0, and 1.4 L (from the bottom).

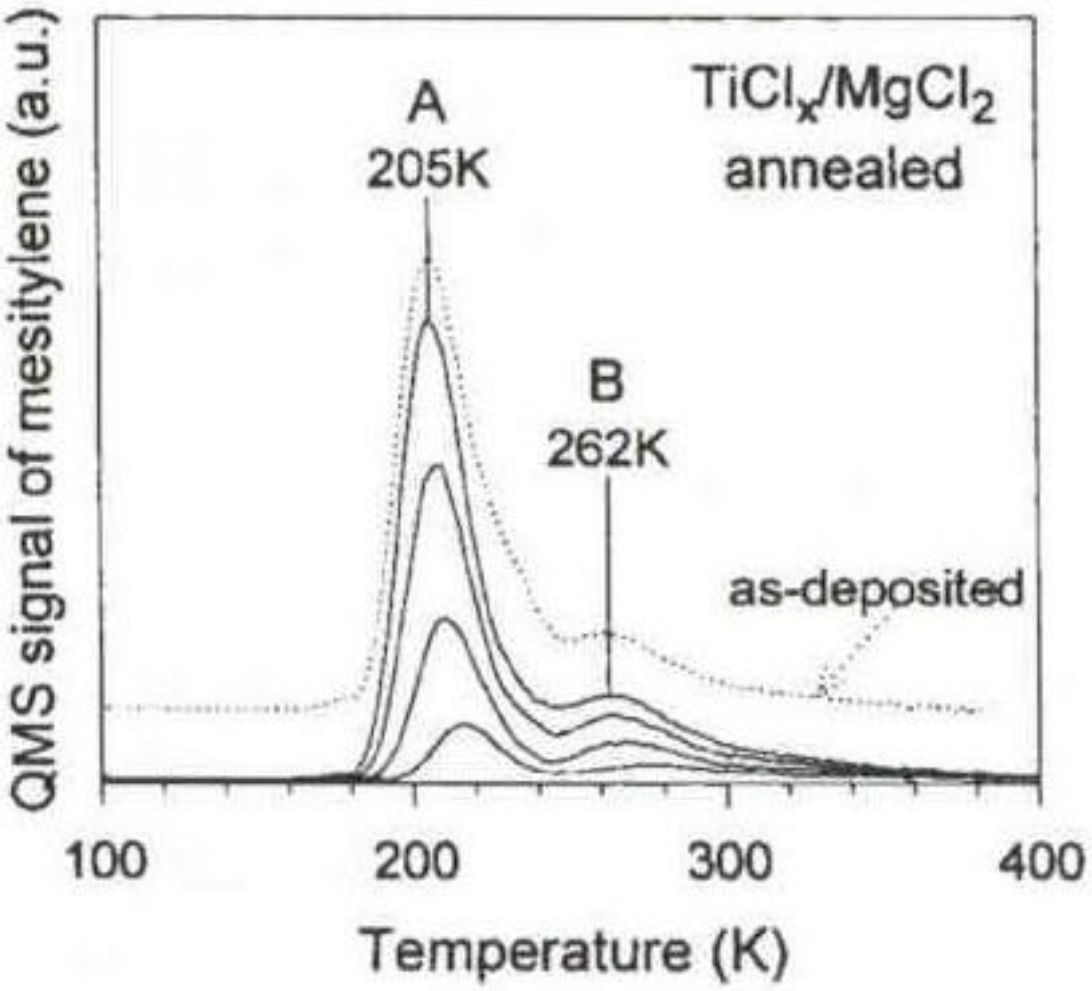

Figure 3.3 Mesitylene TPD after annealing the $TiCl_x$ / $MgCl_2$ film (used in Figure 5.1a) at 640 K. Mesitylene exposure (solid lines): 0.2, 0.6, 1.0, and 1.4 L (from the bottom). For comparison, the TPD profile of 1.4 L mesitylene in Figure 1a is shown as the dotted line.

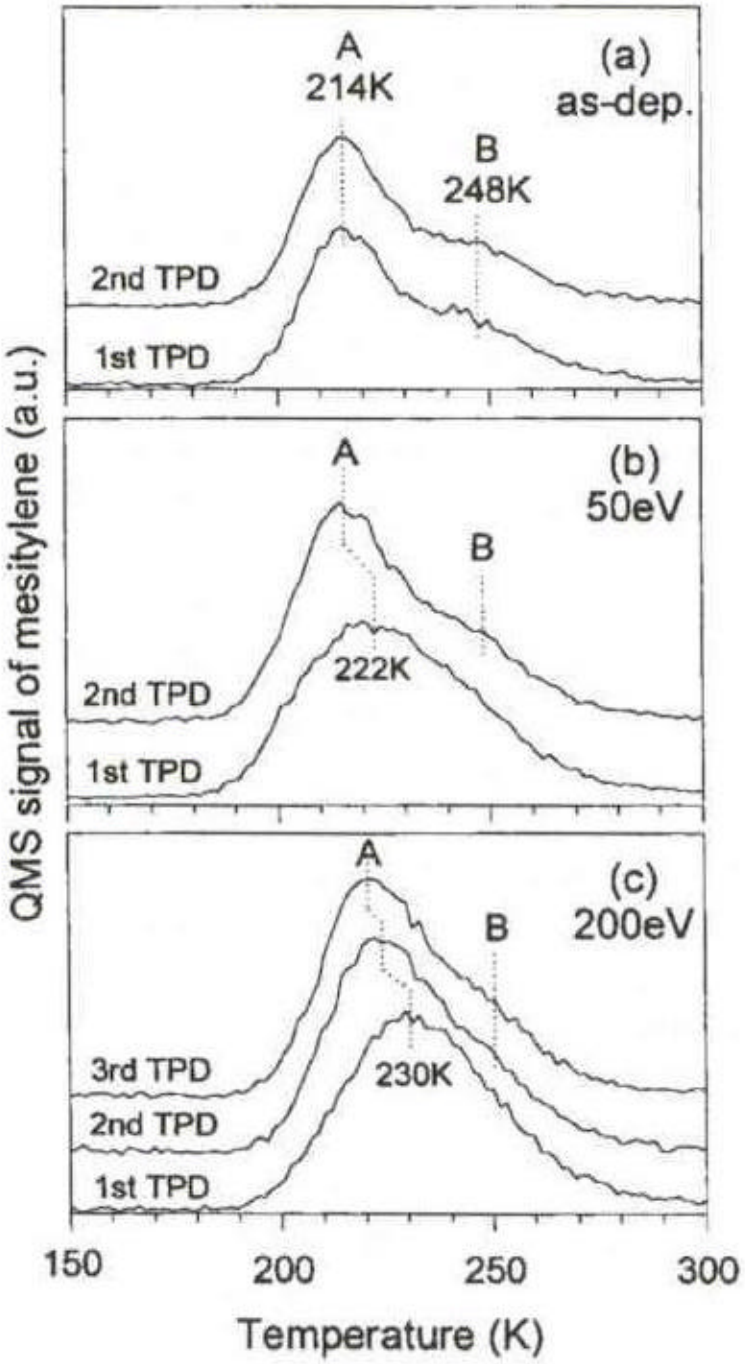

Figure 3.4 Effect of postdeposition electron irradiation on 0.2 L mesitylene TPD for the $TiCl_x$ / $MgCl_2$ film: (a) as-deposited film; (b) 50 eV electron irradiation; and (c) 200 eV electron irradiation (electron dose = 6×10^{16} electrons / cm^2). Film deposition conditions: T_{Mg} = 630 K; $P(TiCl_4) = 2 \times 10^{-7}$ Torr; time = 15 min.

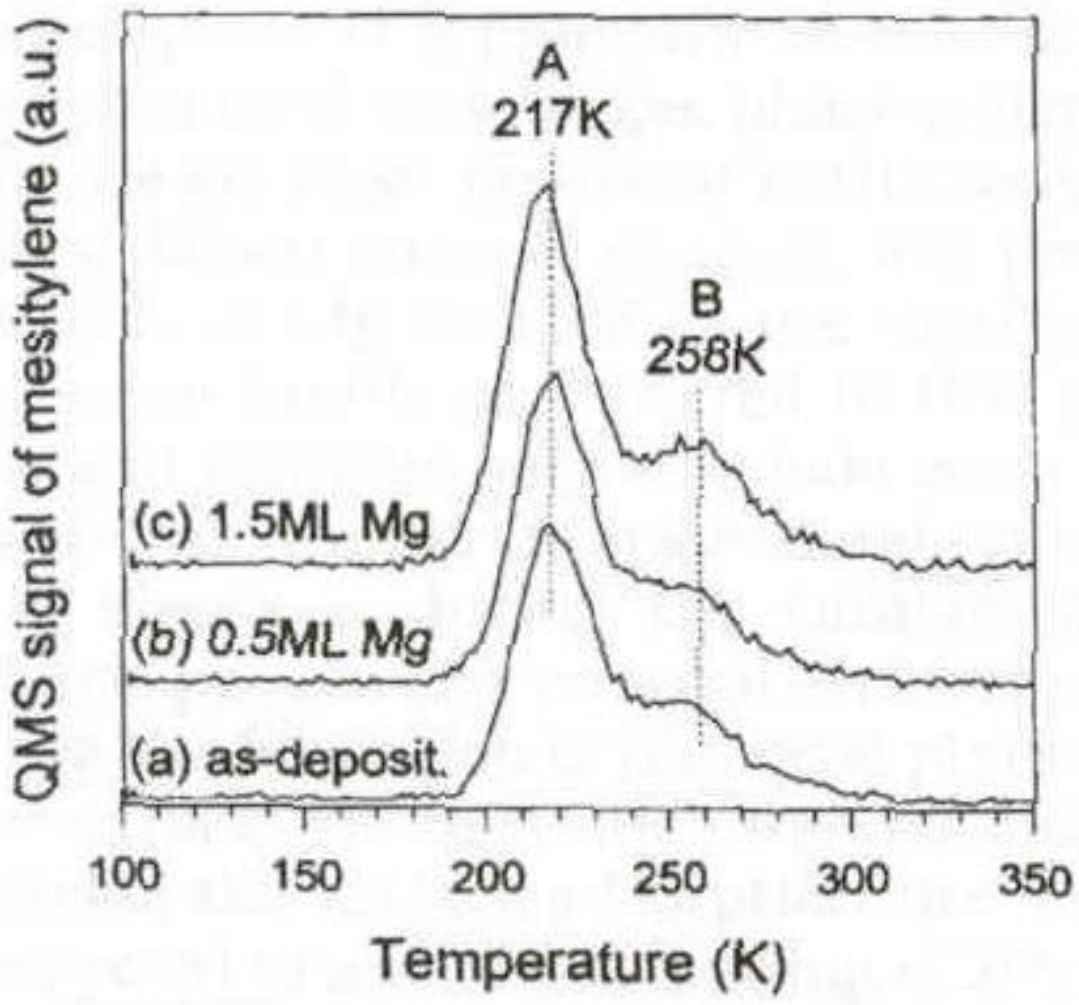

Figure 3.5 Mesitylene TPD (0.2 L) for the $TiCl_x$ / $MgCl_2$ film (a) before and after Mg doses of (b) 0.5 ML and (c) 1.5 ML. Film deposition conditions: T_{Mg} = 630K; $P(TiCl_4) = 2 \times 10^{-7}$ Torr; time = 15 min.

Chapter 4

Characterization and *in situ* Monitoring of Model and Industrial Ziegler-Natta Catalytic Support Materials Using Ultraviolet-Raman Spectroscopy

Section 4.1 Introduction

High-yield Ziegler-Natta polymerization catalysts are based on a $TiCl_4$ catalyst with an Al-trialkyl co-catalyst supported on chemically activated $MgCl_2$. The nature of the active site for this highly-active and stereospecific polypropylene catalyst has been the subject of Chapter 3 and numerous other studies.[1-18] The molecular-level information gained from these ex-situ studies has led to the recent report of a correlation between different surface adsorption sites and the degree of stereospecificity in propylene polymerization.[19] The ability to probe the structure of a Ziegler-Natta catalyst in-situ can provide a significant opportunity to extend the success of these ex-situ studies.

Toward this end, this chapter discusses the first step in developing a technique to probe the structure of Ziegler-Natta catalysts in situ. UV-Raman spectroscopy has been applied to the study of Mg-ethoxide Ziegler-Natta supports prepared from $MgCl_2$ and ethanol. Characterization of these supports is important because it is known that chemically activating $MgCl_2$ with an electron donor such as ethanol, markedly affects both catalyst performance and polymer properties.[20-24]

In this chapter UV-Raman spectroscopic studies of $MgCl_2(C_2H_5OH)_x$ adducts prepared over a wide composition range, x = 0.47 to 6, are reported. Structures were determined for the x = 2 and x = 6 adducts by XRD.[25,26] The results reported in this dissertation confirm the dissociation of the Mg-Cl octahedra at $x \geq 2$. The Raman frequency of the O-H stretch shifts as the C_2H_5OH to $MgCl_2$ molar ratio is altered. A unique correlation between the Raman O-H peak frequency and the $MgCl_2(C_2H_5OH)_x$ composition is reported. This correlation is used as an in situ tool to monitor the dealcoholation of an industrial Mg-ethoxide support sample. The origin of a vibrational spectroscopic feature unique to the x = 6 adduct is discussed.

Section 4.2 Experimental

A series of $MgCl_2(C_2H_5OH)_x$ adducts with $0 < x \leq 6$ were synthesized at Basell "G. Natta" Research Center in Ferrara, Italy. The samples were synthesized by addition of pure ethanol (Ethanol 99.8% purchased from Carlo Erba) to crystalline α-$MgCl_2$ (purchased from Cezus and sieved to select crystals between 700 and 1000 ? m, XRD pattern in Figure 4.1) in precise different stoichiometric amounts which resulted in a swollen white material. The material, independent of composition, was heated to 180 ^{0}C at a rate of 5 ^{0}C/min, followed by a slow cooling to room temperature at a rate of 0.5 ^{0}C/min. After the thermal treatment the samples were reduced to powder by manual milling for 5 minutes into an agate mill in order to obtain a fine powder suitable to be loaded into fused silica capillaries. This entire procedure was performed in an inert, dry atmosphere. The error in determining the molar composition of the synthesized systems is estimated to be within ± 3% based on thermogravimetric analysis.[27] The samples

were determined to be crystalline by differential scanning calorimetry.[27] The XRD pattern for the sample with x = 6 is compared to a reference spectrum in Figure 4.2.

The X-ray Powder Diffraction (XRD) spectra of the synthesized samples were obtained with a Phylips Powder Diffractometer PW 1710. The Cu-K$_{\alpha 1}$ radiation (λ= 0.154 nm) was employed and an instrumental 2θ step of 0.1° every 6 seconds from 5° to 60° was selected. During the XRD measurement the samples were maintained in a N_2 atmosphere in a well sealed polyethylene bag that was kept out of the focal plane. The absolute diffraction line positions were determined relative to the diffraction lines of silicon powder that was added to the sample as internal position line reference.

Figure 4.3 is an overview of the UV-Raman spectroscopy experimental setup. The excitation source is the 244 nm output of a Lexel SHG, an intracavity doubled, continuous wave Ar^+ laser. The 244 nm beam is focused at 45° to the sample normal by a 2 cm focal length spherical lens. The Raman scattered light is collected by a 50 mm diameter f/2 fused silica lens; this corresponds to a solid angle of collection of 0.20 sr. The collected scattered light is focused on the entrance slit of a f/3.7 Triplemate triple spectrometer by a 160 mm focal length lens. The filter stage of the Triplemate contains two 2400 gr/mm diffraction gratings for efficient rejection of stray reflections and the intense Rayleigh scattered light. A 2400 gr/mm diffraction grating is used in the dispersion stage. The spectrum is collected on a back thinned, UV-enhanced liquid-nitrogen-cooled 1340 x 100 pixel CCD detector. The quantum efficiency of the CCD array at 244 nm is approximately 33%. The spectral resolution is ~24 cm^{-1}.

Spectra obtained between 0 and 1500 cm^{-1} were calibrated using the well-known Raman shifts of cyclohexane.[28] Spectra obtained between 3200 and 3620 cm^{-1} were

calibrated using the O-H peak frequencies of gibbsite.[29] This calibration was extrapolated for use in a region spanning from 2800 to 3700 cm^{-1}.

The spectrometer response function was assumed to be constant and no attempt was made to correct the spectra. The absolute signal intensity did vary between samples due to slight differences in the focus of the incident laser on the fused silica capillary tubes. To facilitate comparison of peak intensities between spectra, one peak in a given spectral region for each sample was chosen as an internal intensity standard. The $\nu(CCO)_s$ peak of ethanol at ~885 cm^{-1} was used for the spectra between 0 and 1500 cm^{-1}. The $\nu(CH_2)_{as}$ peak of ethanol at ~2938 cm^{-1} was used for the spectra between 2800 and 3700 cm^{-1}.

Sample integrity under the UV laser beam was investigated. Without thermal or photochemical damage induced by the laser beam, the Raman intensity would increase proportionally with the incident laser power. Raman spectra of the adducts were obtained at 2, 4, 8, 12, and 16 mW. Signal intensity increased linearly with laser power between 2 and 12 mW and all spectra reported here were obtained within this power range. Another indication of sample integrity is the absence of any peak ~1630 cm^{-1} that is indicative of laser induced coke formation from the ethanol.[30,31]

Section 4.3 Results and Discussion

Section 4.3.1 Characterization of Model Mg-ethoxide Ziegler-Natta Support Materials

Crystalline $MgCl_2$ belongs to the rhombohedral space group, D_{3d}, and has a layered structure. The magnesium atoms are in a distorted octahedral configuration coordinated to six chlorine atoms. The octahedra are joined through

chlorine bridges. The Raman mode at 242 cm^{-1} has been assigned to the A_{1g} breathing of the octahedra in the lattice.[32]

Figure 4.4 shows the Raman spectra of powdered $MgCl_2$, a series of $MgCl_2(C_2H_5OH)_x$ adducts, and liquid ethanol from 100 to 1600 cm^{-1}. Features below 200 cm^{-1} in the $MgCl_2(C_2H_5OH)_x$ adduct spectra are due to the fused silica capillary tubes. The A_{1g} mode of $MgCl_2$ at 240 cm^{-1} is observed for the x = 1.67 adduct which indicates the octahedral arrangement of chlorine atoms is maintained at this stoichiometry. This mode is no longer present for the x = 2.05 adduct, indicating a loss of the D_{3d} symmetry of $MgCl_2$. This result is consistent with the $MgCl_2(C_2H_5OH)_2$ structure proposed by Di Noto et al. based on their x-ray diffraction results on powdered polycrystalline samples.[25] They reported a structure where ethanol has disrupted the D_{3d} symmetry of solid $MgCl_2$ through displacement of two chlorine atoms by oxygen atoms of two ethanol molecules. The Mg atoms are connected through two chlorine bridges creating a chain of repeating $MgCl_2(C_2H_5OH)_2$ units.

For $x \geq 3.35$, a peak at 683 cm^{-1} is observed which is not found in liquid ethanol. As shown in Figure 4.5, the intensity of this mode relative to the ethanol $\nu(CCO)_s$ peak at ~875 cm^{-1} increases with the ethanol loading and is most intense for x = 6. The structure of $MgCl_2(C_2H_5OH)_6$ has been solved by G. Valle et al.[26] The structure consists of Mg atoms octahedrally coordinated to six ethanol oxygens. The normal modes for the octahedral point group, O_h, are shown in Figure 4.6. The Raman active modes are A_{1g}, E_g, and T_{2g}. Previous IR studies show no peak around 683 cm^{-1}.[25] This peak is most likely due to the A_{1g} mode (Figure 4.7) since it contains inversion symmetry and would not be simultaneously IR active. A review of the literature shows

a range of frequencies for Mg-O stretches that supports this assignment. Magnesium oxide and magnesium hydroxide Mg-O stretches are found at 785 and 750 cm^{-1}, respectively.[33,34] An ab initio calculation for a $Mg^{2+}O_2^-$ superperoxide complex predicts a Mg-O stretch at 679 cm^{-1}.[35] In their HREELS study of the interaction of magnesium with tris(8-hydroxy-quinoline) aluminum, P. He et al. proposed that their observed peak at 653 cm^{-1} was due to a Mg-O stretch.[36] The closest analogue to the x = 6 adduct that is commercially available is $Mg(OC_2H_5)_2$. A UV-Raman spectrum of this compound is shown in Figure 4.8 along with a spectrum for C_2H_5OH and $MgCl_2(C_2H_5OH)_6$. There is a small peak at ~600 cm^{-1} in the $Mg(OC_2H_5)_2$ spectrum that could be due to a Mg-O stretch. Given the difference in the coordination and symmetry around Mg^{2+}, the frequency shift and intensity decrease is not unreasonable. The validity of this assignment could be improved by determining the depolarization ratio of the peak for a single crystal. Assuming the spectral assignment to be correct, the increase in relative intensity of this new peak indicates that the octahedral arrangement of the six ethanol molecules begins to form below the stoichiometric value of x = 6.

In Figure 4.9, the spectra of liquid ethanol and the $MgCl_2(C_2H_5OH)_x$ adducts in the C-H and O-H stretching region are shown. The peaks in the 3230-3480 cm^{-1} range are due to the O-H stretch of ethanol. The frequency of the O-H stretch is effected strongly by the molar ratio of ethanol to $MgCl_2$ whereas the C-H stretches are not. The O-H stretch for the x = 0.47 adduct is well defined and centered at 3480 cm^{-1}. For x > 1, the O-H stretch broadens and shifts to frequencies at or below the observed peak for liquid ethanol where strong hydrogen bonding is known to occur.[37-39] In the gas phase, the O-H stretch of ethanol is not effected by hydrogen bonding and two peaks are

observed at 3660 and 3677 cm^{-1} which can be assigned to the gauche and trans isomers, respectively.[40,41] The O-H Raman shifts for adducts with $x < 1$ fall between those of liquid and gas phase ethanol and indicate the O-H groups are involved in weak hydrogen bonds. For $x > 1$, the observed O-H Raman shift falls below that of liquid ethanol and therefore hydrogen bonding between ethanol molecules does not account for the observed shift. The O-H stretch for the $MgCl_2(C_2H_5OH)_6$ adduct is observed at 3233 cm^{-1}. The structure proposed for this adduct indicates that the hydrogen of each alcohol group forms a hydrogen bond with a chlorine atom and each chlorine atom contributes to the formation of three hydrogen bonds.[26] Low temperature Raman studies of concentrated ethanol-LiCl solid solutions have shown O-H Raman shifts as low as 3285 cm^{-1}, lower than that of liquid ethanol.[42] Therefore, hydrogen bonding with a chloride ion is a plausible explanation for the observed peak shift and is consistent with the structure analysis of the $MgCl_2(C_2H_5OH)_6$ adduct.

In Figure 4.10 the O-H stretch peak frequency is plotted as a function of the ethanol to $MgCl_2$ ratio, x. As mentioned previously, the Mg atoms are connected through two chlorine bridges creating a chain of repeating $MgCl_2(C_2H_5OH)_2$ units for the $x = 2$ adduct. Below the stoichiometric value of $x = 2$, the O-H stretching frequency is greater than that of the $x = 2$ adduct which indicates a similar structure, but with fewer neighboring $MgCl_2(C_2H_5OH)_2$ units.

As x increases beyond 2, the chlorine bridges are broken as more ethanol is incorporated into the Mg^{2+} coordination sphere. The ethanol hydroxy groups become involved in more hydrogen bonds with the resultant chlorine anions as observed in the continuous decrease in the O-H frequency.

Section 4.3.2 In situ Monitoring of an Industrial Mg-ethoxide Ziegler-Natta Support Material During Delalcoholation As mentioned in the introduction of this chapter, the chemical activation of $MgCl_2$ with ethanol to form the Mg-ethoxide supports markedly affect both the catalyst performance and polymer properties. These effects can be tailored by carefully controlling the dealcoholation of the Mg-ethoxide support.

In the previous section, UV-Raman spectra were acquired during long acquisitions at low laser power with the adduct stationary relative to the laser beam. To follow spectral changes with time during a dealcoholation, it was necessary to increase the laser power to shorten acquisition time. To ensure that the incident UV laser was not responsible for any observed spectral changes, data were obtained in both the fluidized and pack bed UV-Raman reactors at room temperature for an industrial Ziegler-Natta support sample. The spectra acquired in the packed bed UV-Raman reactor are shown in Figure 4.8. After the first 3 minute acquisition, the O-H peak had already broadened. A subsequent 5 minute acquisition indicated a significant loss of ethanol from the focal volume of the laser. In Figure 4.9, the first and second 10 minute acquisition in the fluidized bed UV-Raman reactor were identical. The O-H peak did not broaden.

The spectra for the dealcoholation were acquired in the fluidized bed UV-Raman reactor. An industrial Ziegler-Natta support with 42 wt% ethanol was heated at 50^oC in a stream of helium. A Raman spectrum from 2400 to 3700 cm^{-1} was acquired every 10 minutes. The spectra were analyzed to determine the frequency of the O-H peaks and the intensity of those peaks relative to the $\nu(CH)_{as}$ peak at 2938 cm^{-1}. The

results of that analysis are shown in Figures 4.13a and 4.14a where the Raman Shift and the relative intensities are plotted as a function of time. The correlation of O-H peak frequency with ethanol content, x, developed in the previous section was used to create Figures 4.13b and 4.14b.

After 10 minutes of heating at 50°C, two O-H peaks are observed that correspond to x = 3.5 and 1.0. As the dealcoholation continued, the x = 1.0 peak shifted to higher frequency corresponding to a structure with less ethanol per Mg center. The relative intensity of this peak increased with time. The shift of the x = 3.5 peak was small, but scattered. The relative intensity of this peak, however, decreased and eventually vanished with time. Thus, the most strongly bound ethanol was found in an x = 0.5 structure.

Section 4.4 Conclusions

UV-Raman spectroscopy has been successfully applied to study the interactions between $MgCl_2$ and C_2H_5OH that produce support precursors for Ziegler-Natta polymerization catalysts. For $MgCl_2(C_2H_5OH)_x$ adducts with $x \geq 2$, the 242 cm^{-1} peak of $MgCl_2$ disappears, indicating the destruction of the D_{3d} symmetry of $MgCl_2$. For $x \geq 3.35$, a new peak at 683 cm^{-1} begins to appear. The intensity of the peak increases with the amount of ethanol in the adduct. This peak is attributed to the totally symmetric breathing of Mg-O octahedra characteristic of the $MgCl_2(C_2H_5OH)_6$ structure. Its presence below x = 6 suggests the Mg-O octahedral structure may be thermodynamically favored over structures with a random number distribution of ethanol molecules. In addition, the position of the O-H stretch shifts from 3480 to 3230

cm^{-1} as x increases from 0 to 6 relative to $MgCl_2$. The correlation between O-H peak shift and the C_2H_5OH to $MgCl_2$ molar ratio, x, can be utilized as an in situ monitoring tool. The in situ monitoring of the dealcoholation of an industrial Mg-ethoxide support material indicated that the most strongly bound ethanol was found in the x = 0.5 structure. The tailoring of the catalyst performance with different dealcoholation conditions could be due to creating a support with different ratios of strongly and weakly bound ethanol before uptake of $TiCl_4$.

Section 4.5 References

(1) Barbe, P. C.; Cecchin, G.; Noristi, L. *Adv. Polym. Sci.* **1987**, *81*, 1.

(2) Dusseault, J. J. A.; Hsu, C. C. *J. M. S.- Rev. Macromol. Chem. Phys.* **1993**, *C33*, 103.

(3) Cossee, P. J. *Journal of Catalysis* **1964**, *3*, 80.

(4) Arlman, E. J. *Journal of Catalysis* **1964**, *3*, 89.

(5) Arlman, E. J.; Cossee, P. J. *Journal of Catalysis* **1964**, *3*, 99.

(6) Fujimoto, H.; Koga, N.; Hataue, J. *J. Phys. Chem.* **1984**, *88*, 3539.

(7) Guerra, G.; Pucciariello, R.; Villani, V.; Corradini, P. *Polym. Commun.* **1987**, *28*, 100.

(8) Venditto, V.; Guerra, G.; Corradini, P. *European Polymer Journal* **1991**, *27*, 45.

(9) Cavallo, L.; Guerra, G.; Corradini, P. *J. Am. Chem. Soc.* **1998**, *120*, 2428.

(10) Lin, J. S.; Catlow, C. R. A. *J. Mater. Chem.* **1993**, *3*, 1217.

(11) Colbourn, E. A.; Cox, P. A.; Carruthers, B.; Jones, P. J. V. *J. Mater. Chem.* **1994**, *4*, 805.

(12) Shiga, A.; Kawamura-Kuribayashi, H.; Sasaki, T. *J. Mol. Catal.* **1994**, *87*, 243.

(13) Shiga, A.; Kawamura-Kuribayashi, H.; Sasaki, T. *J. Mol. Catal.* **1995**, *98*, 15.

(14) Puhakka, E.; Pakkanen, T. T.; Pakkanen, T. A. *Surf. Sci.* **1995**, *334*, 289.

(15) Puhakka, E.; Pakkanen, T. T.; Pakkanen, T. A. *J. Mol. Catal. A* **1997**, *120*, 143.

(16) Boero, M.; Parrinello, M.; Terakura, K. *J. Am. Chem. Soc.* **1998**, *120*, 2746.

(17) Boero, M.; Parrinello, M.; Terakura, K. *Surf. Sci.* **1999**, *438*, 1.

(18) Boero, M.; Parrinello, M.; Huffer, S.; Terakura, K. *J. Am. Chem. Soc.* **2000**, *122*, 501.

(19) Kim, S. H.; Somorjai, G. A. *J. Phys. Chem. B* **2001**, *105*, 3922.

(20) Boor, J., Jr. *Ziegler-Natta Catalysis and Polymerizations*; Academic Press: New York, 1979.

(21) van der Ven, S. *Polypropylene and Other Polyolefins: Polymerization and Characterization*; Elsevier: Amsterdam, 1990.

(22) Albizzati, E.; Giannini, U.; Collina, G.; Noristi, L.; Resconi, L. In *Polypropylene Handbook*; Moore, E. P., Jr., Ed.; Carl Hanser Verlag: Munich, 1996.

(23) Kissin, Y. V. *Isospecific Polymerization of Olefins with Heterogeneous Ziegler-Natta Catalysts*; Springer: New York, 1985.

(24) *Encyclopedia of Polymer Science and Engineering*; Wiley: New York, 1988; Vol. 13.

(25) Di Noto, V.; Zannetti, R.; Viviani, M.; Marega, C.; Marigo, A.; Bresadola, S. *Makromol. Chem* **1992**, *193*, 1653.

(26) Valle, G.; Baruzzi, G.; Paganetto, G.; Depaoli, G.; Zannetti, R.; Marigo, A. *Inorg. Chim. Acta* **1989**, *156*, 157.

(27) unpublished results, Basell "G. Natta" Research Center.

(28) McCreery, R. L. *Raman Spectroscopy for Chemical Analysis*; Wiley-Interscience: New York, 2000; Vol. 157.

(29) Dollish, F. R.; Fateley, W. G.; Bentley, F. *Characteristic Raman Frequencies of Organic Compounds*; John Wiley & Sons, Inc.: New York, 1974.

(30) Chua, Y. T.; Stair, P. C. *J. of Catal.* **2000**, *196*, 66.

(31) Gilkes, K. W. R.; Prawer, S.; Nugent, K. W.; Robertson, J.; Sands, H. S.; Lifshitz, Y.; Shi, X. *J. Applied Physics* **2000**, *87*, 7283.

(32) Balasubrahmanyam, K. *J. Chem. Phys.* **1966**, *44*, 3270.

(33) *Spectra of Diatomic Molecules*; Van Nostrand Reinhold: New York, 1950.

(34) Bunker, P. R.; Kolbuszewski, M.; Jensen, P.; Brumm, M.; Anderson, M. A.; Barclay, W. L.; Ziurys, L. M.; Ni, Y.; Harris, D. O. *Chemical Physics Letters* **1995**, *239*, 217.

(35) Chen, J.; Wong, T. H.; Kleiber, P. D. *Journal of Chemical Physics* **1998**, *109*, 8311.

(36) He, P.; Au, F. C. K.; Wang, Y. M.; Cheng, L. F.; Lee, C. S.; Lee, S. T. *Applied Physics Letters* **2000**, *76*, 1422.

(37) Urban, M. W. *Vibrational Spectroscopy of Molecules and Macromolecules on Surfaces*; J. Wiley & Sons: New York, 1993.

(38) van der Maas, J. H.; Lutz, E. T. G. *Spectrochimica Acta* **1974**, *30*, 2005.

(39) Lutz, E. T. G.; van der Maas, J. H. *Spectrochimica Acta* **1978**, *34*, 915.

(40) Schiel, D.; Richter, W. *Chem. Phys. Letters* **1990**, *166*, 82.

(41) Schiel, D.; Richter, W. *J. Chem. Phys.* **1983**, *78*, 6559.

(42) Ishioka, K.; Hase, H. *J. Phys.: Condens. Matter* **1993**, *5*, 2461.

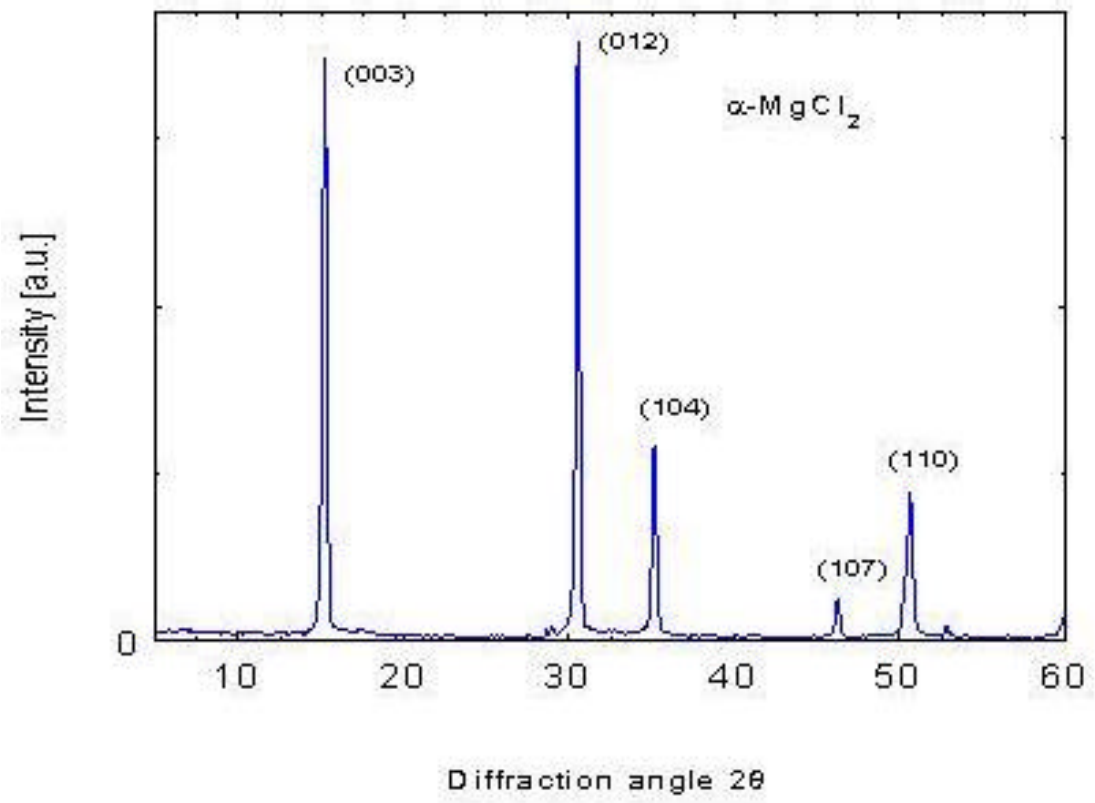

Figure 4.1 XRD pattern of α-$MgCl_2$.

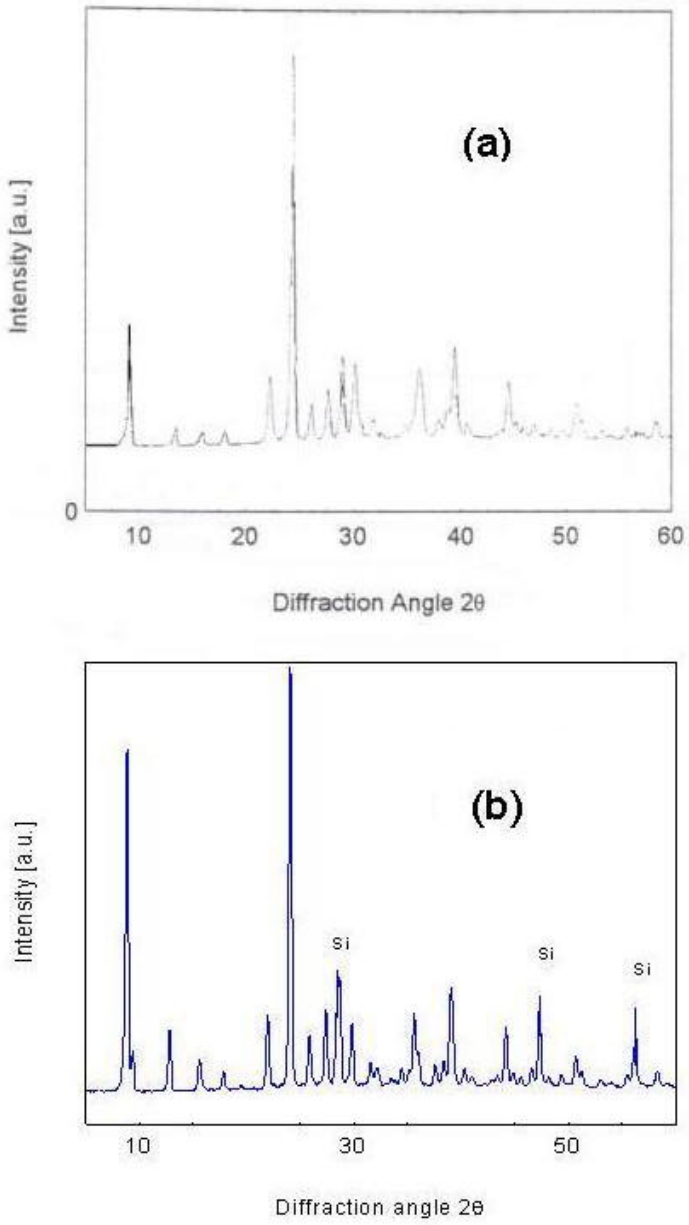

Figure 4.2 XRD of $MgCl_2(C_2H_5OH)_6$ **(a)** as synthesized and **(b)** reference spectrum from G.Valle et al. *Inorganica Chimica Acta* **156** (1989) p. 157.

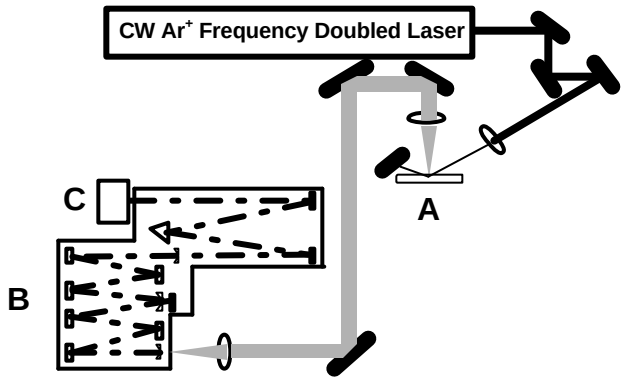

Figure 4.3 Experimental UV-Raman setup. The 244 nm laser beam is focused on a fused silica capillary tube at ~45^{o} by a 2 cm focal length spherical lense (**A**). The light scattered normal to the sample is collected and focused on the entrance slit of the Triplemate Spectrometer (**B**). The filtered and dispersed light is collected with a back-thinned, UV-enhanced CCD detector cooled by a liquid nitrogen resevoir (**C**).

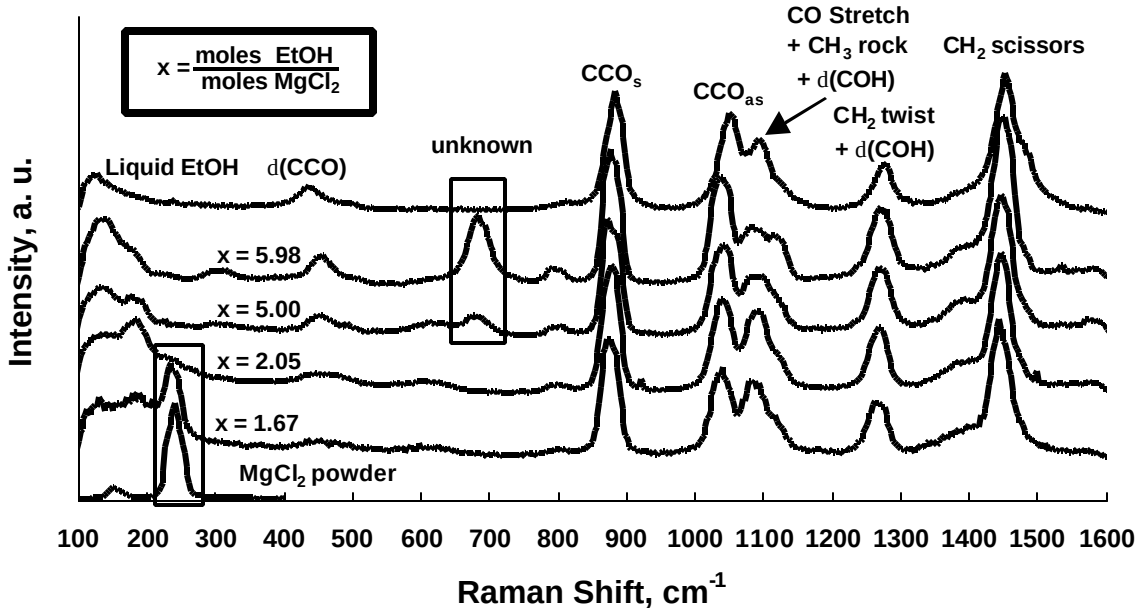

Figure 4.4 UV-Raman spectra of powdered $MgCl_2$, $MgCl_2(C_2H_5OH)_x$ adducts, and liquid ethanol. The liquid ethanol peaks assignments are shown.[29] The $MgCl_2$ peak at 242 cm^{-1} is due to a symmetric breathing mode of Mg-Cl octahedra. The intensity of the $\nu(CCO)_s$ peak at ~885 cm^{-1} has been used as an internal intensity standard.

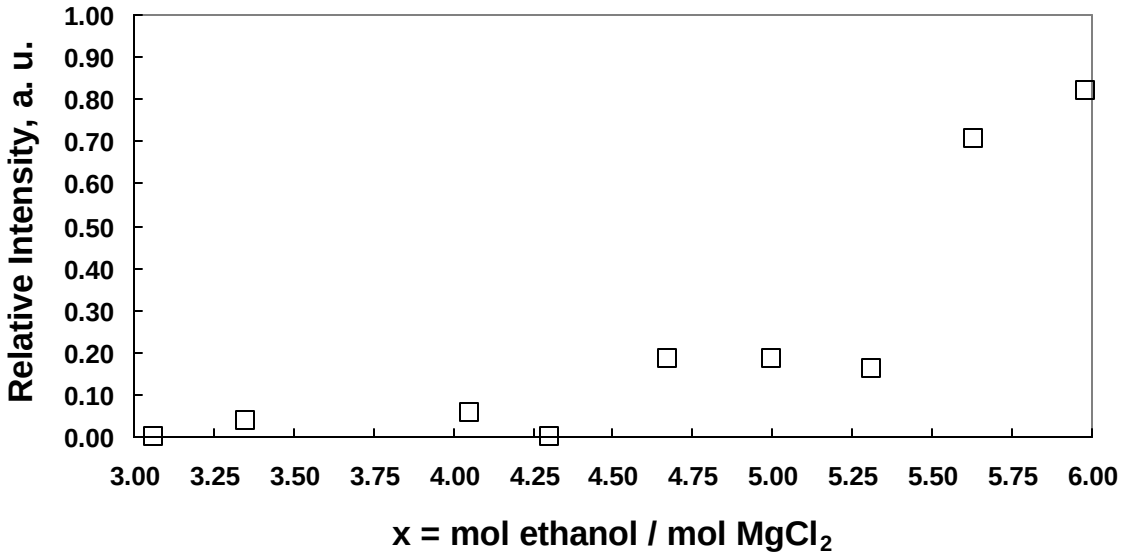

Figure 4.5 Intensity of Mg-O octahedral stretch at 683 cm^{-1} relative to the $\nu(CCO)_s$ peak at 885 cm^{-1} for the $MgCl_2(C_2H_5OH)_x$ adducts shown as a function of ethanol to $MgCl_2$ molar ratio, x.

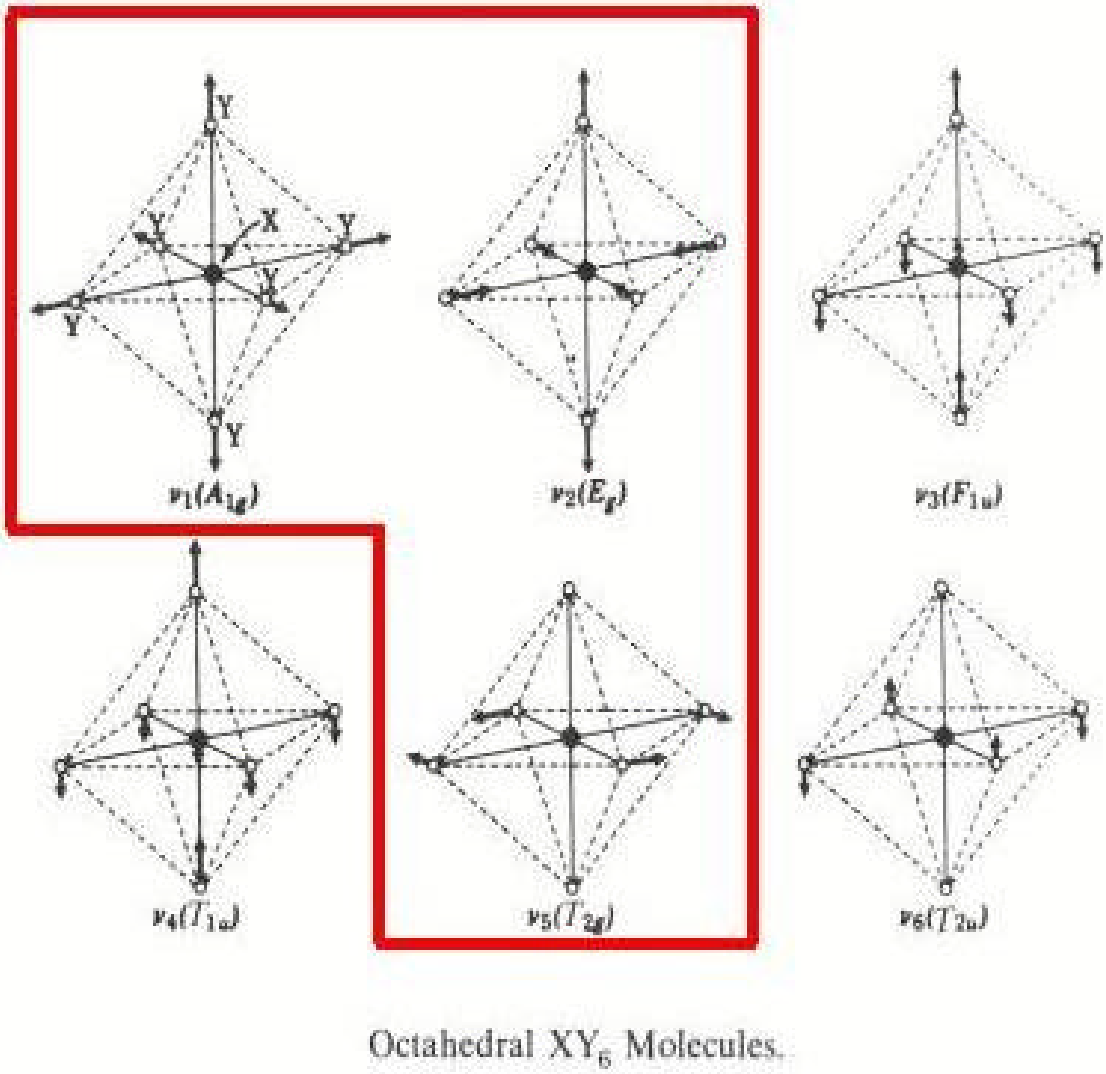

Figure 4.6 Normal modes of octahedral molecules.

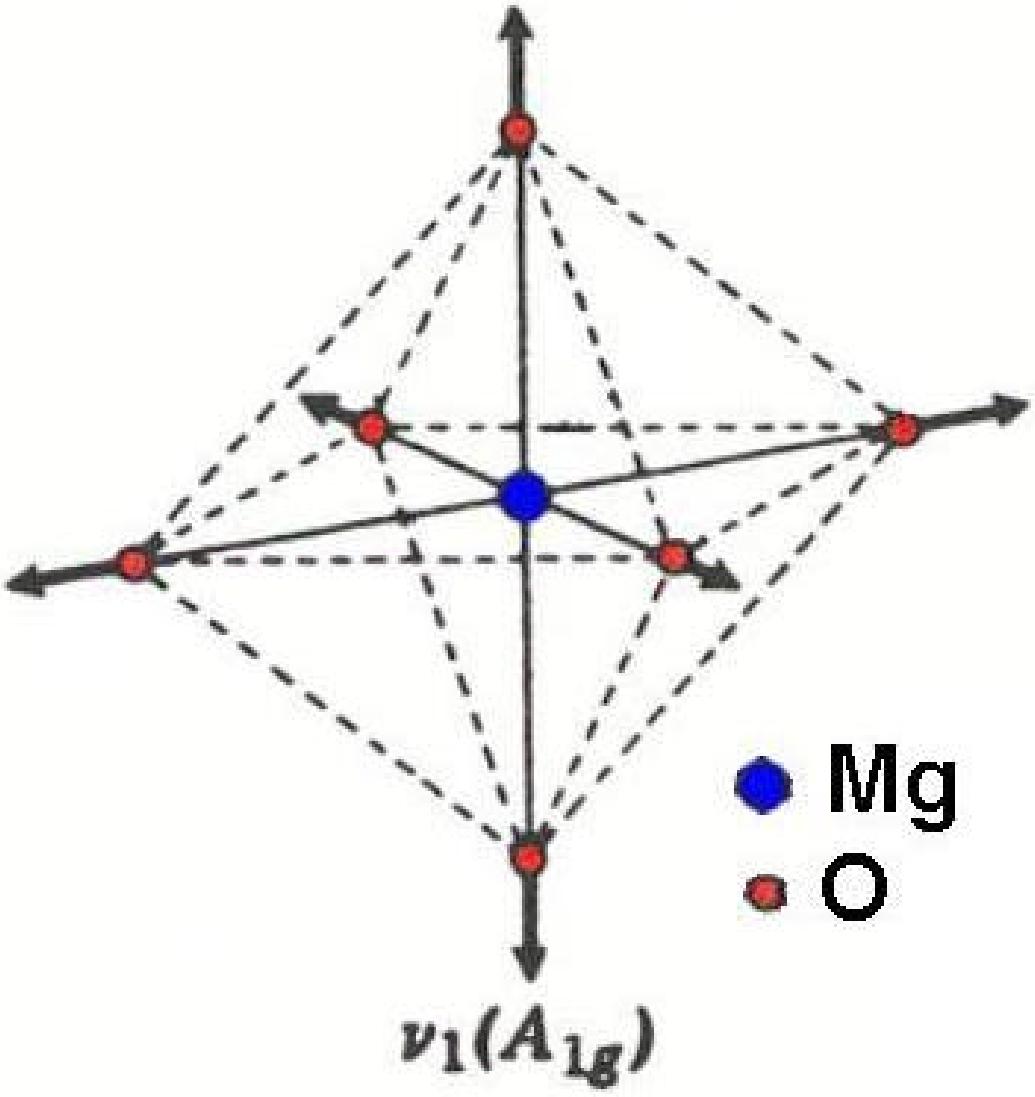

Figure 4.7 Totally symmetric "breathing mode" (A_{1g}) of an octahedral molecule (O_h point group).

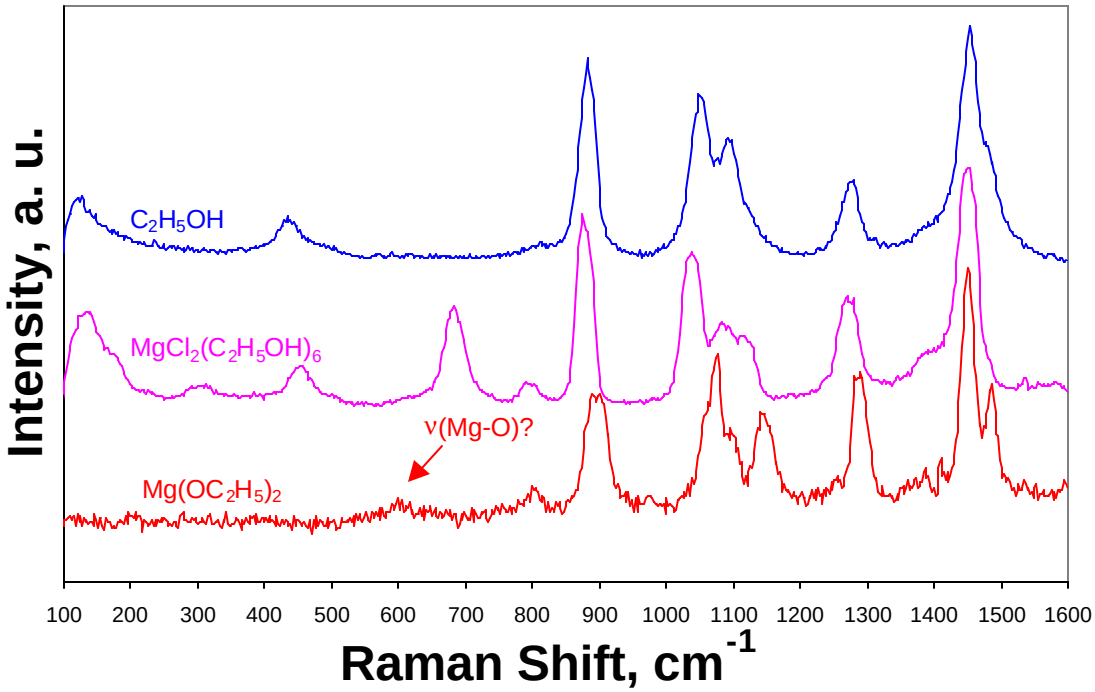

Figure 4.8 Identification of 683 cm^{-1} peak. UV-Raman spectra of C_2H_5OH, $MgCl_2(C_2H_5OH)_6$, and $Mg(OC_2H_5)_2$. The small peak at ~600 cm^{-1} could be due to Mg-O stretch in the $Mg(OC_2H_5)_2$ spectrum.

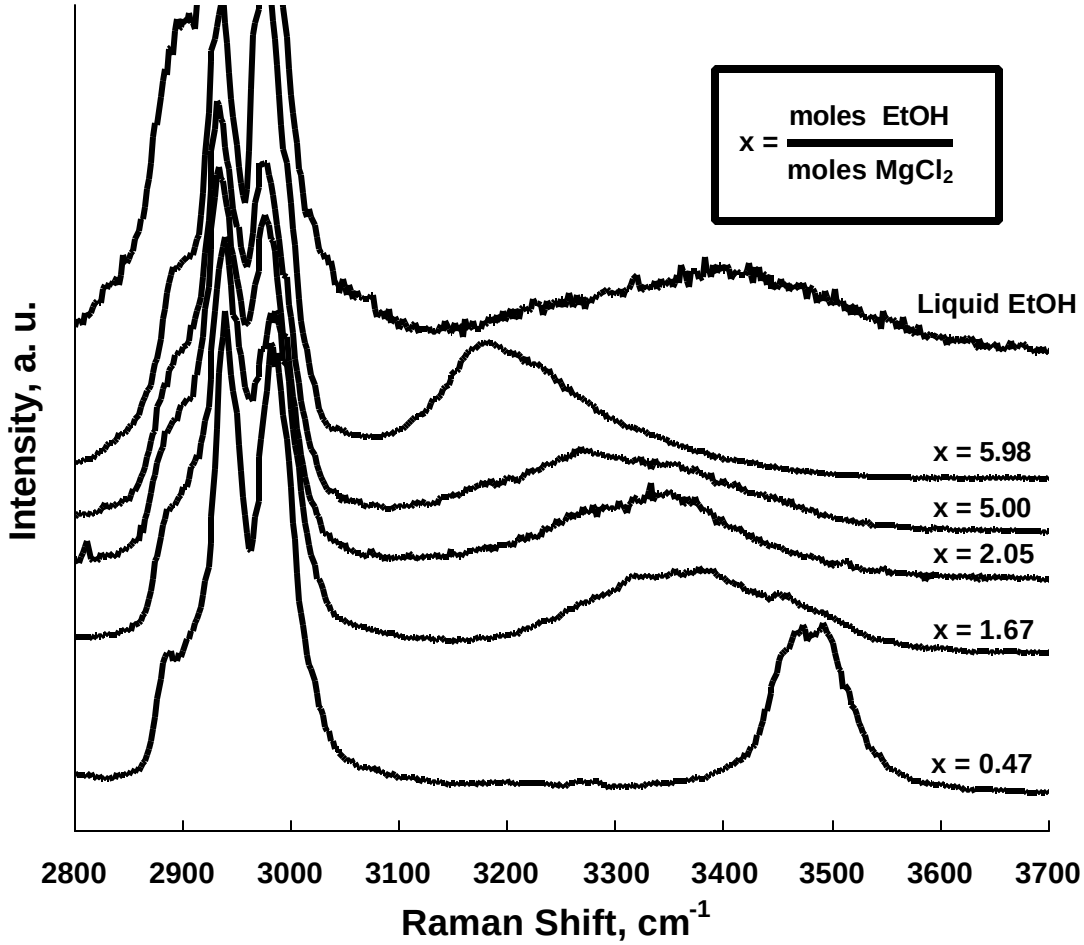

Figure 4.9 UV-Raman spectra of powdered $MgCl_2(C_2H_5OH)_x$ adducts and liquid ethanol. The peaks between 2890 and 2990 cm^{-1} are due to C-H stretching modes of ethanol. The broad peaks between 3100 and 3500 cm^{-1} are due to O-H stretching modes of ethanol. The intensity of the methylene $\nu(CH)_{as}$ peak at ~2938 cm^{-1} has been used as an internal intensity standard.

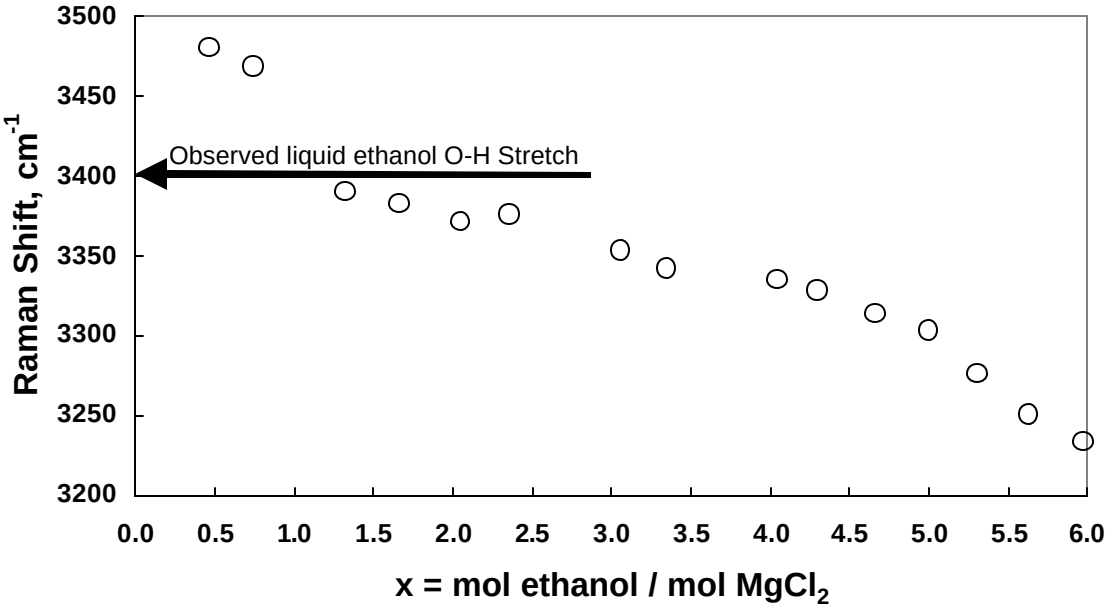

Figure 4.10 O-H peak Raman shift for $MgCl_2(C_2H_5OH)_x$ adducts shown as a function of ethanol to $MgCl_2$ molar ratio, x. Gas phase ethanol has two O-H peaks at 3660 and 3677 cm^{-1}.

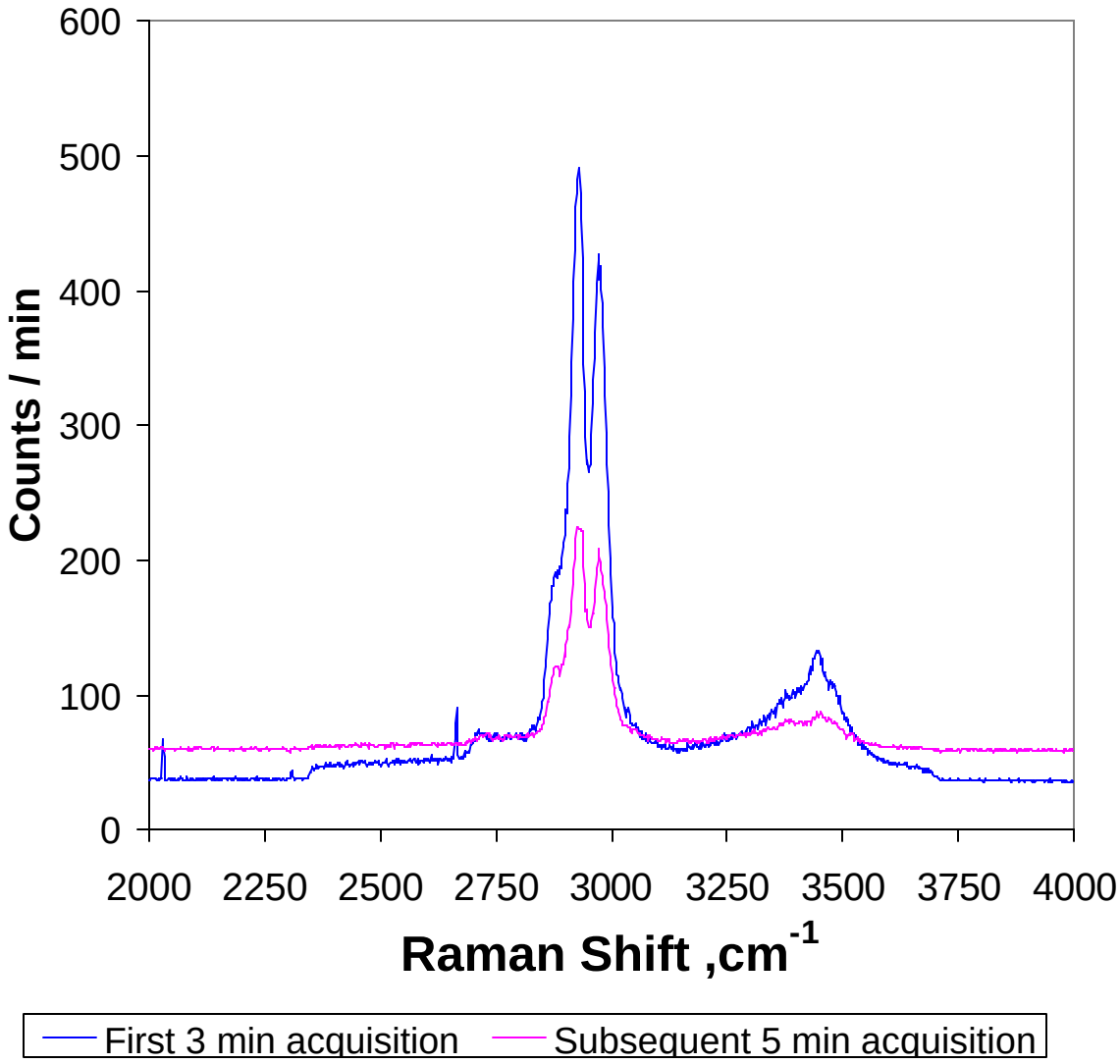

Figure 4.11 UV-Raman spectra of 42 wt% EtOH industrial Mg-ethoxide support: Data acquired in packed bed UV-Raman reactor.

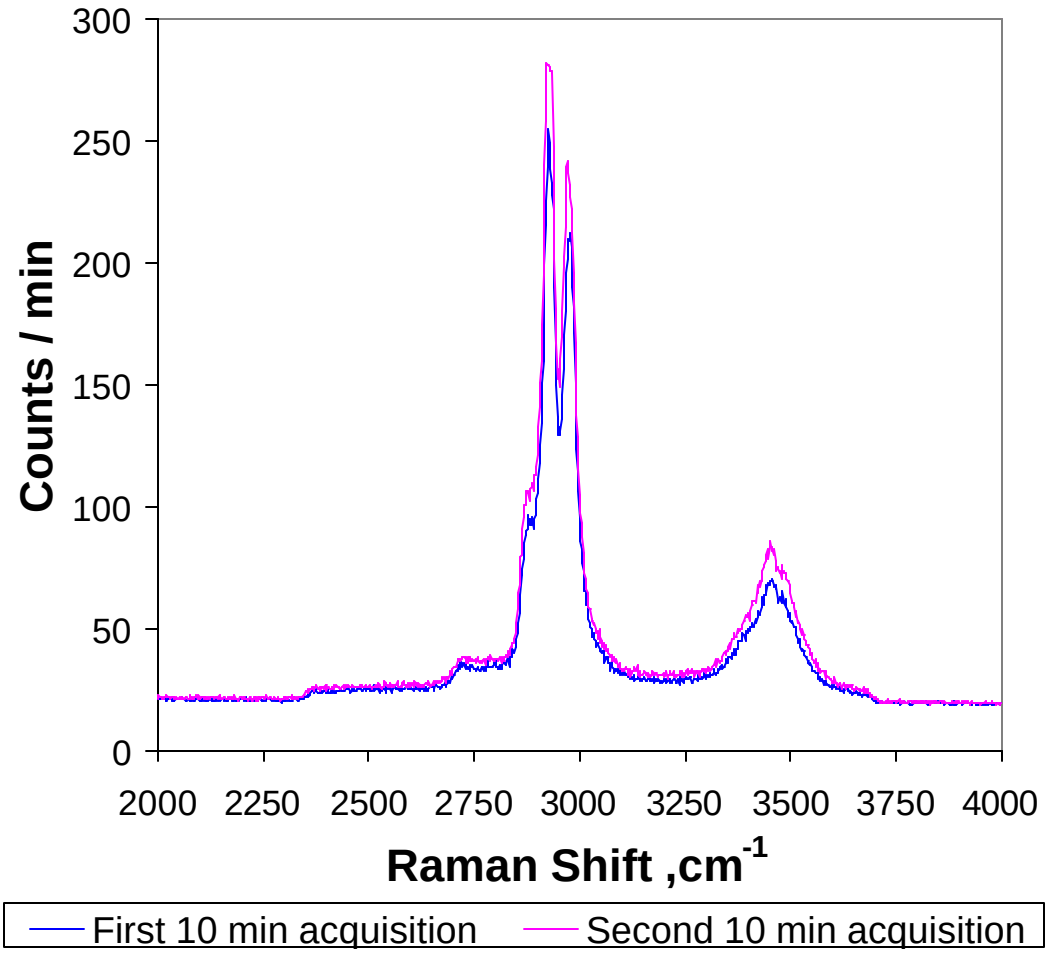

Figure 4.12 UV-Raman spectra of 42 wt% EtOH industrial Mg-ethoxide support: Data acquired in fluidized bed UV-Raman reactor.

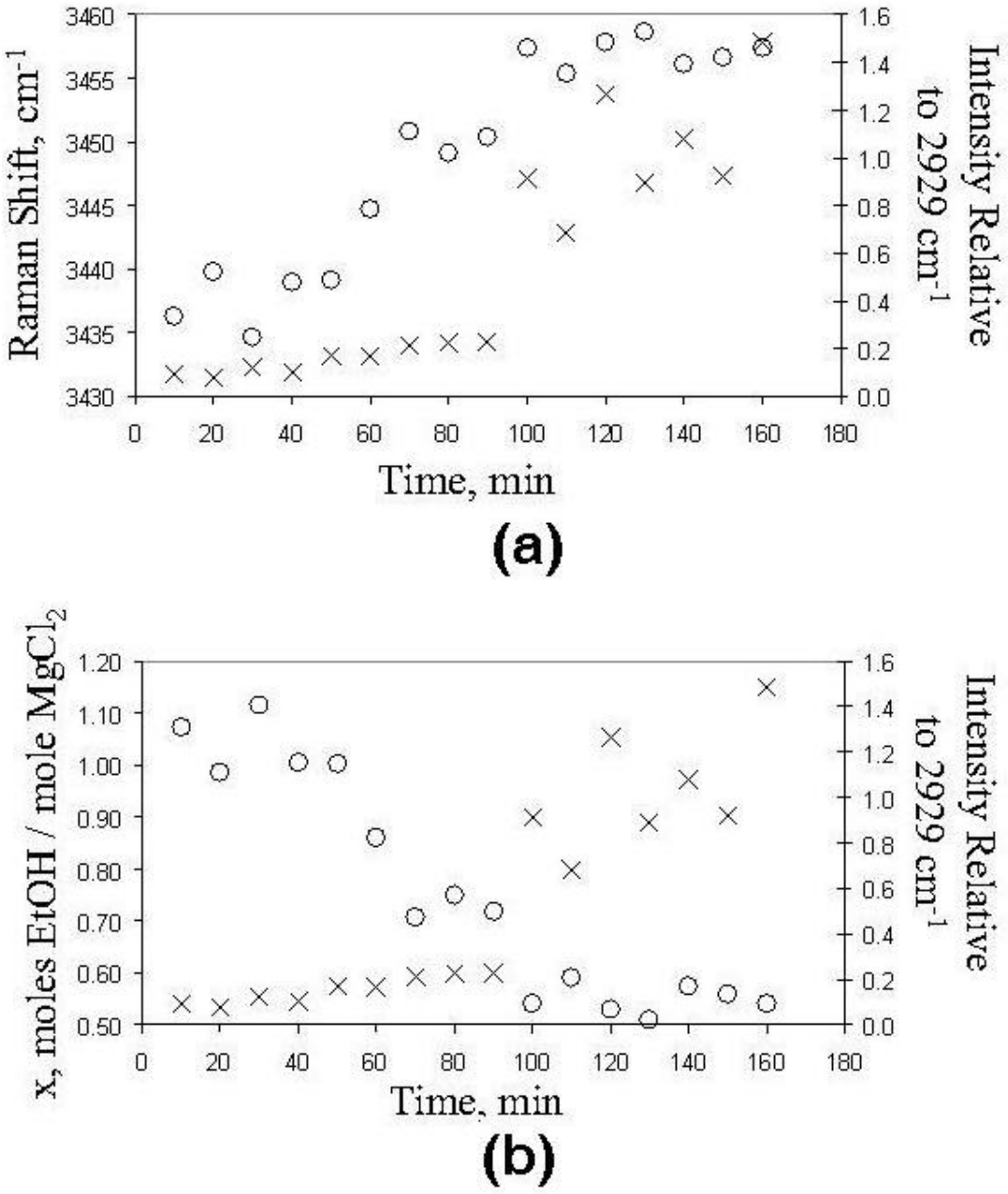

Figure 4.13 Dealcoholation of 42 wt% EtOH industrial Mg-ethoxide support: (a) Raman shift, cm^{-1} and relative intensity vs. time and (b) mole fraction, x, and relative intensity vs. time for the O-H peak that originated at 3436 cm^{-1} at t = 10 min.

Symbol Key:
O – in (a) Raman Shift, cm^{-1}
O – in (b) x, moles EtOH/moles $MgCl_2$
X – in (a) and (b) Intensity Relative to 2929 cm^{-1}

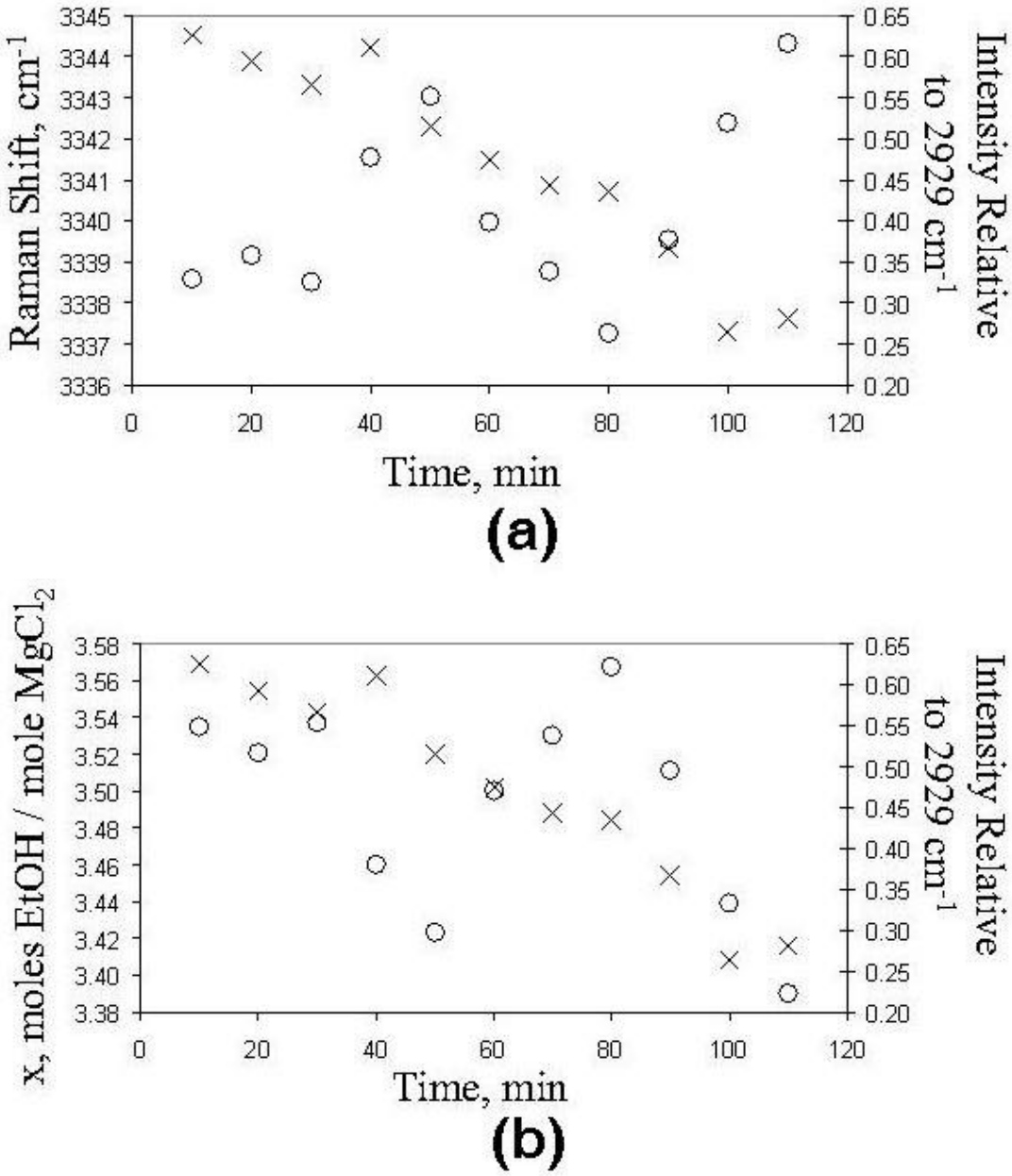

Figure 4.14 Dealcoholation of 42 wt% EtOH industrial Mg-ethoxide support: (a) Raman shift, cm^{-1} and relative intensity vs. time and (b) mole fraction, x, and relative intensity vs. time for the O-H peak that originated at 3337 cm^{-1} at t = 10 min.

Symbol Key:
O – in (a) Raman Shift, cm^{-1}
O – in (b) x, moles EtOH/moles $MgCl_2$
X – in (a) and (b) Intensity Relative to 2929 cm^{-1}

Chapter 5

Structural Characterization of Silica Supported CoMo Catalysts by UV Raman, XPS and X-ray Diffraction Techniques

Section 5.1 Introduction

CoMo catalysts supported on silica or alumina are commonly used as hydrodesulfurization (HDS) catalysts in the petroleum refining industries.[1] These systems have been extensively characterized by various techniques in both oxidized and sulfided states but contradictory conclusions have sometimes been drawn about the reciprocal effect of Mo and Co.[1] However, general agreement exists on the importance of the CoMoS species of "type II" which consist of small MoS_2 particles with Co promoter atoms located at the edges of MoS_2 slabs.[2,3] The promoting effect of Co is attributed to its electron donor capability causing reduction of the Mo oxidation state.[4] The HDS activity of the supported catalysts depends significantly on the types of support material. The support material effects the structure of the oxide precursors formed during the calcination step.[5,6] Indeed important correlations between catalytic activity and precursor oxides are found. Generally speaking, supports interacting strongly with the supported elements induce higher dispersion of the supported molybdena phase which is reflected in higher activity of the sulfided catalysts.[7] However interactions that are too strong may inhibit the subsequent formation of the MoS_2 phase, as in the case of alumina supported catalysts which are harder to sulfide

than silica supported ones. Conversely, the complete absence of interaction with the support, as in silica supported catalysts, favors sintering of the precursor oxide species with a subsequent decrease in activity. Therefore, to achieve an optimally active and stable catalyst, a compromise between the two support interactions is important. Various methods to control the interaction between supports and active species have been tried including changes of the preparation conditions, addition of complexing agents such as nitrilotriacetic acid (NTA)[8] or ethylenediamine[9] or doping the supports with different types of additives.[3,10,11] A recent investigation of sodium doped CoMo catalysts has revealed a dependence of the sodium effect on the type of support; an increase of the HDS activity with sodium was observed for the aluminosilicate support, in contrast to a decrease of activity observed at any Na loading on silica support.[12,13] The positive effect of sodium in the aluminosilicate case was attributed to the formation of β-$CoMoO_4$ species driven by sodium. This mixed oxide is characterized by tetrahedral coordination of Mo and octahedral coordination of Co and is considered a precursor to the active CoMoS species of type II having the same structural features.[9] On the contrary, based on X-ray diffraction results and on physisorption methods, the decrease of the catalytic activity in the sodium doped silica supported catalysts[12,13] was attributed to morphological effects, such as surface area and pore size distribution variation. The extent of the effect depended on the catalyst preparation. To further investigate the nature of the adsorbed species (e.g. isolated MoO_4^{2-}, mixed oxide and polyanions such as $Mo_7O_{24}^{6-}$) and the effect of sodium from the structural and electronic point of view, an X-ray photoelectron spectroscopy (XPS) and UV-Raman spectroscopy study of CoMo catalysts, supported on differently sodium doped silica,

was undertaken and is here described. Correlations between structure and activity are also discussed.

Section 5.2 Experimental

Section 5.2.1 Catalyst preparation. All catalysts were prepared starting with commercially available sodium free silica (Aldrich Chemical Company; surface area of 546 m^2/g; pore sizes10-50 Å; PZC = 3.8). For the sodium doped samples, the silica was impregnated with a solution of sodium nitrate of different concentrations, dried at 343 K for 2 h and then calcined at 773 K in air. Samples doped with sodium are labelled as **1Na**, **2Na**, **3Na**, and **4Na** where the numbers represent the wt% of sodium in the support. These supports were then loaded with molybdenum (at % Mo = 1.4) and cobalt (at % Co = 0.6) following two different procedures.

One series was prepared by incipient wetness impregnation, involving a first impregnation with an aqueous solution of $(NH_4)_6Mo_{17}O_{24}\cdot 4H_2O$. Ammonia was added in order to shift the polymolibdate $\leftrightarrow$ monomolybdate equilibrium.[14] The samples were dried for 2 h at 343 K and overnight calcined at 773 K in air. The second impregnation was with an aqueous solution of $Co(NO_3)_2\cdot 6\ H_2O$ followed by the same drying step as before. Samples prepared in this manner are labelled with **WI**.

A second set of catalysts was prepared by co-impregnation of the two metal salt solutions in the presence of the tridentate nitriloacetic acid (NTA).[8,12] The solid samples were dried at 343 K for 24 h. Unlike the first series, calcination in air was omitted. Samples prepared by this technique are labelled with **NTA**.

Reference samples, MoO_3, Co_3O_4, and $CoMoO_4$ for XPS measurements, were prepared from ammonium heptamolybdate and from cobalt nitrate precursors according to the literature.[14] Their crystallinity was checked by X-ray diffraction (JCPDS Powder diffraction Files no. 35-0609, 42-1467, 21-868 respectively.)[15]

Section 5.2.2 X-ray diffraction (XRD). X-ray diffraction measurements for structure determination were carried out with a Philips vertical goniometer using Ni-filtered Cu Kα radiation. A proportional counter and 0.05° step sizes in 2θ were used. The assignments of the various crystalline phases were based on the JPDS powder diffraction file cards.[15]

Section 5.2.3 BET Analysis. The microstructural characterization was performed with a Carlo Erba Sorptomat 1900 instrument. The surface area of the samples were obtained through the BET method using nitrogen as the probe. By analysis of the desorption curve, using the Dollimore and Heal calculation method, the pore size volume distribution was also obtained.[16]

Section 5.2.4 X-Ray Photoelectron Spectroscopy (XPS). XPS measurements were taken on a Perkin-Elmer PHI 5300 XPS spectrometer equipped with a hemispherical energy analyzer and a dual Mg/Al anode. The spectra were obtained using the non-monochromated Al Kα source (1486.6 eV). For the individual peak energy regions, a pass energy of 20 eV set across the hemispheres was used. Survey spectra were measured at 50 eV pass energy. The sample powders were analysed as pellets, mounted on a double-sided adhesive tape. The pressure in the analysis chamber was in the range of 10^{-8} Torr during data collection. The constant charging of the samples was removed by referencing all the energies to the C 1s set at 285.1 eV, arising

from the adventitious carbon. The invariance of the peak shapes and widths at the beginning and at the end of the analyses ensured absence of differential charging. Analysis of the peaks were based on non-linear least square fitting program using properly weighted sum of Lorentzian and Gaussian component curves after background subtraction according to Shirley and Sherwood.[17,18] Constraints on the intensity ratios of the two Mo 3d and Co 2p doublet components were used in accord with the spin orbit coupling processes. Atomic concentration were calculated from peak intensity as described in Chapter 2. The binding energy (BE) values are quoted with a precision of ± 0.15 eV. Contact of the samples with air was minimised during sample loading. In order to check for possible radiation damage, spectra of the Mo 3d and Co 2p regions were acquired as the first and last regions. No differences were observed.

Section 5.2.5 UV- Raman Spectroscopy. In order to eliminate interference from photodecomposition and thermal degradation, the fluidized bed (FB) reactor has been used.[19] In this type of set up the powder sample is placed on top of a fritted disc. Helium gas, flowing through the sample, produced vertical lift. Stable fluidization was achieved by adding an electric shaker.

Figure 5.1 is an overview of the UV-Raman spectroscopy experimental set up. The excitation source is the 244 nm output of a Lexel SHG, an intracavity doubled, continuous wave Ar^+ laser. The 244 nm beam is focused at 45^o to the sample normal by a 2 cm focal length spherical lens. The Raman scattered light is collected by a 50 mm diameter f/2 fused silica lens; this corresponds to a solid angle of collection of 0.20 sr. The collected scattered light is focused on the entrance slit of a f/3.7 Triplemate triple spectrometer by a 160 mm focal length lens. The filter stage of the Triplemate

contains two 2400 gr/mm diffraction gratings for efficient rejection of stray reflections and the intense Rayleigh scattered light. A 2400 gr/mm diffraction grating is used in the dispersion stage. The spectrum is collected on a back thinned, UV-enhanced liquid-nitrogen-cooled 1340 x 100 pixel CCD detector. The quantum efficiency of the CCD array at 244 nm is approximately 33%. The spectral resolution is ~24 cm^{-1}. Spectra obtained between 700 and 1500 cm^{-1} were calibrated using the well-known Raman shifts of cyclohexane.[20] The spectrometer response function was assumed to be constant and no attempt was made to correct the spectra. The absolute signal intensity did vary between samples due to slight differences in the focus of the incident laser on the fused silica capillary tubes. To facilitate qualitative comparison of peak intensities between spectra, one peak in a given spectral region for each sample was chosen as internal intensity standard.

Sample integrity under the UV laser beam was investigated. If the laser beam were inducing thermal or photochemical damage, the Raman intensity would not increase proportionally with the incident laser power. Under stationary conditions, sample degradation was already observed at 9 mW, especially for the NTA series, whereas under fluidized bed conditions, Raman spectra recorded at 2, 9, 18 and 36 mW exhibited signal intensity which increased linearly with laser power. All spectra reported here were obtained at 36 mW.

Section 5.3 Results

Section 5.3.1 BET and PZC. Table 5.1 summarizes the surface areas obtained from BET analysis for the catalyst samples. The meaning of the catalyst sample names

is described in section 5.2.1. The decrease of the surface area of the supports is related to the amount of the added sodium.[21] Consecutive calcinations can also reduce the surface area.

The point of zero charge (PZC) of the silica support as a function of the amount of added sodium was determined by mass titration.[22] The PZC is determined by monitoring the pH as more of the solid sample is added to solution. The steady-state pH value is the PZC. The PZC values and the surface areas relative to pure silica and to the sodium doped supports are reported in Table 5.2. Addition of sodium to the silica support induces an increase of the PZC. At around 2 atomic % of sodium, the pH (PZC) > 9 is reached, corresponding to the dissolution of silica.[23]

Section 5.3.2 XRD Results. X-ray diffraction patterns of the sodium free samples prepared by the NTA procedure, exhibit the broad band typical of amorphous silica (data not shown).[12,13] In agreement with previous observations, addition of sodium to silica, followed by calcination at 773 K, induces the transformation from amorphous to cristobalite.[21] For the WI series in Figure 5.2, diffraction lines attributed to β-$CoMoO_4$ are present.[12] Moreover, diffraction lines, from Na_2MoO_4 phase, are observed in the case of samples with Na loading above 2.7 at %.

Section 5.3.3 UV-Raman Results. In Figure 5.3 the Raman spectra of the WI series with varying sodium content are displayed. In the SilWI sample (Figure 5.3a) a broad peak centered at 970 cm^{-1} with a shoulder at 944 cm^{-1} is detected. The peak at 944 cm^{-1} is attributed to $Mo_7O_{24}^{6-}$ (Mo=O Raman band at 946-951 cm^{-1}).[24] The peak at 970 cm^{-1} is attributed to large polymolybdate clusters such as $Mo_8O_{26}^{4-}$ (Mo=O Raman band at 958-960 cm^{-1}.[24,25] Formation of MoO_3, especially after calcination at high

temperature, characterized by peaks in the range of 990 - 1000 cm^{-1} can also be postulated due to the weak interaction between Mo(VI) and SiO_2.[24,26-28] Some contribution from Mo-O-Co stretching vibrations in $CoMoO_4$ species are also observed in the region at 930 cm^{-1} and 870 cm^{-1}.[29]

In the presence of 1% wt of sodium ions the spectrum changes (Figure 5.3b). The intensity of the peak at 970 cm^{-1} decreases, while a broad band at 916 cm^{-1} appears. Moreover, small features at 840 cm^{-1}, 892 cm^{-1} and 807 cm^{-1} are distinguished. The band at around 840 cm^{-1} can be associated with the Mo-O-Mo asymmetric stretching mode of the octahedral molybdate species. The peaks at 892 and 807 cm^{-1} are attributed to the stretching modes of Mo=O bond of the tedrahedral molybdate species due to the formation of sodium molybdate.[24] The peak at 916 cm^{-1} can be attributed to the Mo=O stretching mode of MoO_4^{2-} species with distorted tetrahedral symmetry.[30] Indeed, this distortion will lead to a rehybridization and strengthening of terminal Mo=O bonds and consequently to a shift of the Mo=O stretching frequency to higher wavenumbers with respect to the undistorted symmetry.[27]

The spectrum of the sample doped with 4 % wt of sodium exhibits two sharp peaks at 807 cm^{-1} and 892 cm^{-1} typical of Na_2MoO_4. A strong peak at 1060 cm^{-1} is observed due to nitrate residue from the sodium precursor which is still present in the samples. The polymeric molybdate species have totally disappeared and the coordination of Mo has changed from octahedral, as in the polymolybdates, to tetrahedral, as in the sodium monomolybdate.

In Figure 5.4 the Raman spectra of the NTA series as a function of the sodium content are shown. In this case, the spectra are quite similar to each other, suggesting

that the surface oxide species are not influenced much by the presence of differing amounts of sodium. Unlike the WI samples, the region of 990-1000 cm^{-1} does not contain any features due to MoO_3 species. The samples with no sodium and with 1% wt sodium exhibit a broad band centred at 915 cm^{-1} with shoulders at ca. 960, 930, 890 and 860 cm^{-1}. The broadness of the signal and its positions indicates a mixture of several Mo species with different symmetries. The peak at 915 cm^{-1} may arise from $[MoO_3(NTA)]^{3-}$ complex anchored to the silica surface and from MoO_4^{2-} with distorted tetrahedral symmetry.[26] Contribution from heptamolydbate (peaks at 937 cm^{-1} and 886 cm^{-1})[31], $CoMoO_4$ (930 cm^{-1}), smaller Mo units like $Mo_2O_7^{2-}$ (932 cm^{-1})[24] and MoO_4^{2-} (892 cm^{-1} and 803 cm^{-1})[24] are also present in the large envelope. With an increasing amount of sodium the main band shifts to 905 cm^{-1}, as observed in the spectra of the samples containing 3 and 4 % wt of sodium. The shift can be attributed to the increase of the monomeric Mo species relative to the $[MoO_3(NTA)]^{3-}$ ligand complex component and to a decrease of the surface concentration of the polymolybdate species. The peaks at 1060 cm^{-1} and 1044 cm^{-1} are again due to nitrate ions from sodium and cobalt precursors respectively.

Section 5.3.4 XPS Results. The Mo $3d_{5/2}$, Co $2p_{3/2}$, O 1s and Si 2p binding energies of the model compounds are listed in Table 5.3. The values are in agreement, within experimental errors, with literature work.[14,32] The Co $2p_{3/2}$ of the mixed oxide Co_3O_4 could be fitted with two peaks, one at low energy corresponding Co^{2+} species and the other at higher value corresponding to a Co^{3+} oxidation state. Typically, the Co 2p spectra of oxidized cobalt species are characterized by shake-up satellite structures at 6 eV on the high energy side of the main Co $2p_{3/2}$ and Co $2p_{1/2}$ peaks. The intensity of

the satellites is also related to the chemical environment, being much stronger in the mixed $CoMoO_4$ oxide as compared to the Co_3O_4 .[14]

The experimental XPS spectra of the Mo 3d level for the various catalysts prepared by classic wet impregnation (WI) of the differently sodium doped supports are shown in Figure 5.5. The two spin – orbit components, $3d_{5/2}$ and $3d_{3/2}$, are present. The energy separation between the two states is constant and fixed at 3.1 eV along with the relative intensity ratio ($3d_{5/2}$ to $3d_{3/2}$) of 1.5 in the peak fitting routine. As shown in Figure 5.5 the resolution of the Mo 3d spectra improves upon addition of sodium to the silica support. The principal binding energies and the corresponding full width at half maximum (FWHM) for the WI samples are listed in Table 5.4. For comparison, samples with no Co are also reported. The binding energy of Mo $3d_{5/2}$, typical of Mo (VI)[33], ranges from 233.2 eV for the sodium free and the low sodium content samples, to 231.8 eV for the more highly sodium loaded catalysts. At the same time a decrease of the FWHM with sodium is also observed. This is observed for the samples without cobalt as well. The constant line widths of the Si 2p and O 1s excludes the possibility of any charging effects to account for the origin of Mo 3d FWHM variation. The values of the sodium free samples are quite close to the value of the unsupported MoO_3, in accordance with a rather weak or absent electronic interaction with the support.[33]

The Si 2p binding energy of the samples are close to 103.5 eV found for pure silica. No trend can be envisioned for the Na 1s binding energy as the sodium doping is increased. Comparison of the XPS derived Na atomic concentration of the CoMo samples with Mo samples, indicates that repeated calcinations induce sodium segregation to the surface.

In Figure 5.6 the Co 2p spectra of two selected samples, SilWi and 4NaSilWI, are shown. The Co 2p peaks do not shift with increasing sodium doping. The increase of the Co 2p / Si 2p intensity ratio with increasing sodium could arise from an increase of the cobalt dispersion, as already observed in alumina supported cobalt.[29]

The binding energies and the intensity ratios of the NTA prepared samples, listed in Table 5.5, are rather unchanged by the increase of sodium in the support. The organic ligand, NTA, makes the exact determination of the position of the referencing C 1s more difficult. As a consequence, variations of the values are attributed to experimental error. The absence of a support effect on the binding energy values of the supported elements would agree with the supposed role of the organic ligand which tends to decrease the interaction with the support.[8]

Section 5.4 Discussion

Section 5.4.1 WI Samples. The UV Raman spectroscopy, along with the XPS results, has clearly indicated that in the CoMo catalyst supported on pure silica prepared by classic wet impregnation, a mixture of polymolybdate oxides are formed. The assignment of the various peaks agrees with the presence of large clusters, like $Mo_7O_{24}^{6-}$, $Mo_8O_{26}^{4-}$ and also MoO_3. The presence of sodium in the silica transforms the original polymolybdate surface phases into monomeric Na_2MoO_4, leading to the change from octahedral coordination of Mo (VI) to tetrahedral coordination.[34]

This shift from polymeric to monomeric molybdate structures can be accounted for by examining the effect of pH of the solution and the support surface during the catalyst preparation steps. Oxymolybdenic species in aqueous solution are in

equilibrium between $(MoO_4)^{2-}$ and $(Mo_xO_y)^{n-}$, depending upon pH, temperature and concentration of the solution. The pH of 8 for the precursor impregnating solution would favour formation of monomeric Mo units according to the following equilibrium:

$$Mo_7O_{24}^{6-} + 4H_2O \Leftrightarrow MoO_4^{2-} + 8H^{+} \qquad (5.1)$$

However, since pure silica is characterized by an acidic PZC, one can assume that the monomeric units forming in solution can easily polymerize at the solid surface. The addition of sodium by impregnation followed by high temperature calcination induces a decrease of the silica surface acidity (as shown in Table 5.1) with a subsequent shifting of the equilibrium to the right in (5.1). Similar Raman results were obtained for alumina supported Mo catalysts in which the depolymerization of polymolibdate species was promoted by increasing K^+ content.[31]

The Mo 3d and Co 2p binding energies indicate a very weak interaction between supported Mo (VI) and Co (II) with the pure silica support. As the sodium content increases, the FWHM and BE of the Mo 3d peaks decrease. The decrease in binding energy can be attributed to an electron donor effect by sodium.[28] The larger FWHM of the SilWI sample is attributed to a mixture of polymeric oxymolybdates and to a lesser extent, a possible Mo (V) species caused by the reducing action of NH_3 formed by the decomposition of the ammonium salt.[34] The decrease in the FWHM with increasing sodium content agrees with the Raman results that indicate a shift from a mixture of polymolybdates towards a monomolybdate species.

The Raman spectra and the XPS results are not conclusive about the chemical state of cobalt. The XPS intensity ratio of the main $Co2p_{3/2}$ peak over the shake-up satellite, suggests that Co(II) species are formed preferentially to Co_3O_4. Only in the

Raman spectra of the sodium free sample are features related to $CoMoO_4$ surface species present. In the presence of sodium, Na_2MoO_4 particles are formed in place of $CoMoO_4$. The decrease of HDS catalytic activity with increasing sodium doping of the WI catalysts can be attributed to the absence of $CoMoO_4$ surface species which are considered a precursor for the active CoMoS entity.[12]

Section 5.4.2 NTA Samples. XPS and UV-Raman spectroscopy indicate very little change with increased sodium doping of the NTA prepared catalysts. Raman spectra show the presence of vibrations from a $[MoO_3(NTA)]^{3-}$ complex anchored to the silica surface, a MoO_4^{2-} species with distorted tetrahedral symmetry, and a $CoMoO_4$ species.[26] The shift of the center of the broad peak from 915 cm^{-1} to 905 cm^{-1} is attributed to an increase of the monomeric MoO_4^{2-} species with respect to the $[MoO_3(NTA)]^{3-}$ complex and to the $CoMoO_4$ species. XPS spectra of the samples with and without sodium are similar and are in agreement with the Raman results. Any effect the sodium could have on the binding energy of Mo 3d and Co 2p is modulated by the presence of the organic ligand which is known to shield the Mo and Co from the increased electron density from the sodium.

The decrease in HDS activity with increasing sodium content for the NTA catalysts can therefore be accounted for by considering the structural changes induced by sodium.[12] The structural transformation of the polymolybdate into the Na_2MoO_4 monomolybdate reduces the concentration of $CoMoO_4$ species with a resultant loss in HDS activity.[12] As expected from the literature, the activity of the NTA prepared samples is enhanced relative the WI samples.[8]

Section 5.5 Conclusion

This study has shown that addition of sodium to the silica support affects the structure and the electronic properties of the molybdenum oxides formed at the surface of the supported CoMo catalysts. In the samples prepared by classic wet impregnation, the high temperature calcinations drive the sodium ions to the surface increasing the PZC. The increased PZC drives the equilibrium from polymolybdate to monomolybdates species forming Na_2MoO_4 compounds at the expense of the active precursor, $CoMoO_4$. The formation of sodium molybdates species, which are not good precursors for the active site in the HDS of thiophene may account for the decrease of HDS activity observed in previous studies. In the NTA prepared samples, the complexing action of the organic ligand, limits the structural and electronic effects of sodium. This shielding capability of the NTA ligand could account for the increased HDS activity of the NTA catalysts over the WI catalysts.

Section 5.6 References

(1) Topsoe, H.; Clausen, B. S.; Massoth, F. E. *Hydrotreating Catalysis*; Springer: Berlin, 1988.

(2) Topsoe, N.-Y.; Topsoe, H. *I. Catal.* **1983**, *84*, 386.

(3) Bouwens, S. M. A. M.; van Zon, F. B. M.; van Dijk, M. P.; van der Kraan, A. M.; de Beer, V. H. J.; van Veen, J. A. R.; Koningsberger, D. C. *J. Catal.* **1994**, *146*, 375.

(4) Harris, S.; Chianelli, R. R. *J. Catal.* **1986**, *98*, 17.

(5) Breysse, M.; Portefaix, J. L.; Vrinat, M. *Catal. Today* **1991**, *10*, 489.

(6) Muralidhar, G.; Massoth, F. E.; Shabtai, J. *J. Catal.* **1984**, *85*, 44.

(7) Lauritsen, J. V.; Helveg, S.; Laegsgaard, E.; Stensgaard, I.; Clausen, B. S.; Topsoe, H.; Besenbacher, F. *J. Catal.* **2001**, *197*, 1.

(8) van Veen, J. A. R.; Gerkema, E.; van der Kraan, A. M.; Knoster, A. *J. Chem. Soc. Chem. Commun.* **1987**, 1684.

(9) Brito, J. I.; Barbosa, A. L. *J. Catal.* **1997**, *171*, 467.

(10) Olorunyolemi, T.; Kydd, R. A. *Catal. Lett.* **1999**, *59*, 27.

(11) Adachi, M.; Contescu, C.; Schwarz, J. A. *J. Catal.* **1996**, *162*, 66.

(12) Venezia, A. M.; Raimondi, F.; La Parola, V.; Deganello, G. *J. Catal.* **2000**, *194*, 393.

(13) Venezia, A. M.; La Parola, V.; Deganello, G.; Cauzzi, D.; Leonardi, G.; Predieri, G. *J. Appl. Catal.* **in press**.

(14) Koranyi, T. I.; Manninger, I.; Paal, Z.; Marks, O.; Gunter, J. R. *J. Catal.* **1989**, *116*, 422.

(15) *JCPDS Powder Diffraction File*; Int. Centre for Diffraction Data: Swarthmore.

(16) Gregg, S. J.; Sing, K. S. *Adsorption, Surface Area and Porosity*, 2nd ed.; Academic Press: San Diego, 1982.

(17) Shirley, D. A. *Phys. Rev.* **1972**, *B5*, 4709.

(18) *Handbook of X-Ray Photoelectron Spectroscopy*; Perkin-Elmer Corp.: Eden Prairie, MN, 1992.

(19) Chua, Y. T.; Stair, P. C. *J. Catal.* **2000**, *196*, 66.

(20) McCreery, R. L. *Raman Spectroscopy for Chemical Analysis*; Wiley-Interscience: New York, 2000; Vol. 157.

(21) Venezia, A. M.; La Parola, V.; Longo, A.; Martorana, A. *J. Sol. State Chem.* **2001**, *161*, 373.

(22) Subramanian, S.; Noh, J. S.; Schwarz, J. A. *J. Catal.* **1988**, *114*, 433.

(23) van Santen, R. A.; van Leeuven, P. W. N. M.; Moulijn, J. A.; Averill, A. In *Stud. Surf. Sci. and Catal.*; Elsevier: Amsterdam, 1999; Vol. 123; pp Chapter 9.

(24) Mestl, G.; Srinivasan, T. K. K. *Chem. Rev. Sci. Eng.* **1998**, *40*, 451.

(25) Wachs, I. E. *Catalysis Today* **1996**, *27*, 437.

(26) Medici, L.; Prins, R. *J. Catal.* **1996**, *163*, 38.

(27) Kantschewa, M.; Delannay, F.; Jeziorowski, H.; Delgado, E.; Eder, S.; Ertl, G.; Knozinger, H. *J. Catal.* **1984**, *87*, 482.

(28) Venezia, A. M.; Rossi, A.; Duca, D.; Martorana, A.; Deganello, G. *Appl. Catal. A* **1995**, *125*, 113.

(29) Lycourghiotis, A.; Defosse, C.; Delannay, F.; Lemaitre, J.; Delmon, B. *J. C. S. Faraday I* **1980**, *76*, 1677.

(30) Xiong, G.; Feng, Z.; Li, J.; Yang, Q.; Ying, P.; Xin, Q.; Li, C. *J. Phys. Chem. B* **2000**, *104*, 3581.

(31) Verbruggen, N. F. D.; von Hippel, L. M. J.; Mestl, G.; Lengeler, B.; Knozinger, H. *Langmuir* **1994**, *10*, 3073.

(32) Okamoto, Y.; Imanaka, T.; Teranishi, S. *J. Catal.* **1980**, *65*, 448.

(33) Plyuto, Y. V.; Babich, I. V.; Plyuto, I. V.; van Langeveld, A. D.; Moulijn, J. A. *Appl. Surf. Sci.* **1997**, *119*, 11.

(34) Lycourghiotis, A.; Defosse, C.; Delannay, F.; Delmon, B. *J. C. S. Faraday I* **1980**, *76*, 2052.

Catalysts	**S (m^2/g)**
WI	**450**
1NaSilWI	**69**
2NaSilWI	**14**
3NaSilWI	**18**
4NaSilWI	**13**
SilNTA	**343**
1NaSilNTA	**208**
3NaSilNTA	**22**
4NaSilNTA	n. d.

Table 5.1 Surface areas, S, of the catalysts determined by BET nitrogen adsorption.

Supports	**S (m^2/g)**	**PZC (pH)**	**at %Na**
Silica	**550**	**3.8**	**0.0**
1NaSil	**200**	**n.d**	**0.9**
2NaSil	**22**	**9.6**	**1.8**
3NaSil	**25**	**n.d.**	**2.7**
4NaSil	**13**	**9.5**	**3.6**

Table 5.2 BET Surface Area (S), Point of Zero Charge (PZC), and sodium content in atomic percent of the pure silica and sodium doped silica supports.

Samples	**Mo $3d_{5/2}$**	**Co $2p_{3/2}$**	**O 1s**	**Si 2p**
MoO_3	233.2 (1.8)		531.4 (1.8)	
Co_3O_4		780.1 (1.8)	530.4 (1.5)	
		781.6 (1.8)		
CoO[a]		780.7		
$CoMoO_4$	232.6 (1.8)	781.0 (3.2)	530.5 (2.2	
$(NH_4)_6Mo_7O_{24}$	232.6 (2.2)		530.5 (1.9)	
SiO_2			532.3 (2.3)	103.5 (2.4)

[a] From Ref. 32

Table 5.3 XPS binding energy (eV) data for reference compounds. The FWHM are given in parentheses.

Catalyst	Mo $3d_{5/2}$	Co $2p_{3/2}$	O 1s	Si 2p	Co 2p / Si 2p	Mo 3d / Si 2p	at% Na
SilMo	232.8	-	532.8	103.9	0.0	0.3	0.0
	(3.6)		(2.4)	(2.3)			
1NaSilMo	233.2	-	533.1	103.9	-	0.2	0.3
	(2.3)		(2.4)	(2.4)			(0.9)
3NaSilMo	232.2	-	532.7	103.7	0.0	0.2	3.0
	(1.8)		(2.2)	(2.4)			(2.7)
4NaSilMo	232.3	-	532.8	103.6	-		4.2
	(1.9)		(2.1)				(3.6)
SilWI	232.7	781.8	532.8	103.9	0.2	0.3	0.0
	(3.2)	(3.6)	(2.4)	(2.3)			
1NaSilWI	232.5		532.8	103.9	0.1	0.2	0.8
	(2.3)		(2.4)	(2.3)			(0.9)
2NaSilWI	232.3		533.0	104.1	0.5	0.3	2.9
	(1.8)		(2.3)	(2.3)			(1.8)
3NaSilWI	232.2		532.8	103.4	0.7	0.5	5.7
	(1.7)		(2.2)	(2.3)			(2.7)
4NaSilWI	231.8	781.9	532.4	103.4	0.6	0.4	7.0
	(1.6)	(3.8)	(2.2)	(2.2)			(3.6)

Table 5.4 XPS binding energy (eV), Co 2p / Si 2p and Mo 3d / Si 2p intensity ratios, and XPS derived Na atomic % for the WI catalysts. The full width half maximum (FWHM) and the nominal atomic% Na are given in parentheses. The results for the Mo catalyst (no Co added), SilMo, 1NaSilMo and 3NaSilMo are also listed.

Catalyst	**Mo $3d_{5/2}$**	**Co $2p_{3/2}$**	**O 1s**	**Si 2p**	**Co 2p / Si 2p**	**Mo 3d / Si 2p**	**at %Na**
SilNTA	232.6	781.5	532.8	103.8	0.2	0.2	0.0
	(3.2)	(4.0)	(2.4)	(2.3)			
1NaSilNTA	232.9	781.7	532.9	104.1	0.2	0.2	0.6
	(2.9)	(4.2)	(2.4)	(2.2)			
3NaSilNTA	232.2	779.9	532.3	103.5	0.2	0.2	3.1
	(2.9)	(3.8)	(2.1)	(2.1)			
4NaSilNTA	232.3	780.4	533.0	104.1	0.2	0.2	3.1
	(2.9)	(4.1)	(2.2)	(2.1)			

Table 5.5 XPS binding energy (eV), Co 2p / Mo 3d and Mo 3d / Si 2p intensity ratios, and XPS derived Na atomic % for the NTA catalysts. The full widths at half maximum (FWHM) are given in parentheses.

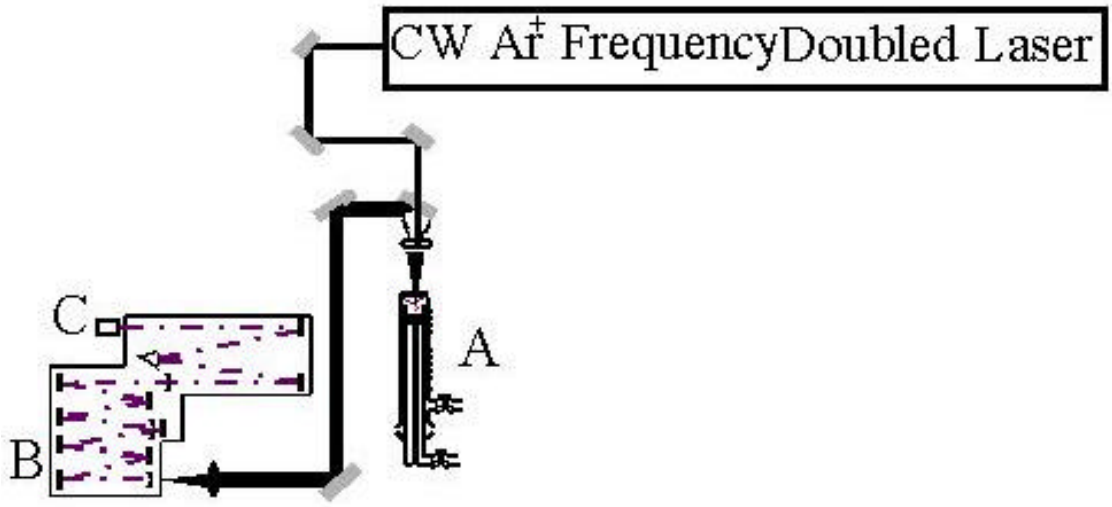

Figure 5.1 Experimental UV-Raman setup. The 244 nm laser beam is focused on the sample at 90° by a 2 cm focal length spherical lense (**A**). The light scattered normal to the sample is collected as focused on the entrance slit of the Triplemate Spectrometer (**B**). The filtered and dispersed light is collected with a back-thinned, UV-enhanced CCD detector cooled by a liquid nitrogen resevoir (**C**).

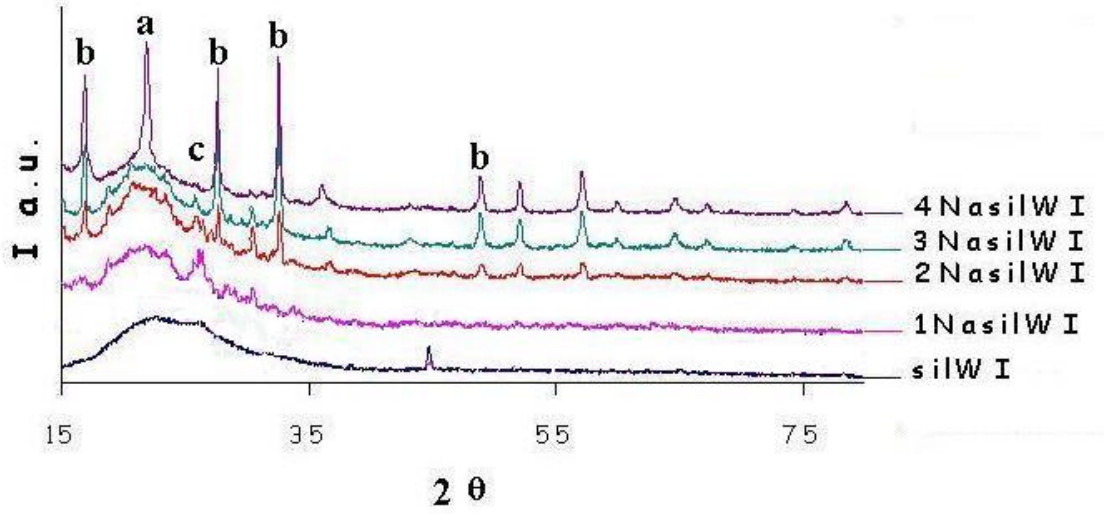

Figure 5.2 X-Ray Diffraction data for WI samples. The reflections labelled are assigned as (a) Cristobalite, (b) Sodium molybdate (Na_2MoO_4), and (c) $CoMoO_4$.[15]

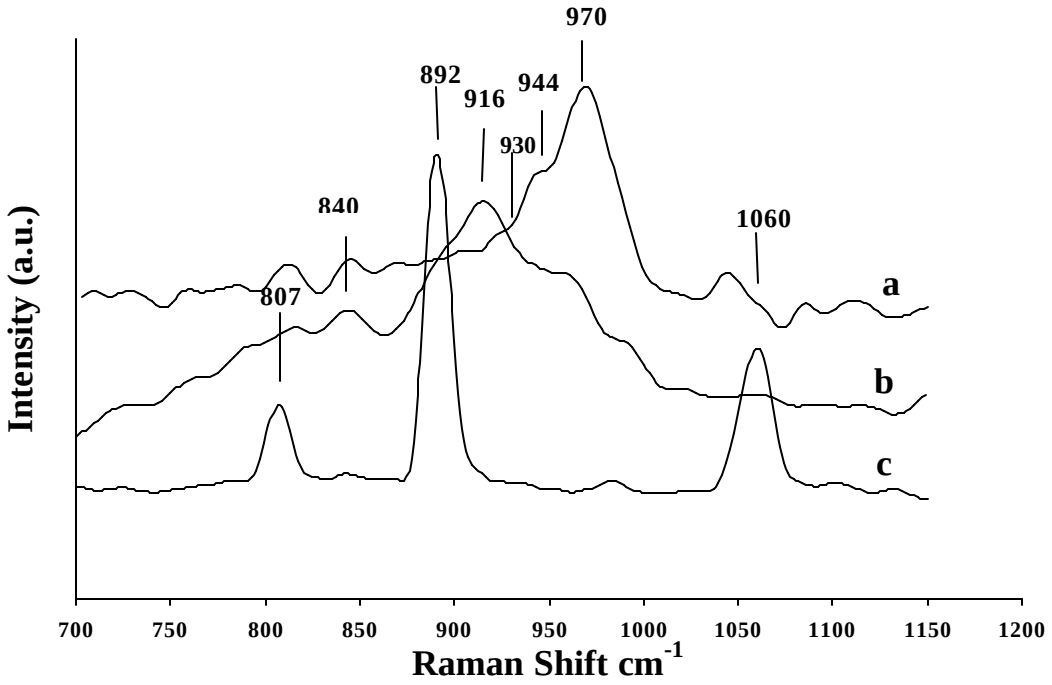

Figure 5.3 UV-Raman spectra of (a) SilWI, (b) 1NaSilWI, and (c) 3NaSilWI.

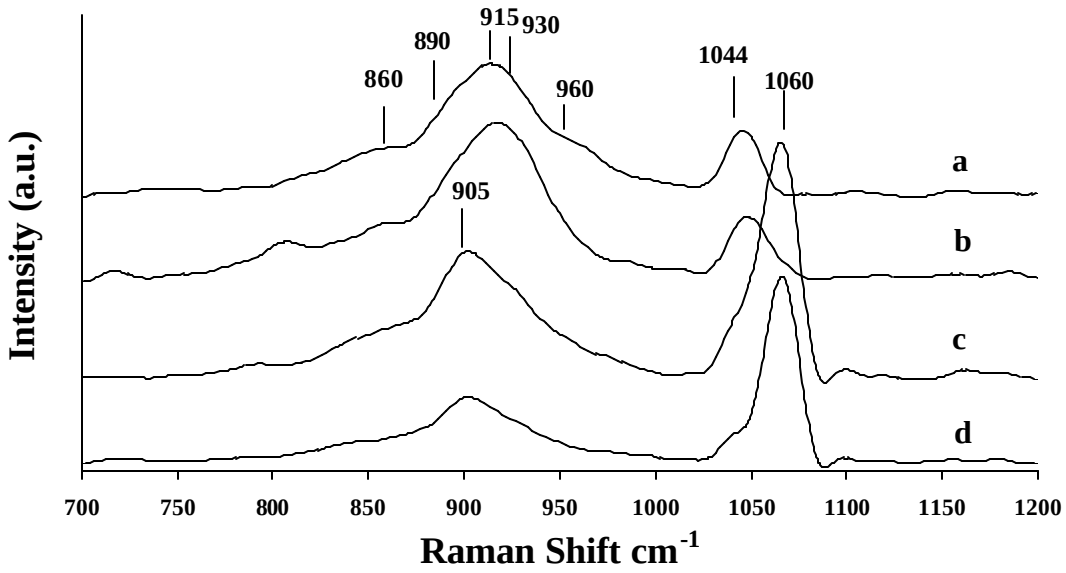

Figure 5.4 UV-Raman spectra of (a) SilNTA, (b) 1NaSilNTA, (c) 3NaSilNTA, and (d) 4NaSilNTA.

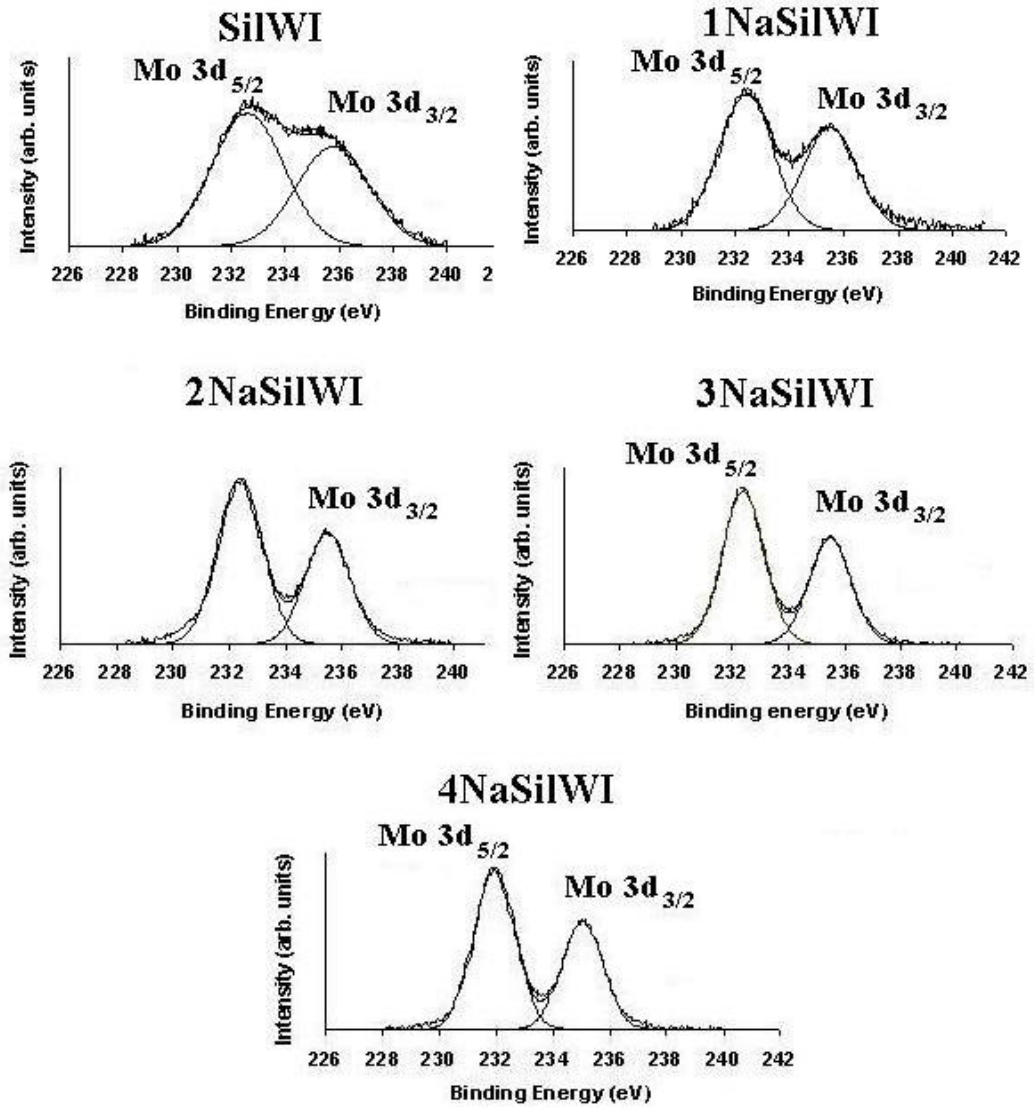

Figure 5.5 Mo 3d XPS spectra of the WI catalyst samples.

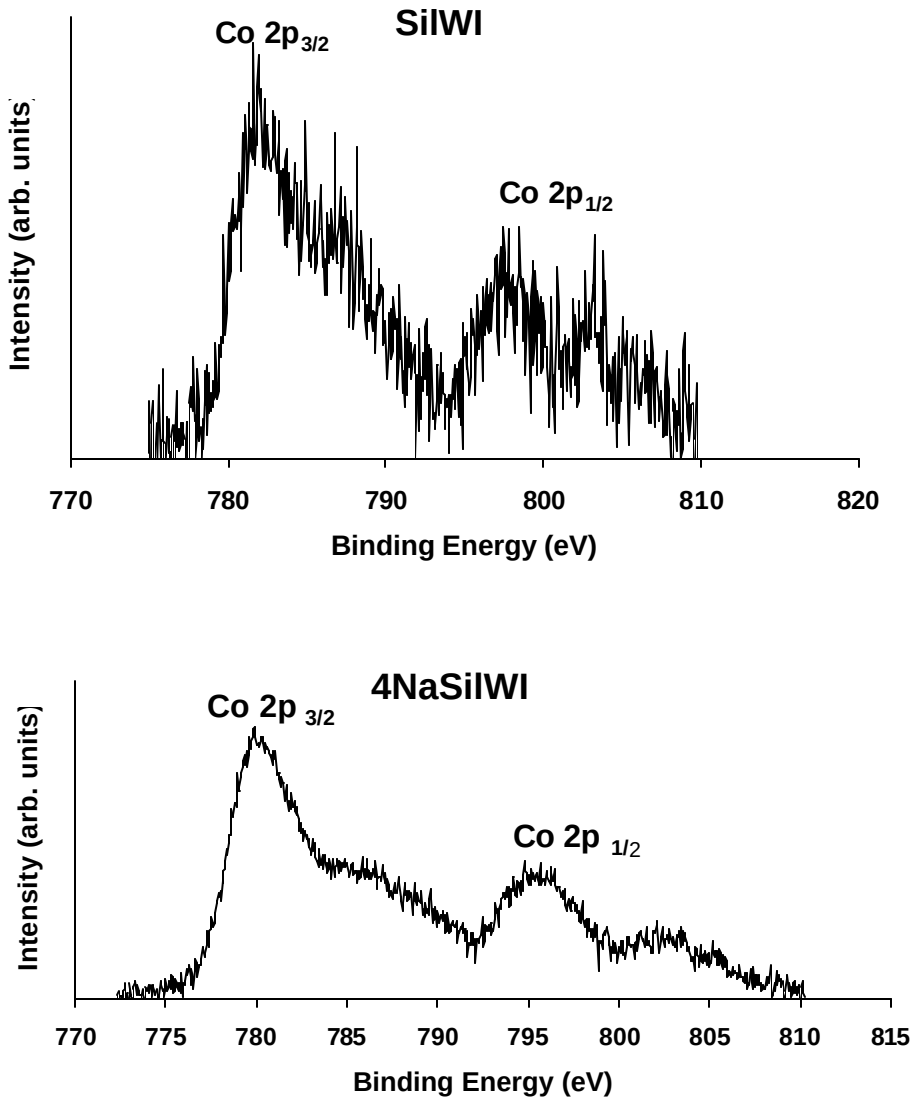

Figure 5.6 Co 2p XPS spectra of selected WI catalyst samples.

Chapter 6

In situ UV-Raman Spectroscopic Studies of Hydrocarbon Catalysis on Platinum-Alumina Catalysts

Section 6.1 Introduction

Many scientists in the field of catalysis have hypothesized on the ability of Raman spectroscopy to probe the mechanism of catalysis by monitoring reaction intermediates.[1-5] Indeed the number of publications reporting Raman spectroscopic studies of heterogeneous catalysts has been growing steadily since 1975.[2] A closer examination of the literature indicates that these studies are similar to those reported in Chapters 4 and 5, in which Raman spectroscopy has been widely used to study solid crystalline phases on the surface of heterogeneous catalysis. *In situ* investigations generally involve monitoring the evolution of these crystalline phases with changes in temperature and gas phase concentration.[6-46] There have been many fewer reports of unenhanced Raman spectra of surface adsorbates that originated from the gas phase.[1,5,47-63] These type of studies are limited due to the small signal-to-noise ratio resulting from the low concentration of adsorbates in the focal volume of the laser.

There are two specialized Raman spectroscopic techniques that greatly enhance signal-to-noise making the detection of such adsorbates easier. One is surface enhanced Raman spectroscopy (SERS), but it is limited to a few specific substrates. The other is Resonance Raman spectroscopy that was briefly discussed in Chapter 2. The resonance enhancement is specific to the adsorbed molecule. To be completely general, Resonance Raman requires a laser tunable over a very wide frequency range. In

addition, interpretation of resonance Raman spectra are sometimes complicated by competing photochemical processes.

As one of the most significant challenges to understanding and controlling selectivity in heterogeneous catalysts, a more general method of detecting surface reaction intermediates is needed. This chapter will focus on attempts to use UV-Raman spectroscopy as a completely general tool to probe the adsorbate structure on industrial Pt-alumina catalysts *in situ.* Surface hydrocarbon fragments play a key role in hydrocarbon conversion reactions in nearly every catalytic process in petroleum refining. Surface scientists have created a wide body of literature describing the nature of these adsorbates on model catalysts, primarily noble metal single crystals and foils, but much of the knowledge of the adsorbate structure from these studies is *ex situ.* [64,65]

Section 6.2 Experimental

Section 6.2.1 Pt / g-Al_2O_3 Industrial Catalyst Exxon Research and Development Laboratory (ERDL) donated several samples of an industrial Pt-alumina catalyst for these experiments. The catalyst preparation technique is proprietary.

The active metal surface area for the 5 wt% catalyst was determined by H_2 chemisorption at 40°C to be 4.719 m^2 / g. The metal dispersion is 38.2%. This data was not obtained for the 0.9 wt% Pt catalyst sample.

Prior to the experiment, the catalyst samples were calcined at 500°C in air for 12 h. The catalyst was activated by heating at 300°C in a stream of flowing H_2 in the UV-Raman reactor.

Section 6.2.2 Experimental Setup In these experiments, the UV-Raman reactors were coupled with a gas chromatograph (GC) which was used to monitor inlet and outlet compositions. The inlet and outlet ports of the UV-Raman reactors are plumbed to the GC column through a combination of two multiposition valves. Both the inlet and outlet compositions can be monitored by alternating the position of those valves as shown in Figure 1a-d.

Section 6.3 Results

Section 6.3.1 Ethylene Hydrogenation over 5 wt% Pt /g-Al_2O_3 Figure 6.2 shows the UV-Raman spectrum acquired during an ethylene hydrogenation reaction at 25°C and atmospheric pressure over a sample of the 5 wt% Pt / γ-Al_2O_3 catalyst obtained in the fluidized bed reactor. The gas contained a mixture of ethylene and hydrogen in a 1:1 molar ratio. The ethylene flow rate was 104.8 sccm and the hydrogen flow rate was 6.88 sccm. The turn over rate (TOR) under these conditions was 0.7 molecules C_2H_4 / Pt atom / sec. The narrow peak centered at 2992 cm^{-1} is attributed to gas phase ethylene. The very broad peak centered at 3050 cm^{-1} encompasses the range from about 2750 to 3250 cm^{-1}. This peak is most likely π-bonded ethylene but could be due to a mixture of species including ethylidyne.[47,66]

Section 6.3.2 Cyclohexene Disproportionation over 0.9 wt% Pt / g-Al_2O_3 In the presence of some catalysts, cyclohexene can disproportionate into cyclohexane and benzene. Because of the distinct Raman spectra of these three molecules, this reaction seemed ideal to study. The experiment was performed in both the packed bed and fluidized bed UV-Raman reactors.

The UV-Raman results for a cyclohexene disproportionation reaction experiment in the packed bed reactor at atmospheric pressure are shown in Figure 6.3. The catalyst was allowed to reach steady-state (i.e., constant conversion of cyclohexene and a constant ratio of reaction products) in a stream of He with approximately 1 Torr of cyclohexene at 25°C before acquiring the spectrum labeled as **1**. One broad peak centered at 1616 cm^{-1} is observed. At these conditions 24% of the cyclohexene is converted and three times as much cyclohexane is produced as benzene. After reaching steady-state at 25°C the catalyst bed was slowly heated to 125°C. Mid-way through the temperature ramp, another Raman spectrum was acquired and labeled as spectrum 2. Again, one broad peak centered at 1616 cm^{-1} is observed. The intensity of this peak is much less than spectrum **1**. The cyclohexene conversion increased as expected from the increase in temperature. The product distribution changed to equal proportions of cyclohexane and benzene. The third spectrum was obtained when the catalyst achieved steady-state at 125°C. The cyclohexene conversions is again higher due to the greater temperature. The concentration of benzene is twice that of cyclohexane.

It is well known that Raman features around 1616 cm^{-1} are due to surface carbonaceous species.[47] When this experiment was repeated in the fluidized bed reactor, no Raman features were observed. Thus it is apparent that the band at 1616 cm^{-1} was due to a carbonaceous species formed from the thermal degradation induced by the laser beam. The Raman features are localized and cannot be compared to the kinetic information for the packed catalyst bed.

Section 6.3.3 UV-Raman spectra of crystalline zeolites and mesoporous silica (MCM-41) nanoparticl catalyst samples In the results presented in Sections

6.3.1 and 6.3.2, no Raman features were detected due to the catalyst. No Raman features are expected for Pt, a fcc metal. The phonon spectra of typical catalytic supports are known to be weak.[2] Since the γ-Al_2O_3 is amorphous, the phonon spectrum is farther weakened. As a test of the capability of the UV-Raman spectroscopy system, four samples of crystalline zeolites were examined. The UV-Raman spectra for ZSM-5, MOR, Zeolite A, and Zeolite Y are shown in Figure 6.4a-d. These spectra agree very well with the recent reports.[67-69]

In Figure 6.5, the UV-Raman spectrum of four different samples of a noble metal nanoparticle catalyst supported by mesoporous silica (MCM-41) is shown. The noble metal nanoparticles have a very narrow distribution of sizes and shapes. The complete analysis of these samples is the subject of a future publication by co-workers. The MCM-41 is semi-crystalline. The Raman features cannot be definitely assigned at the time of publication of this dissertation.

Section 6.4 Conclusions

No Raman features were observed due to either the amorphous alumina support or to hydrocarbon fragments on the surface during the cyclohexene reaction experiments. One very broad peak from 2750 to 3250 cm^{-1} was observed during one ethylene hydrogenation experiment. The broadness of the peak indicates a wide distribution of ethylene fragments on the surface and no correlation between this peak and the reaction kinetics could be drawn. UV-Raman spectroscopy results for mesoporous silica (MCM-41) supported nanoparticle catalysts indicate the need for a crystalline support to detect Raman features for the catalyst. A crystalline or semi-

crystalline support with uniform metal nanoparticle sizes may induce better ordering of surface reaction species and may facilitate interpretation of UV-Raman spectroscopic observations of adsorbed molecules.

Section 6.5 References

(1) Campion, A. *J. Vac. Sci. Technol. B* **1985**, *3*, 1404.

(2) Wachs, I. E. *Topics in Catalysis* **1999**, *8*, 57.

(3) Knozinger, H. *Catalysis Today* **1996**, *32*, 71.

(4) Knozinger, H.; Mestl, G. *Topics in Catalysis* **1999**, *8*, 45.

(5) Chua, Y. T.; Stair, P. C. *J. of Catal.* **2000**, *196*, 66.

(6) Barton, D. G.; Shtein, M.; Wilson, R. D.; Soled, S. L.; Iglesia, E. *J. Phys. Chem B* **1999**, *103*, 630.

(7) Chan, S. S.; Bell, A. T. *Journal of Catalysis* **1984**, *89*, 433.

(8) Pittman, R. M.; Bell, A. T. *J. Phys. Chem* **1993**, *97*, 12178.

(9) Su, S. C.; Bell, A. T. *J. Phys. Chem B* **1998**, *102*, 7000.

(10) Abdelouahab, F. B.; Olier, R.; Guilhaume, N.; Lefebvre, F.; Volta, J. C. *Journal of Catalysis* **1992**, *134*, 151.

(11) Burcham, L. J.; Wachs, I. E. *Spectrochimica Acta, Part A* **1998**, *54A*, 1355.

(12) Chan, S. S.; Wachs, I. E.; Murrell, L. L.; Wang, L.; Hall, W. K. *J Phys Chem* **1984**, *88*, 5831.

(13) Das, N.; Echert, H.; Hangchun, H.; Wachs, I. E.; Walzer, J. F.; Feher, F. J. *J Phys Chem* **1993**, *97*, 8240.

(14) Haller, K.; Lunsford, J. H.; Laane, J. *J Phys Chem-US* **1996**, *100*, 551.

(15) Hardcastle, F. D.; Wachs, I. E. *Journal of Raman Spectroscopy* **1990**, *21*, 683.

(16) Hardcastle, F. D.; Wachs, I. E. *J Phys Chem* **1991**, *95*, 10763.

(17) Hardcastle, F. D.; Wachs, I. E. *Solid State Ionics, Diffusion & Reactions* **1991**, *45*, 201.

(18) Hardcastle, F. D.; Wachs, I. E. *Journal of Solid State Chemistry* **1992**, *97*, 319.

(19) Hardcastle, F. D.; Wachs, I. E. *Journal of Raman Spectroscopy* **1995**, *26*, 397.

(20) Hardcastle, F. D.; Wachs, I. E. *Journal of Raman Spectroscopy* **1995**, *26*, 407.

(21) Hardcastle, F. D.; Wachs, I. E.; Echert, H.; Jefferson, D. A. *Journal of Solid State Chemistry* **1991**, *90*, 194.

(22) Horsley, J. A.; Wachs, I. E.; Brown, J. M.; Via, G. H.; Hardcastle, F. D. *J Phys Chem* **1987**, *91*, 4014.

(23) Lunsford, J. H.; Yang, X. M.; Haller, K. *J Phys Chem-US* **1993**, *97*, 13810.

(24) Mestl, G.; Knozinger, H.; Lunsford, J. H. *Ber Bunsen Phys Chem* **1993**, *97*, 319.

(25) Mestl, G.; Rosynek, M. P.; Lunsford, J. H. *J Phys Chem B* **1997**, *101*, 9321.

(26) Mestl, G.; Rosynek, M. P.; Lunsford, J. H. *J Phys Chem B* **1997**, *101*, 9329.

(27) Mestl, G.; Rosynek, M. P.; Lunsford, J. H. *J Phys Chem B* **1998**, *102*, 154.

(28) Mestl, G.; Xie, S. B.; Rosynek, M. P.; Lunsford, J. H. *Stud Surf Sci Catal* **1998**, *118*, 459.

(29) Snyder, T.; Hill, C. G., Jr. *Journal of Catalysis* **1991**, *132*, 536.

(30) Wachs, I. E.; Chan, S. S. *Applications of Surface Science* **1984**, *20*, 181.

(31) Weckhuysen, B. M.; Mestl, G.; Rosynek, M. P.; Lunsford, J. H. *J Phys Chem B* **1998**, *102*, 3773.

(32) Weckhuysen, B. M.; Rosynek, M. P.; Lunsford, J. H. *Phys Chem Chem Phys* **1999**, *1*, 3157.

(33) Williams, C. C.; Ekerdt, J. G.; Jehng, J.-M.; Hardcastle, F. D.; Turek, A. M.; Wachs, I. E. *J Phys Chem* **1991**, *95*, 8781.

(34) Williams, C. C.; Ekerdt, J. G.; Jehng, J.-M.; Hardcastle, F. D.; Wachs, I. E. *J Phys Chem* **1991**, *95*, 8791.

(35) Xie, S. B.; Lunsford, J. H. *Appl Catal A-Gen* **1999**, *188*, 137.

(36) Xie, S. B.; Mestl, G.; Rosynek, M. P.; Lunsford, J. H. *J Am Chem Soc* **1997**, *119*, 10186.

(37) Xie, S. B.; Rosynek, M. P.; Lunsford, J. H. *Journal of Catalysis* **1999**, *188*, 24.

(38) Xie, S. B.; Rosynek, M. P.; Lunsford, J. H. *Appl Spectroscopy* **1999**, *53*, 1183.

(39) Xie, S. B.; Rosynek, M. P.; Lunsford, J. H. *Journal of Catalysis* **1999**, *188*, 32.

(40) Yu, Z.; Yang, X.; Lunsford, J. H.; Rosynek, M. P. *Journal of Catalysis* **1995**, *154*, 163.

(41) Li, C.; Li, M. *J. Raman Spectrosc.* **2002**, *33*, 301.

(42) Kuba, S.; Knozinger, H. *J. Raman Spectrosc.* **2002**, *33*, 325.

(43) Mestl, G. *J. Raman Spectrosc.* **2002**, *33*, 333.

(44) Busca, G. *J. Raman Spectrosc.* **2002**, *33*, 348.

(45) Banares, M. A.; Wachs, I. E. *J. Raman Spectrosc.* **2002**, *33*, 359.

(46) Arab, M.; Bougeard, D.; Aubry, J. M.; Marko, J.; Paul, J. F.; Payen, E. *J. Raman Spectrosc.* **2002**, *33*, 390.

(47) Li, C.; Stair, P. C. *Catalysis Today* **1997**, *33*, 353.

(48) Campion, A. *Annual Review of Physical Chemistry* **1985**, *36*, 549.

(49) Campion, A. *Journal of Electron Spectroscopy and Related Phenomena* **1990**, *54*, 877.

(50) Campion, A.; Brown, J. K.; Grizzle, V. *Surface Science* **1982**, *115*, L153.

(51) Campion, A.; Mullins, D. R. *Chem. Phys. Letters* **1983**, *94*, 576.

(52) Campion, A.; Mullins, D. R. *Surface Science* **1985**, *158*, 263.

(53) Hallmark, V. M.; Campion, A. *Chem. Phys. Letters* **1984**, *110*, 561.

(54) Hallmark, V. M.; Campion, A. *J. Chem. Phys.* **1986**, *84*, 2942.

(55) Hallmark, V. M.; Campion, A. *J. Chem. Phys.* **1986**, *84*, 2933.

(56) Harradine, D.; Campion, A. *Chemical Physics Letters* **1987**, *135*, 501.

(57) Kambhampati, P.; Child, C. M.; Foster, M. C.; Campion, A. *J. Chem. Phys.* **1997**, *108*, 5013.

(58) Mullins, D. R.; Campion, A. *Chemical Physics Letters* **1984**, *110*, 565.

(59) Perry, S. S.; Campion, A. *Surface Science Letters* **1990**, *234*, L275.

(60) Perry, S. S.; Campion, A. *Surface Science* **1991**, *259*, 207.

(61) Shannon, C.; Campion, A. *Journal of Physical Chemistry* **1988**, *92*, 1385.

(62) Shannon, C.; Campion, A. *Surface Science* **1990**, *227*, 219.

(63) Moissette, A.; Gener, I.; Bremard, C. *J. Raman Spectrosc.* **2002**, *33*, 381.

(64) Somorjai, G. A. *Chemistry in Two Dimensions*; Cornell University Press: Ithaca, NY, 1981.

(65) Somorjai, G. A. *Introduction to Surface Chemistry and Catalysis*; Wiley-Interscience: New York, 1994.

(66) Cremer, P. S.; Su, X.; Shen, Y. R.; Somorjai, G. A. *J. Am. Chem. Soc.* **1996**, *118*, 2942.

(67) Yu, Y.; Xiong, G.; Li, C.; Xiao, F. S. *Microporous and Mesoporous Materials* **2001**, *46*, 23.

(68) Poborchii, V. V. *J. Chem. Phys.* **2001**, *114*, 2707.

(69) Mozgawa, W. *Journal of Molecular Structure* **2001**, *596*, 129.

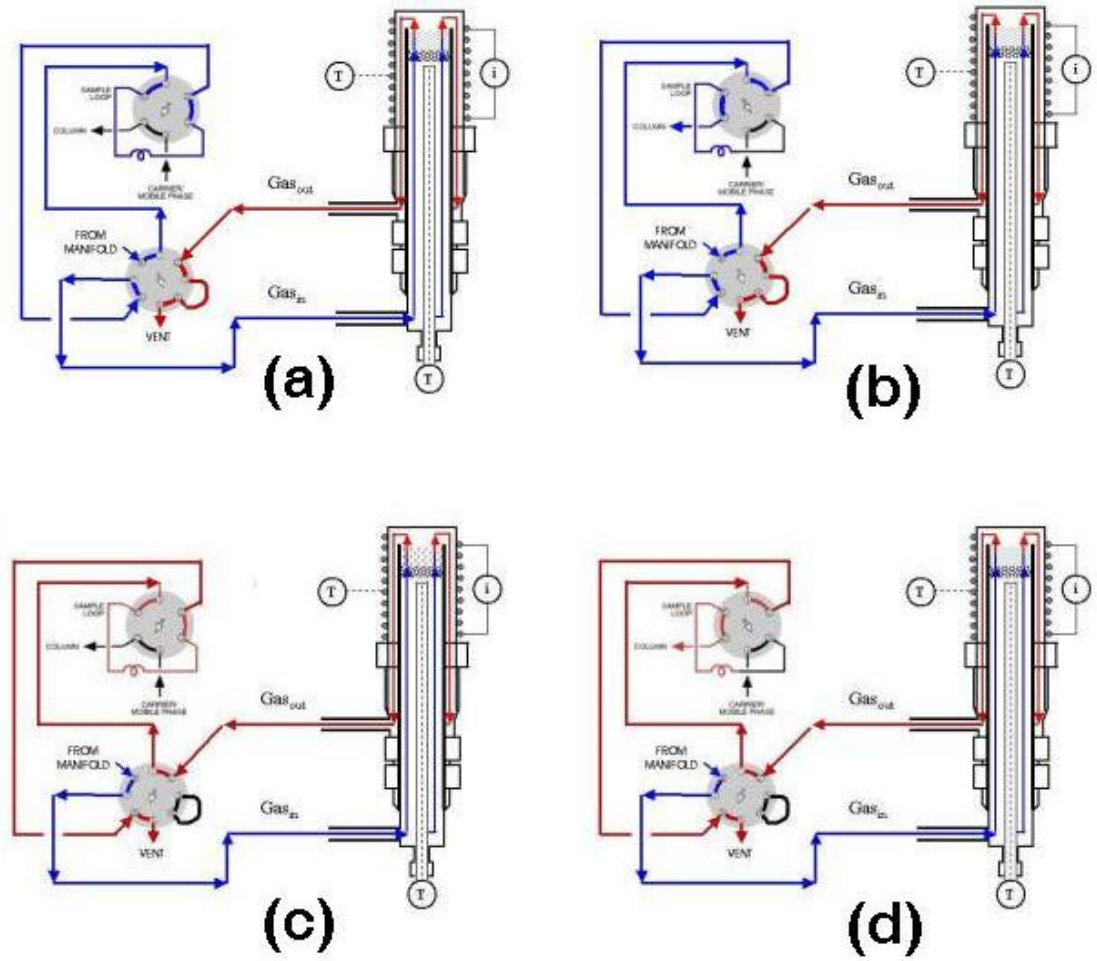

Figure 6.1 UV-Raman reactor and gas chromatography configuration for (a) & (b) inlet gas sampling and (c) & (d) outlet gas sampling.

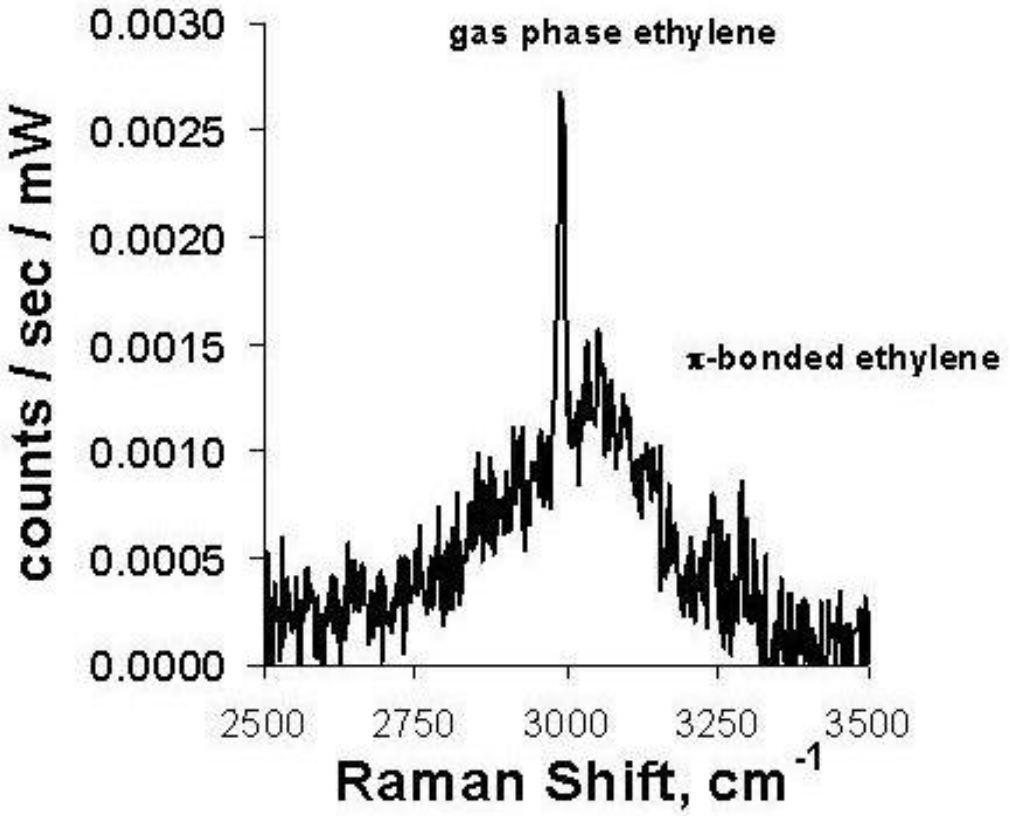

Figure 6.2 UV-Raman spectrum during ethylene hydrogenation over 5 wt% Pt / γ-Al_2O_3. Experiment conducted in fluidized bed UV-Raman reactor.

Reaction conditions:
1:1 Molar ration C_2H_4 : H_2
Temperature = 25^{o}C
Fluidized bed UV-Raman reactor

Flow rates:
104.8 sccm C_2H_4
6.88 sccm H_2

Laser and spectrometer settings:
Laser Power = 64 mW
Acquisition time = 40 min
S3 = 100
S1 = S2 = fully open
Filter = 1050 nm
λ_c = 261.0 nm

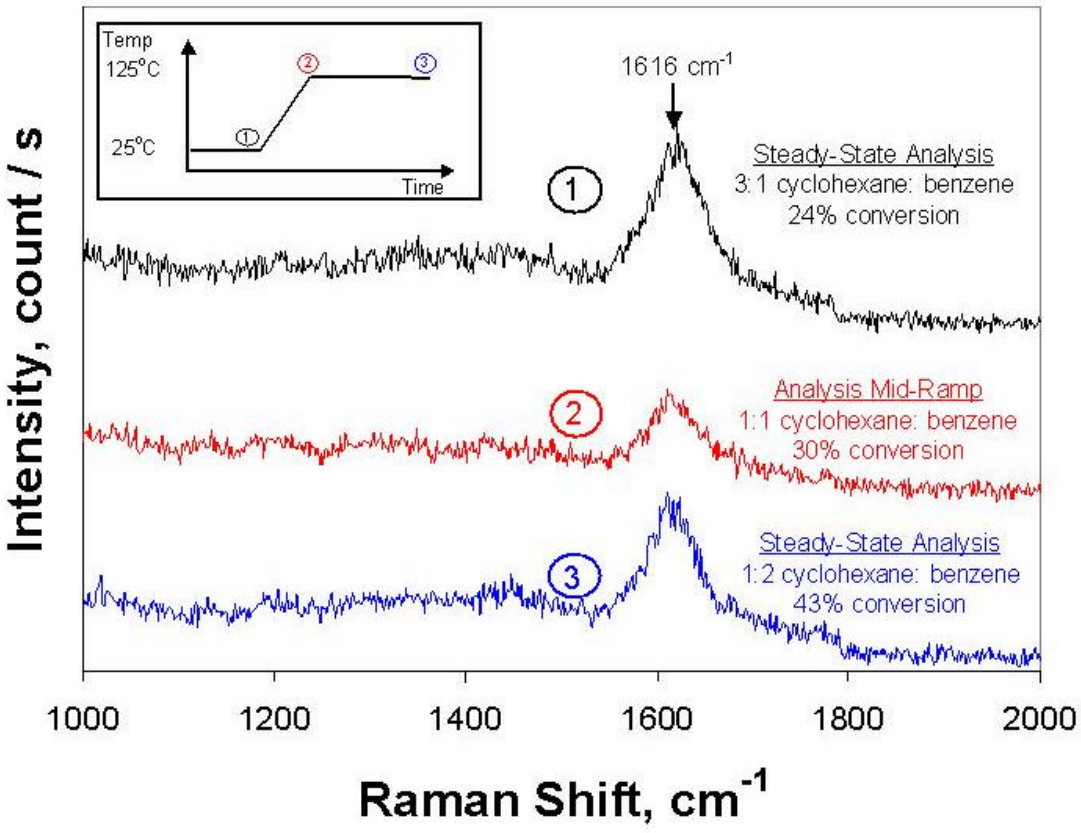

Figure 6.3 UV-Raman spectra during cyclohexene disproportionation over 0.9 wt% Pt γ-Al_2O_3. Experiment conducted in packed bed UV-Raman reactor.

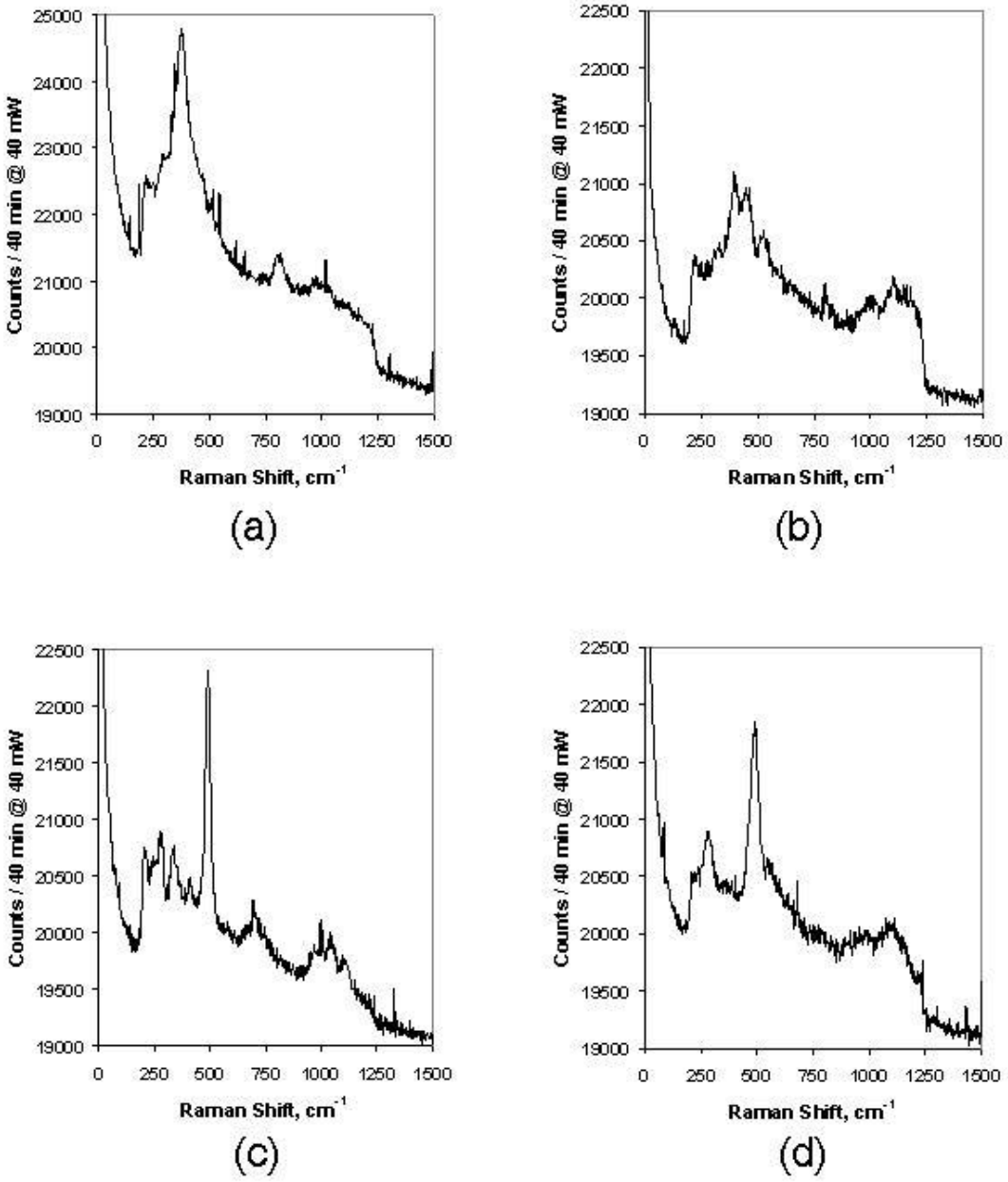

Figure 6.4 UV-Raman spectra of (a) ZSM-5, (b) MOR, (c) Zeolite A, and (d) Zeolite Y. Spectrometer settings are as follows: S1 = 300, S2 = 4.5, S1 = 0.45, Filter = 993.4 nm, and λ_c = 251.3. Laser power = 40 mW accumulated for 40 minutes.

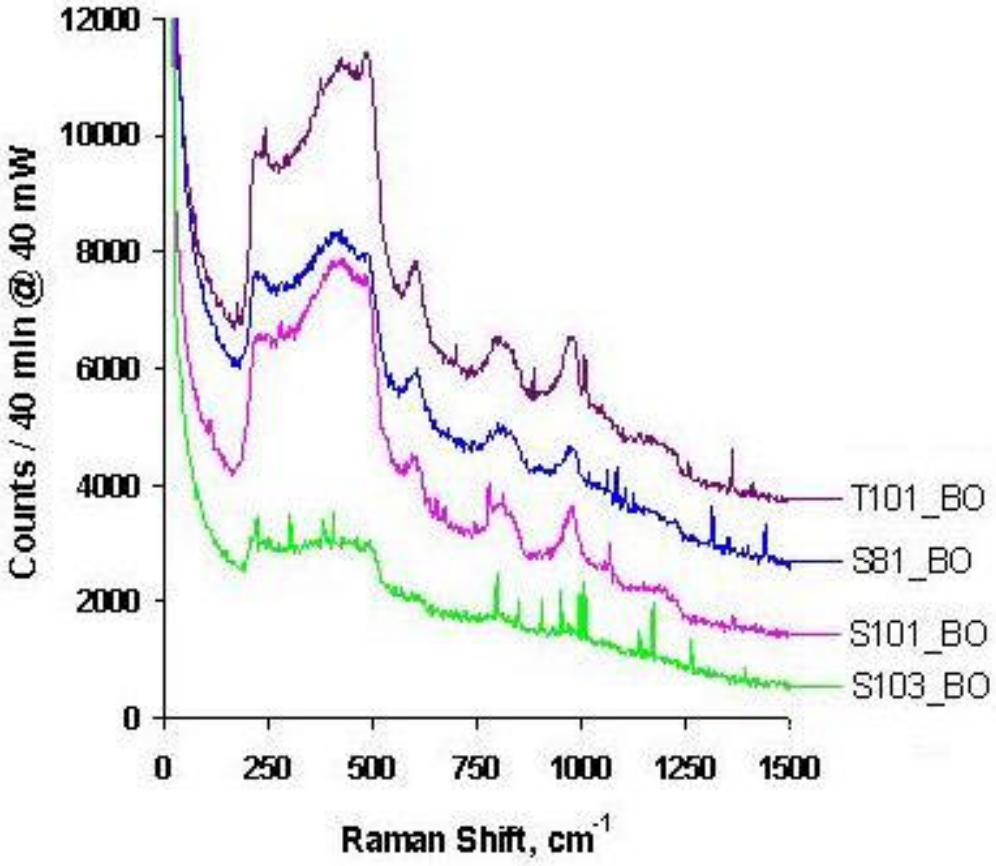

Figure 6.5 UV-Raman spectra of mesoporous silica (MCM-41) supported noble metal nanoparticle catalyst samples.

Chapter 7

Summary

UV-Raman spectroscopy has been successfully applied to studying heterogeneous catalysts *in situ* and *ex situ*. This technique will continue to be a useful complement to the array of *ex situ* surface science techniques such as X-ray photoelectron spectroscopy (XPS) and temperature programmed desorption (TPD). The availability of continuous wave lasers with an output in the ultraviolet have eliminated the fluorescence interference commonly encountered with many catalytic support materials.

The preponderance of the Raman spectroscopic studies in this dissertation and the current literature involve the changes in the crystalline phases on the catalyst surface due to changes in preparation methods or reaction environment. The highest concentration of scattering molecules in the focal volume of the laser are usually these crystalline phases which makes it quite easy to obtain a high signal-to-noise ratio. Fluidized and spinning bed reactors can be used, even in a less than optimized collection geometry, to minimize thermally induced laser damage while acquiring a Raman spectrum of these crystalline phases.

The goal of monitoring the structure of surface adsorbates during a catalytic reaction has not been fully realized. This is largely due to the low number of adsorbates in the focal volume of the laser. If adsorbates are susceptible to laser induced damage, it is even more difficult to measure the Raman spectrum. There are generally two

methods to enhance the signal-to-noise ratio of adsorbate Raman spectra: Surface Enhanced Raman Spectroscopy (SERS) and Resonance Raman spectroscopy. SERS is substrate specific and Resonance Raman spectroscopy is adsorbate specific. In addition, photochemical damage is difficult to avoid in Resonance Raman spectroscopy. To use Raman spectroscopy as a generally applicable technique to study adsorbates on catalysts, more progress needs to be made on reactors that can minimize thermal damage while optimizing the scattered light collection. Ideally, a Raman excitation source in the IR, visible, and UV spectral regions should be available. The choice of excitation source could be optimized based upon the optical properties of the system of interest.